CO_2 SEQUESTRATION ASSESSMENT USING MULTICOMPONENT 3D SEISMIC DATA: ROCK SPRINGS UPLIFT, WYOMING

A Thesis Presented to

the Faculty of the Department of Earth and Atmospheric Sciences

University of Houston

In Partial Fulfillment

of the Requirements for the Degree

Master of Science

By

Luis Alejandro Lopez Guedez

May 2019

CO_2 SEQUESTRATION ASSESSMENT USING MULTICOMPONENT 3D SEISMIC DATA: ROCK SPRINGS UPLIFT, WYOMING

Luis Alejandro Lopez

APPROVED:

Dr. Robert R. Stewart, Chairman

Dept. of Earth and Atmospheric Sciences

Dr. Hua-Wei Zhou

Dept. of Earth and Atmospheric Sciences

Dr. Richard Verm

SAExploration Holdings, Inc.

Dean, College of Natural Sciences and Mathematics

CO_2 SEQUESTRATION ASSESSMENT USING MULTICOMPONENT 3D SEISMIC DATA: ROCK SPRINGS UPLIFT, WYOMING

An Abstract Presented to

the Faculty of the Department of Earth and Atmospheric Sciences

University of Houston

In Partial Fulfillment

of the Requirements for the Degree

Master of Science

By

Luis Alejandro Lopez Guedez

May 2019

Abstract

Geophysical analysis plays a crucial role in the assessing, measuring, and monitoring of CO_2 sequestration. Seismic data allows the extraction of lithologic and fluid properties via inversion techniques that aid in identifying CO_2 storage compartments and monitoring of fluid injection into the subsurface. Although the industry standard is to analyze the vertical component (PP reflection) data, converted-wave reflections (P-to-S conversion) can be used to help determine density information with higher reliability due to the sensitive variations of the S-waves to density. Multi-component seismic data is processed for PP and PS reflections, and pre-stack simultaneous inversion is applied to the data to generate elastic properties of the subsurface to complete a reservoir assessment for CO_2 sequestration in the Rock Springs Uplift, Wyoming. Rock physics and sensitivity analysis at the well location shows that a 5% porosity increase at the target intervals corresponds to a 16% - 19% decrease in σ and $\mu\rho$, making these attributes optimal for CO_2 sequestration assessment in the area. A porosity volume is generated by a least-squares linear regression with $\mu\rho$ at the well location that displays a 93% correlation. The resultant porosity relation is applied to the $\mu\rho$ inverted volume, and the average porosity values obtained at the Weber and Nugget sandstones throughout the survey are 9% – 14% and 12% – 18%, respectively. Extracted porosity maps from the target formations display high-porosity anomalies in the eastern section of the survey and are interpreted for the P30, P60, and P90 case. The anomalous areas are utilized jointly with isopach and porosity

maps to determine the range of CO_2 mass for storage capacity and ranges from 120 Mt to 561 Mt. Considering the efficiency storage factors between 0.2 – 1, the daily CO_2 emissions from the Jim Bridger power plant of 16 Mt, pressure and temperature conditions of CO_2 of 701 bars and 366 ^{o}K at the target depth, the duration for sequestration range from 7 years to 34 years for the large high-porosity anomalous area. A CO_2 injection model is created, and a well for sequestration is proposed at a latitude of 41^{o}42'34.799" and a longitude of -108^{o}47'54.019".

Contents

List of Figures

List of Tables

List of Abbreviations

ACP	=	Asymmetrical Conversion Point
AI	=	Acoustic Impedance
AVA	=	Amplitude Versus Azimuth
AVO	=	Amplitude Versus Offset
CCP	=	Common Conversion Point
CCS	=	Carbon Capture and Sequestration
CDP	=	Common Depth Point
CMP	=	Common Mid-Point
CO_2	=	Carbon Dioxide
DHI	=	Direct Hydrocarbon Indicator
f-k	=	Frequency – Wavenumber
ft	=	Feet
ft/s	=	Feet per Second
G	=	Gradient
GR	=	Gamma-Ray

HTI	=	Horizontal Transverse Isotropy
Hz	=	Hertz
IFP	=	Institut Francais du Petrole
NMO	=	Normal Move Out
NI	=	Normal Incidence
m	=	Meters
mD	=	Millidarcy
ms	=	Milliseconds
Mt	=	Metric Megaton
m/s	=	Meters per Seconds
OVT	=	Offset Vector Tile
p	=	Move-Out
PR	=	Poisson's Reflectivity
PP	=	Primary to Primary reflections
PS	=	Primary to Secondary reflections
PSTM	=	Pre-Stack Time Migration
RMS	=	Root Mean Square

RNMO	=	Residual Normal Move Out
RSU	=	Rock Springs Uplift
s	=	Seconds
SI	=	Shear Impedance
SOF	=	Structure-Oriented Filter
SWS	=	Shear-wave Splitting
V_p	=	P velocity
V_s	=	S velocity
VTI	=	Vertical Transverse Isotropy
WAZ	=	Wide-Azimuth
ρ	=	Density
ϕ	=	Porosity
σ	=	Poisson's ratio
$\lambda\rho$	=	Lambda-Rho
$\mu\rho$	=	Mu-Rho
$\frac{V_p}{V_s}$	=	P velocity over S velocity ratio
τ-ρ	=	Two-way zero offset time – Ray parameter

Chapter 1

Introduction

Primary objectives of seismic exploration are to characterize the response of seismic amplitudes and generate rock physics relationships that can be used to predict variations in reservoir properties. The data may undergo a rigorous processing and post-migration conditioning workflow that aids in the subsurface structural imaging and increases signal-to-noise values to correctly characterize the subsurface via seismic amplitudes. The results of seismic imaging can be utilized for the evaluation of seismic amplitudes for reservoir characterization using various analytic interpretation techniques such as forward modeling, sensitivity analysis, rock physics relationship generation, AVO inversion, and elastic attribute interpretation. Even though often ignored, the addition of converted-wave (PS) seismic data into the reservoir characterization can significantly improve the determination of bulk density, which in turns aids in the completeness of the reservoir studies. Joint PP-PS inversion methodologies increase the reliability of elastic properties generated and can be used for enhanced characterization of the subsurface.

1.1 The problem

Even though the subsurface of Rock Springs Uplift (RSU), Wyoming has been subject to geologic analysis utilizing seismic data (Pafeng et al., 2017; Grana et al., 2017), a more robust reservoir characterization can be employed to obtain reliable information of porosity, density, and elastic rock properties by incorporating PS converted seismic wave data to the analysis. Although it is widely known the incorporation of converted-wave data to reservoir analysis can aid in the reliable determination of elastic properties, this type of dataset is often neglected in the oil and gas industry (Pafeng et al., 2017). PP reflection data is dependent on the rock matrix and the saturating fluid within the rock matrix. Although this may be beneficial for characterizing hydrocarbons in oil and gas exploration, additional information is required to obtain information solely on the rock medium in which the wave propagates. Fluids lack the ability to resist shear stresses, and the primary driving mechanism of shear-wave propagation is through shear resistance (Omnes, 1978). Hence, the S-wave largely neglects the saturating fluid and is primarily affected by the rock matrix. Thus, elastic rock properties can be extracted for reservoir analysis with increased accuracy in comparison to attributes generated solely based on PP data.

1.2 Objectives

This study aims to investigate the rock properties of the Pennsylvanian Weber and Jurassic – Triassic Nugget sandstones in the Rock Springs Uplift, Wyoming and create rock physics relationships with the elastic response. Seismic processing, forward modeling, and sensitivity analysis are carried out with the primary purpose of finding a signature of the porosity and elastic behavior of the reservoir of interest. Furthermore, PS converted-wave seismic data are incorporated in the study to aid the characterization of the elastic response from the derivation of rock properties. This is undertaken via PP and PS seismic inversion followed by a robust multi-attribute interpretation process conducted to estimate accurate porosity values utilized for CO_2 storage. The results from the inversion are used to develop additional elastic attributes that are used to identify lithologic and geomechanical information of the Weber and Nugget sandstones.

The main questions to address in this study are:

- What rock physics relationships can be derived from well-logs to determine accurate elastic property characteristics using seismic data?
- Where are the locations with higher porosity content for the Nugget and Weber sandstones for CO_2 storage within the seismic survey?
- What are the multicomponent processing and gather-conditioning workflows and parameters for the seismic data in this area? (i.e. statics, velocity models).

1.3 Carbon dioxide sequestration

Carbon capture storage or sequestration (CSS) refers to the capturing of CO_2 by utilizing industrial plants to remove the CO_2 from exhaust gases and potentially use deep strata within the subsurface for long-term storage away from the atmosphere (Benson and Cole, 2008). This process requires the compression and injection of the CO_2 in sealed and porous sedimentary compartments within geologic formations, where it can potentially remain stored for long periods of time. The principal strata of interest for CCS are thick sequences of sedimentary rocks within which there are permeable rocks such as sandstones, which work as storage reservoirs. Overlying low permeability rocks, typically shales, serve as seals to block upward migration of the CO_2 (Benson and Cole, 2008). Figure 1.1 displays the typical process for CCS and the expected depths of sequestration.

The main goal of storing CO_2 in deep sedimentary formations is to diminish emissions of greenhouse gases into the atmosphere. A billion metric tons or more must be sequestered annually to noticeably reduce CO_2 in the atmosphere (Benson and Cole, 2008). This corresponds to 250 times increase over the amount of what is sequestered today. CCS contributes up to 20% of carbon dioxide emissions reduction (Benson and Cole, 2008).

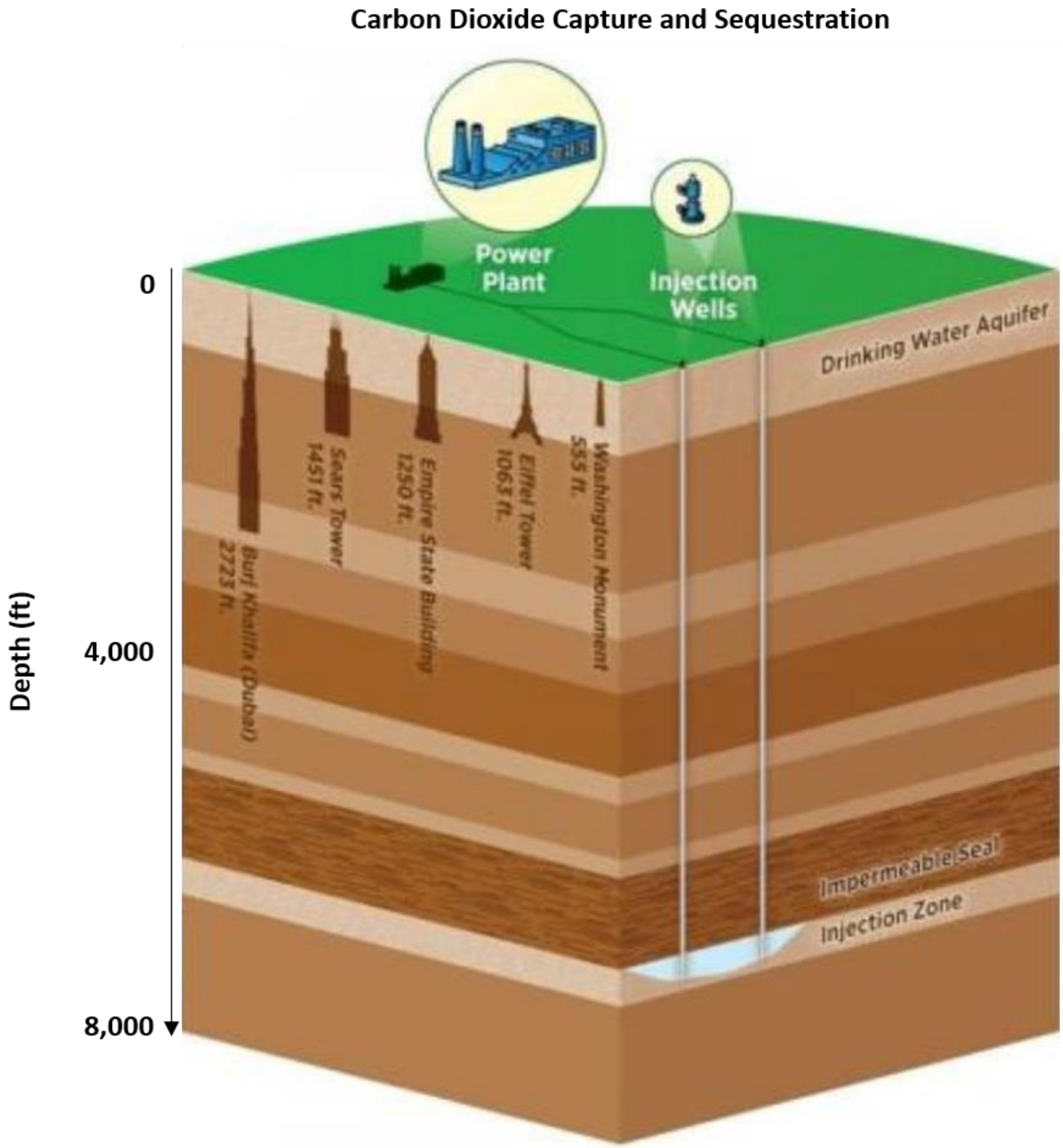

Figure 1.1: Schematic diagram demonstrating the typical process and depths for CCS. (modified from EPA, 2017).

Carbon capture or sequestration is one of the principal greenhouse gas reduction processes, and it provides the potential for CO_2 emissions from power plants (EPA, 2017).

According to the U.S Inventory of Greenhouse Gas Emissions and Sinks, more than 40% of carbon dioxide emissions in the United States are from electric power generation. Carbon capture technologies are currently available and could drastically reduce emissions by 80-90% from power plants that burn fossil fuels. Figure 1.2 displays a rough estimate of the amount of carbon dioxide that should be sequestered by the year 2050 according to the International Energy Agency (IEA). The graph displays the amount of CO_2 emitted for different processes, with coal power being the highest emitter of carbon dioxide (IEA, 2013)

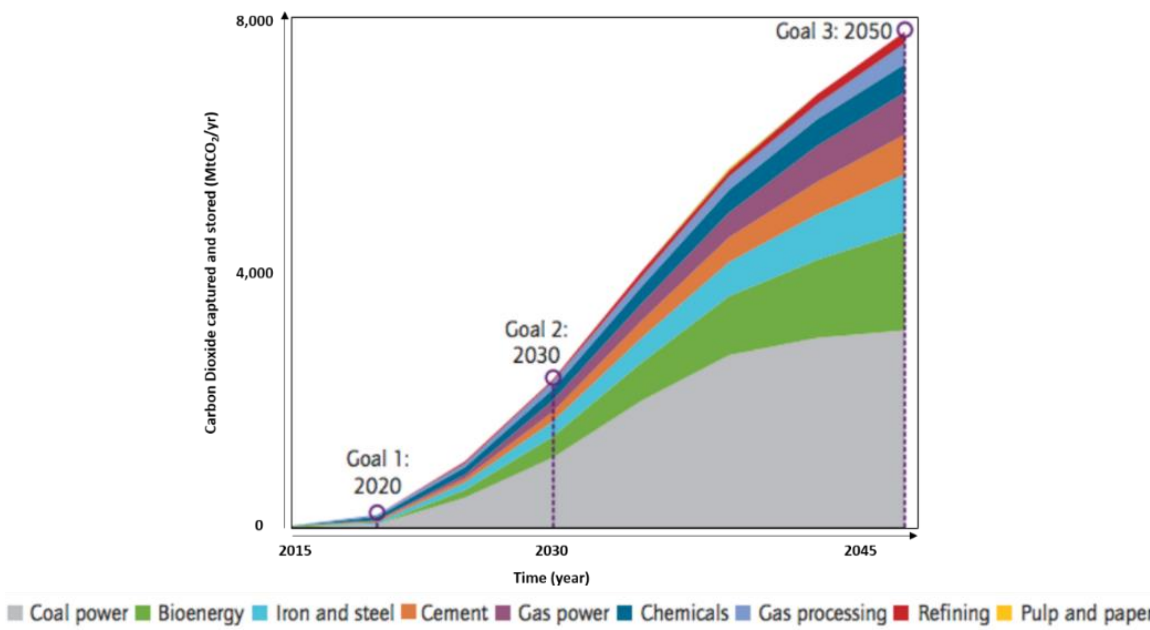

Figure 1.2: Estimate of the goals of carbon dioxide that should be sequestered by the year 2050. A projection of the amount of CO_2 from various CO_2-emitting processes with time is displayed (modified from IEA, 2013).

Figure 1.3 shows a map of carbon capture or storage (CCS) projects in North America using CO_2 emissions from power plants. There are approximately 25 operational sequestration projects globally with 13 of those being in North America (Burns, 2017).

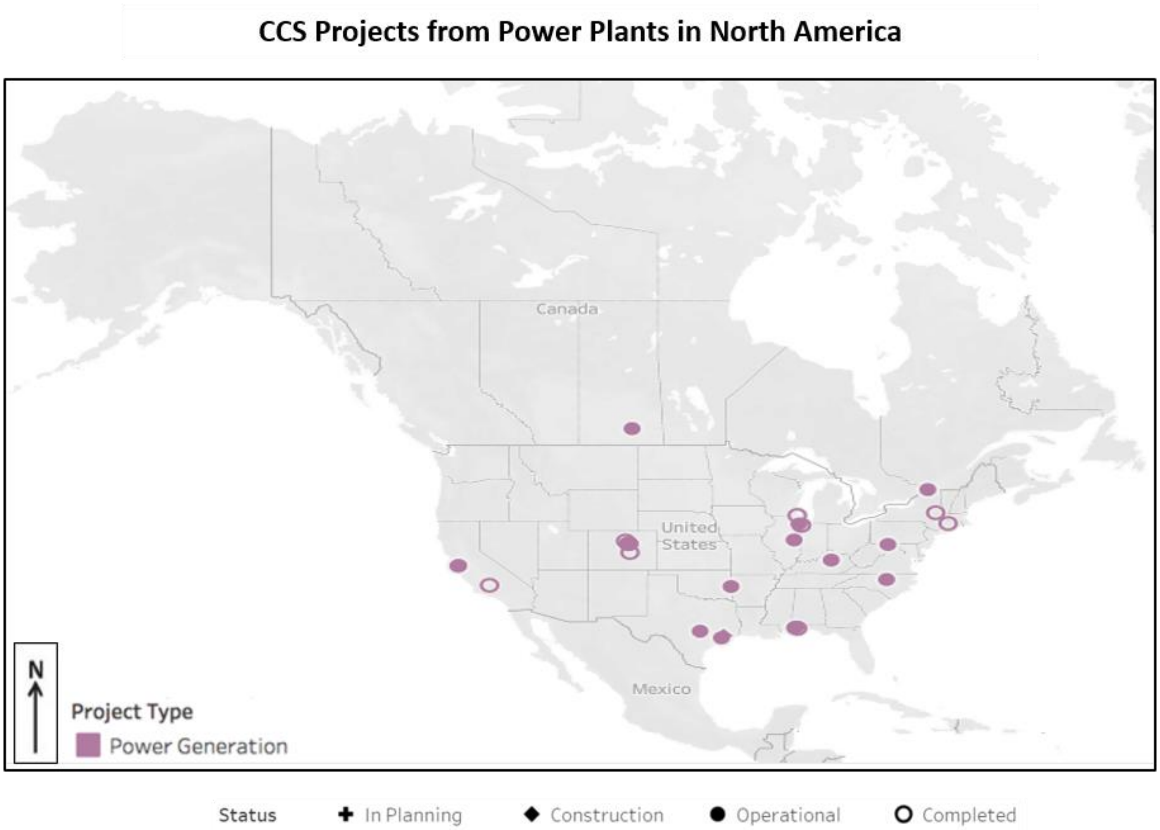

Figure 1.3: Map of CCS projects in North America for CO_2 emitted from power plants. Approximately 25 projects worldwide are currently operational. 13 projects are currently operational in North America (modified from Burns, 2017).

1.4 PP and PS reflections

The Zoeppritz equations relate the reflections of an incident, reflected, and transmitted P and S-waves on both sides of a medium's interface. To be able to analyze wave reflections, an equation which relates the reflected wave amplitudes to incident wave amplitudes as a function of the angle of incidence is required. There are various forms of simplified Zoeppritz wave equations of PP reflection coefficients that appear in literature and are commonly used in industry (Aki and Richards, 1980; Shuey, 1985; Parson, 1986; Smith and Gidlow, 1987; Verm and Hilterman, 1994; Stewart et al., 2002). Each different simplification links the reflection amplitude with variations to rock properties to some degree. Figure 1.4 displays a schematic diagram of an incident P-wave and its corresponding reflected and transmitted P and S-waves.

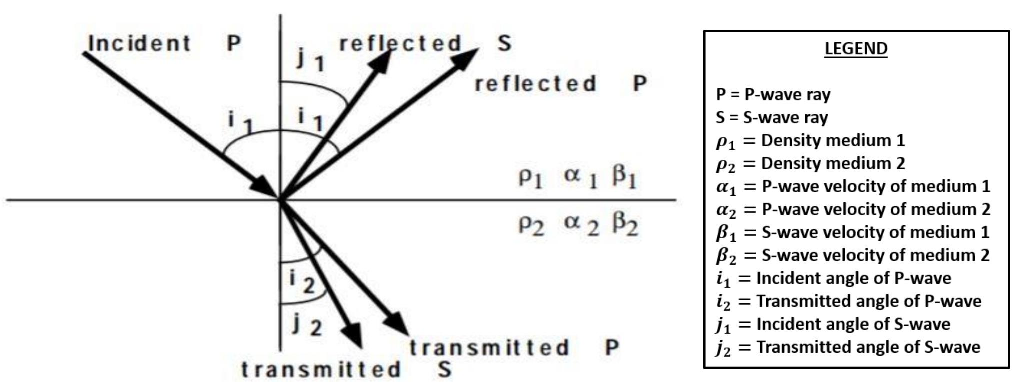

Figure 1.4: Schematic diagram displaying an incident P-wave and its corresponding reflected and refracted P and S-waves (modified from Feng and Bancroft, 2006).

Amplitude versus offset or azimuth (AVO or AVA) equations describe the amplitude coefficients of an incident P-wave as the angle of the incident or source-receiver offsets increases. As the AVO phenomena translate the sharing of the energy of the incident compressible wave between the compressible and converted reflections, the observation of the converted mode AVO would be redundant (Xu and Bancroft, 1997. Single fold data are not pure enough to provide reliable amplitude measurements and results may be doubtful (Xu and Bancroft, 1997). In such a case, the study of AVO of the converted-waves can be advantageous (Xu and Bancroft, 1997). Equation 1 displays the Aki-Richards (1980) approximation of PS reflection coefficients.

$$PS = \frac{-p\alpha}{2cosj}[\left(1 - 2\beta^2p^2 + 2\beta^2\frac{cosi}{\alpha}\frac{cosj}{\beta}\right)\frac{\Delta p}{p} - (4\beta^2p^2 - 4\beta^2\frac{cosi}{\alpha}\frac{cosj}{\beta})\frac{\Delta\beta}{\beta}] \qquad (1)$$

Where PS refers to the reflection coefficient for converted-waves, p is the average density, α is the average P-wave velocity, β is the average S-wave velocity, and Δ refers to the change of the parameter. The angle i is the average of the incident and transmitted P-wave angles while j is the average of the reflected and transmitted S-wave angles (Xu and Bancroft, 1997). Although AVO analysis and methodologies are industry standard, AVO assumes the recorded seismic data consists of primary reflections only and are not contaminated by other wave propagation effects, such as multiples and converted-waves (Pafeng et al., 2017). In a modeling study, Mallick and Adhikari (2015) demonstrate that such assumptions are valid only for a relatively small source-to-receiver offset. Typically for the offsets corresponding to the incident angles of 30 degrees or less. For the large offsets or angles (greater than 30 degrees), the recorded seismic data are increasingly affected by the complex effects of wave propagation; therefore, the application of AVO to large offset/angle reflections become more difficult (Mallick and Adhikari, 2015).

A primary objective of pre-stack seismic inversion is to derive reliable estimates of P-wave velocity, S-wave velocity, and density from which elastic attributes can be calculated to predict fluid and lithologic properties of the subsurface. Due to limitations of seismic methods such as band-limited characteristics and noise levels, information from various approaches, such as converted-waves, are continuously obtained for a comprehensive interpretation of the subsurface. P and S-wave velocities can be derived from inversion and converted to λ and μ elastic attributes to detect reservoirs. They can be used as direct hydrocarbon indicators (DHI) (Goodway et al., 1997). One of the main issues of the seismic inversion is the non-uniqueness component due to the limited information available. There are many sources of uncertainty such as errors in background velocity that causes the $\frac{V_p}{V_s}$ to change significantly and eliminates the high-frequency contrast. Careful selection of parameters, background velocity, wavelet estimation, and application of a priori information is still important issues which remain to be resolved (Xu and Bancroft, 1997). By incorporating additional information to the seismic inversion, such as PS reflection data, the inversion becomes more stable and more reliable results from elastic attributes can be obtained.

1.5 Geological background

The Rock Springs Uplift (RSU) was formed during the late Cretaceous to Paleogene Laramide Orogeny, and it is cut by several east and north-east trending faults (Erslev and Koenig, 2009) located in Sweetwater County, Wyoming (Figure 1.5). The uplift extends for approximately 50 miles (80 km) in the north-south direction and 35 miles (56 km) in the east-west direction and is characterized by a plunging anticline structure (Mallick and Adhikari, 2015). The Baxter shale is the secondary seal above the primary target formations for this study, which are the Weber and Nugget sandstones. The Mesa Verde group is 3,500 ft (1,066 m) thick and overlays the Baxter Shale. This geologic group consists of, in ascending order, the Blair formation, Rock Springs formation, Ericson sandstone, and Almond formation (Mallick and Adhikari, 2015). A thick Paleozoic deep saline aquifer sequence; Madison limestone and Weber sandstone are overlain by sealing shale formations (Mowry and Baxter shales and the Lower Triassic units). These aquifers, in conjunction with the quality of the overlying seals, make them potential targets for CO_2 sequestration (McLaughlin and Garcia-Gonzales, 2013).

The geologic setting at RSU contains favorable characteristics for potential CO_2 sequestration. This includes laterally extensive sandstone reservoirs, primary seals directly overlying the potential reservoirs, and a thick secondary seal (Allis, 2003). Figure 1.6 displays a schematic cross-section of the geologic structure and formations near the well RSU-#1.

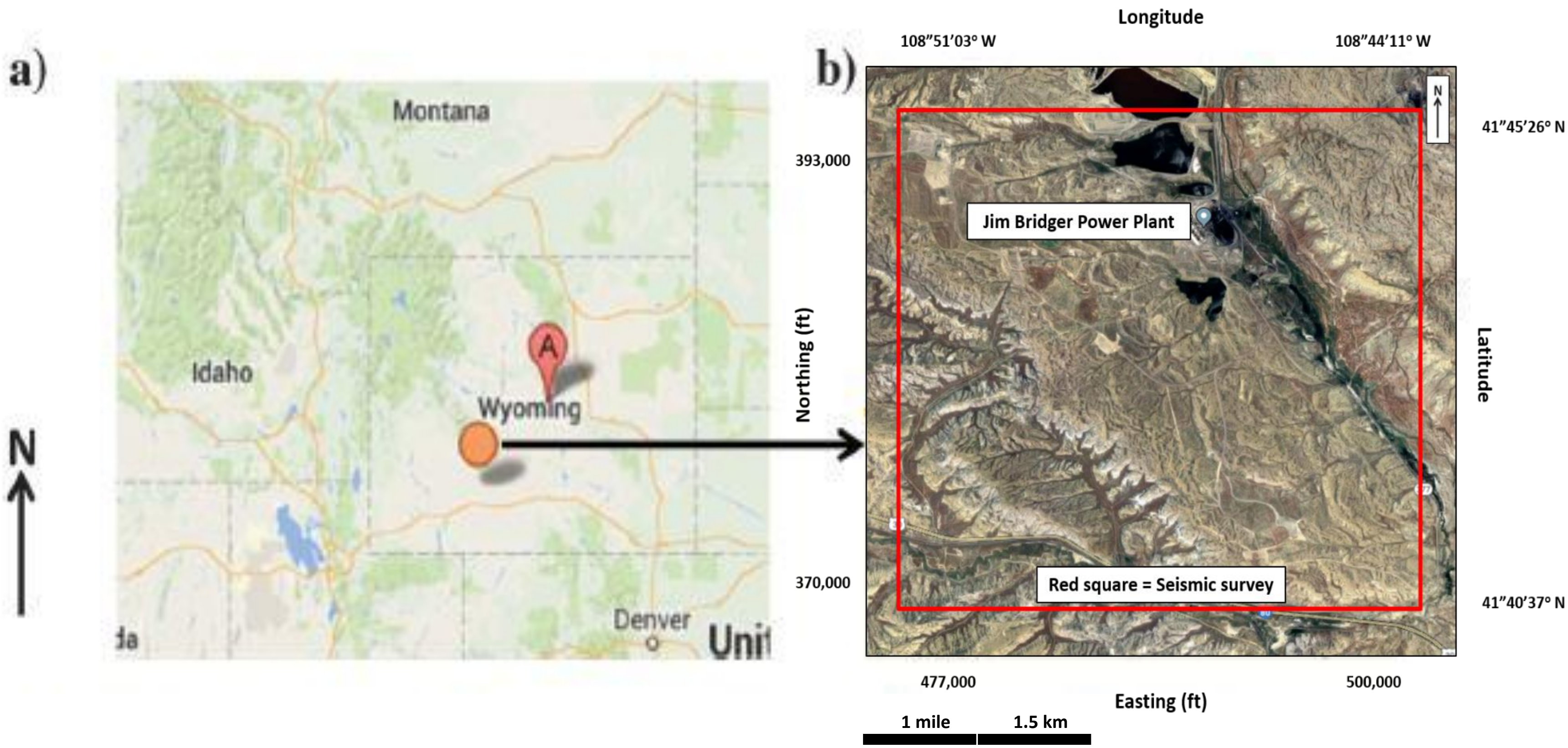

Figure 1.5: Map location of Rock Springs Uplift, Sweetwater County, Wyoming, USA (left) and the location of a seismic survey area (right) (modified from Mallick and Adhikari, 2015).

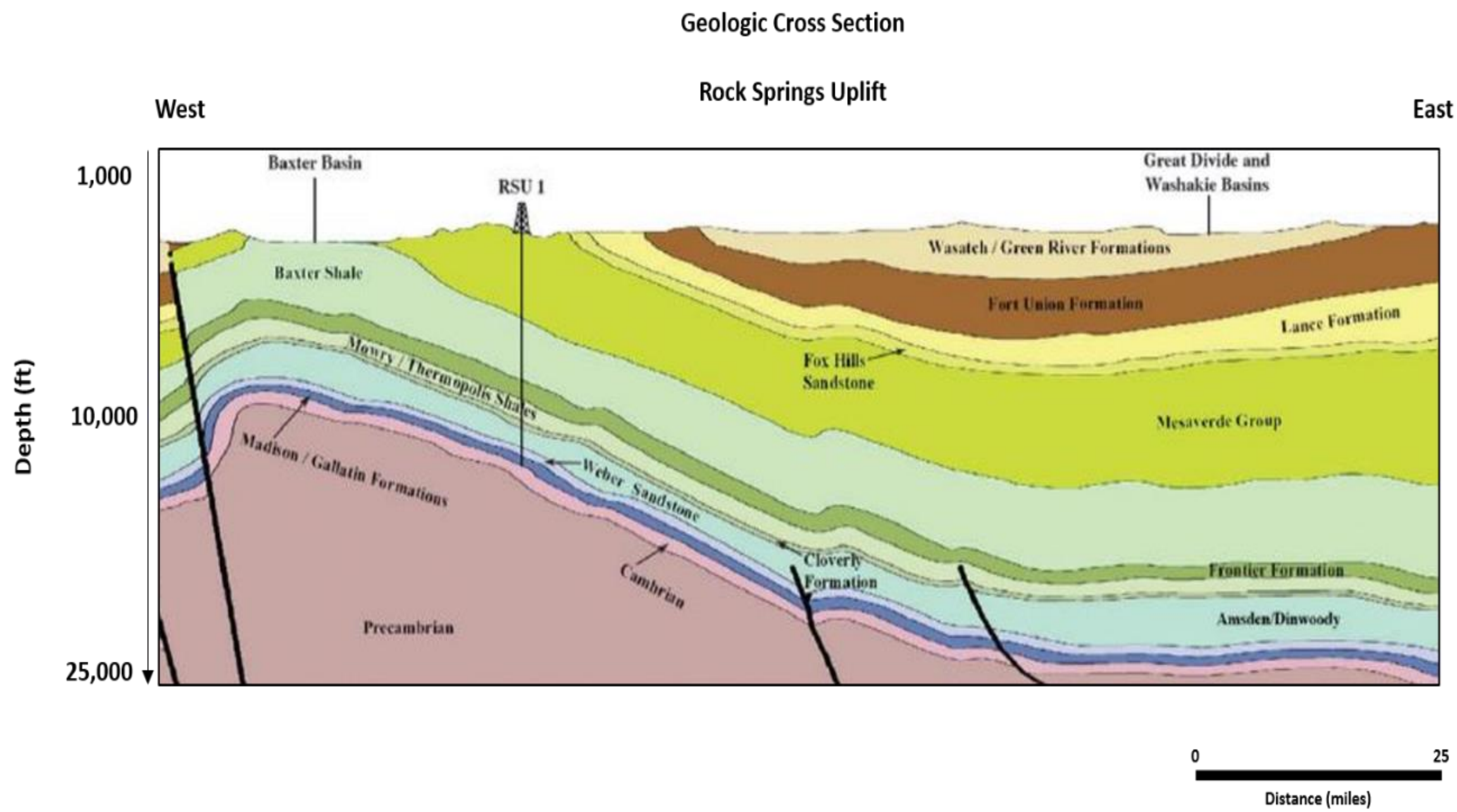

Figure 1.6: Schematic cross-section of the geologic structure and formations near RSU-#1 well (modified from Pafeng et al., 2017).

1.5.1 Weber and Nugget sandstones

The main target reservoirs for carbon dioxide injection are the Jurassic-Triassic Nugget sandstone with an overlying seal formed by the Gypsum Springs Formation and the Pennsylvanian Weber sandstone with the Permian Formation potentially forming an overlying sea (Allis, 2003). The Cretaceous Baxter Shale is a secondary seal, characterized by 6,000 ft (1,829 m) structural closure encompassing about 1,200 square miles (3,108 km^2). Normal faults have been mapped on the surface and drilling has identified many more that are not visible on the surface (Allis, 2003).

The Weber sandstone has an approximate thickness of 657 ft (200 m) and is overlain by the Phosphoria, Dinwoody, and Chugwater formations. These formations are shale-rich which behave as a seal mechanism with approximately 450 ft (137 m). On the other hand, the Nugget sandstone has a thickness of 142 ft (43 m) and is overlain by Gypsum Spring, Sundance, and Morrison/Mowry formations. These shale-rich formations behave as low porosity and permeability seals with an aggregated thickness of 600 ft (183 m). The Baxter shale overlays both Weber and Nugget sandstones, and it is the primary shale seal approximately 3,600 ft (1,097 m) thick. Figure 1.7 displays a stratigraphic column of the geologic formation comprised at RSU-#1 well from 8,500 ft (2,591 m) to the total drilled depth of 12,500 ft (3,810 m).

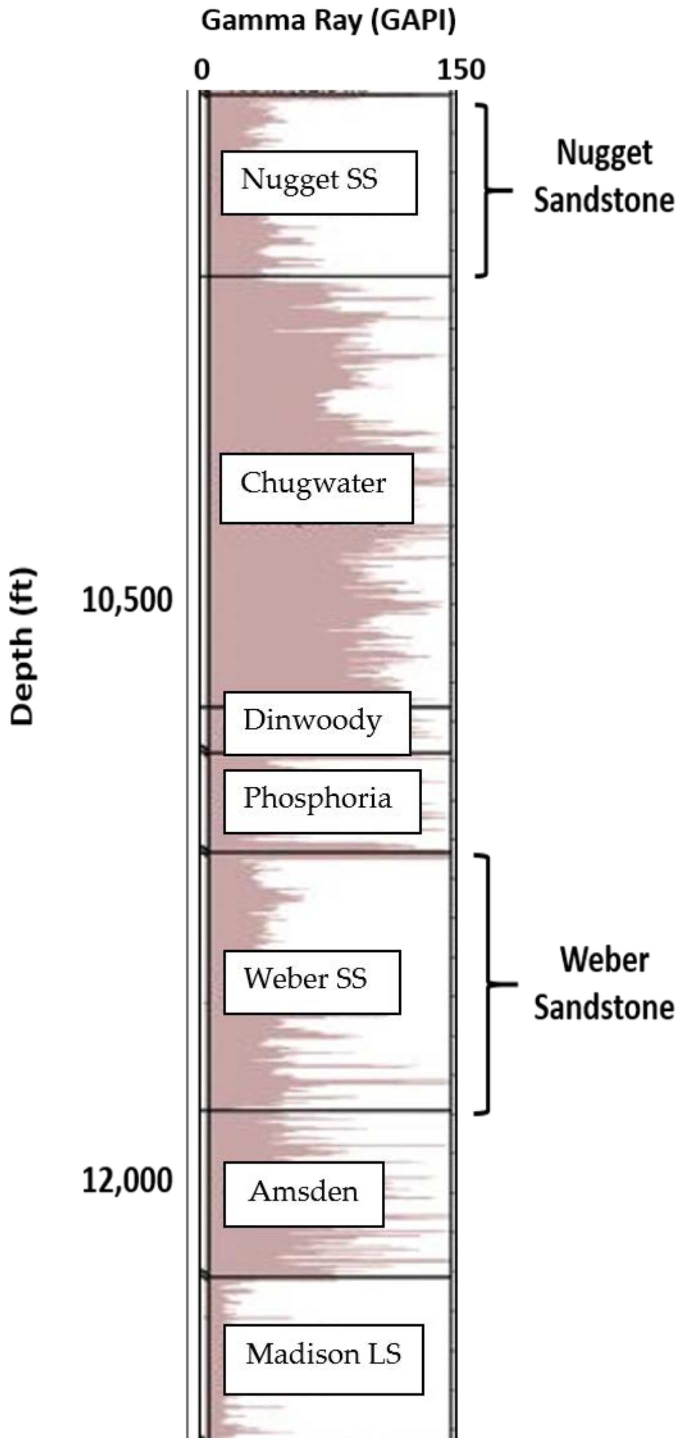

Figure 1.7 Stratigraphic column at RSU-#1 well from 9,000 ft (2,743 m) to total drilled depth of 12,500 ft (3,810 m). Gamma-ray values are displayed for each formation (modified from Pafeng et al., 2017).

1.6 Dataset overview

The datasets provided by Dr. Subhashis Mallick at the University of Wyoming for this study consist of raw pre-stack vertical, horizontal X, and horizontal Y seismic data. Geokinetics acquired the Jim Bridger 3D survey in 2010 and comprised of 25.16 square miles of multi-component seismic data. The energy source was a Vibroseis with an 8-second linear sweep over 6-110 Hz frequency range. There were 2,541 source points. The source point interval is 220 ft (67 m) and source line spacing is 1,320 ft (402 m). The receiver group intervals are 220 ft (67 m) and receiver line spacing is 1,320 ft (402 m) with a total number of geophones of 2,514. Maximum offset in the survey is 19,800 ft (6,035 m). Figure 1.8 shows a survey acquisition map displaying locations of sources (red) and receivers (blue). Table 1.1 lists the main seismic acquisition parameters for the survey.

Table 1.1: Acquisition parameters for the Jim Bridger 3D seismic survey (modified from Mallick, 2015)

Receiver group interval	67 m (220 ft)
Receiver line spacing	402 m (1320 ft)
Total geophone stations	2514
Number of live receiver lines	18 (144 live stations per line)
Source interval	67 m (220 ft)
Source line spacing	402 m (1320 ft)
Total source points	2541
Longest source-to-receiver offset	Approximately 6035 m (19,800 ft)
x- and *y*-coordinate projection	NAD 27, Clarke 1866
x- and *y*-coordinate state plane	Wyoming west central
Survey size	40.4 km^2 (25.16 mi^2)
Source information	
Source description I/O AVH IV vibroseis, four over flag	
Sweep linear 6–100 Hz	
Sweep tapers linear 300–300 ms	

Geokinetics have previously processed the vertical (P-wave) component in 2011. The maximum fold is roughly 120 toward the center of the survey while lower fold area still comprises of about 30-fold. Provided from the previous processing are the refraction statics (calculated based on P-wave refractions) and P-wave migration velocity model. Both refraction statics and velocity models provided are used in the processing the PP and PS reflections.

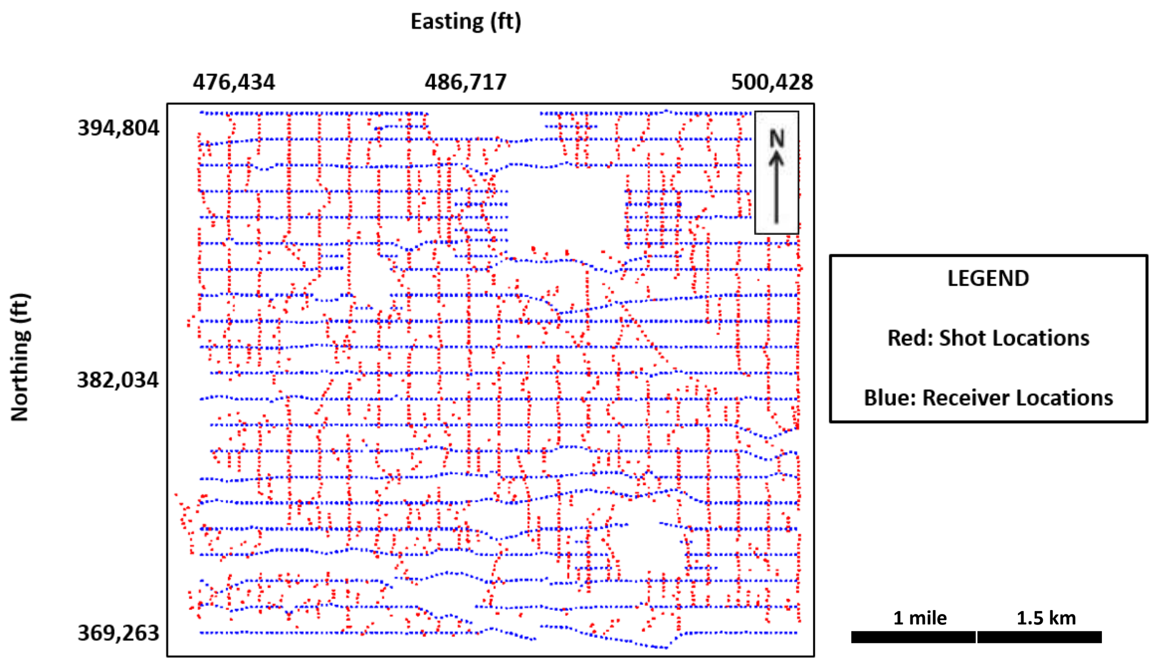

Figure 1.8: Survey map of the multi-component seismic data acquired. Geophones (blue) and shots (red) are displayed.

The well is located near the center of the seismic survey. It was acquired at an elevation of 6,841 ft (1,975 m) and total depth logged is approximately 12,810 ft (3,905 m). The well-log suite provided for this study includes caliper, gamma-ray, compressional sonic, shear sonic, and bulk density logs. Additional logs can be calculated using petrophysical relationships, such as the shale volume, which will be discussed in further detail in Chapter 2. Formations of interest for carbon dioxide sequestration in the area are the Nugget and Weber sandstones, and the logged interval suggest a thickness of approximately 450 ft (137 m) and 700 ft (123 m), respectively. Both geologic formations are characterized by lower gamma-ray values, higher P and S-wave velocities, and density values than the overlying shale sealing lithologies.

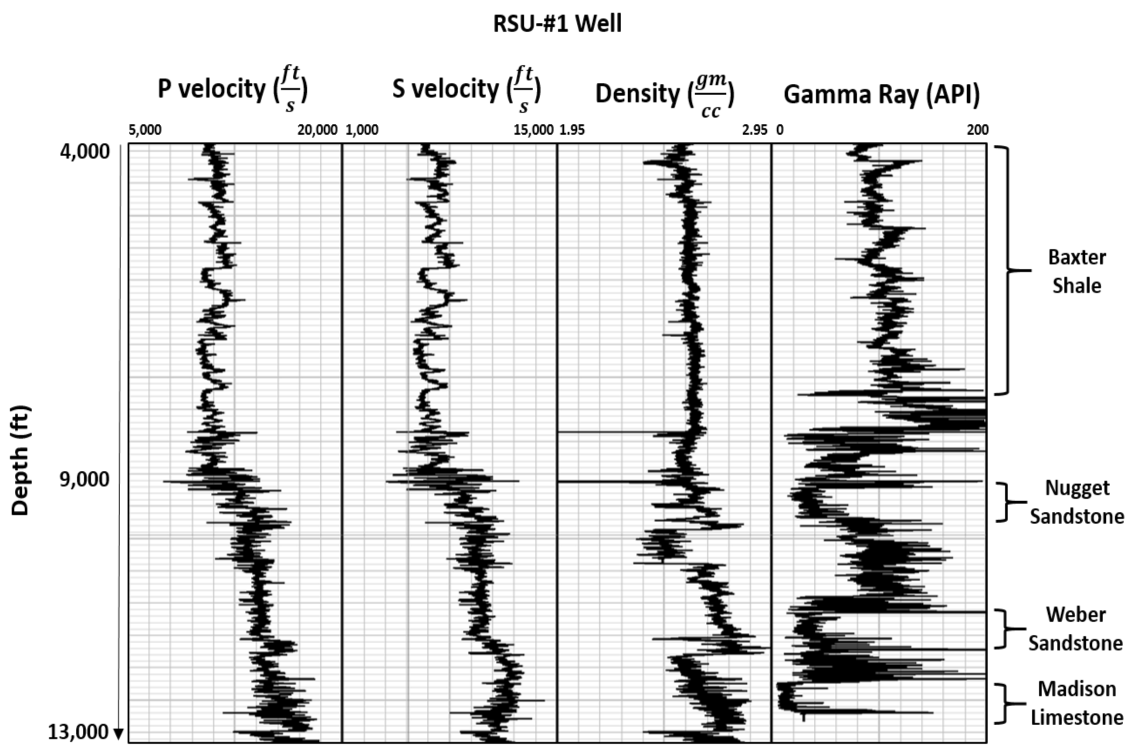

Figure 1.9: Well-logs provided for this study. Logs displayed are gamma-ray, P-velocity, S-velocity, and bulk density. The primary geologic formation intervals are displayed.

1.6.1 Software

The well-log analysis and seismic modeling are carried out using Jtips™ developed by Dr. Fred Hilterman at the University of Houston. For the seismic processing and post-migration conditioning, Ethos processing platform is used, a software currently owned by SAExploration. For the pre-stack simultaneous AVO inversion and elastic attribute interpretation, Paradigm software is used. Additional seismic attributes such as sweetness and spectral decomposition are generated utilizing Transform by Drilling Info.

Chapter 2

Well-log analysis and AVO seismic modeling

The well-logs available at RSU#1 well are used to further investigate the mechanical and petrophysical properties of formations of interest, to obtain relationships of petrophysical properties with elastic parameters in the subsurface. Relationships between the rock properties and the elastic/acoustic response are evaluated and forward models generated from P-wave velocity, S-wave velocity, and density to aid the understanding of the seismic amplitude response of the area.

Petrophysical analysis of the available well-logs aid in the study of the data. Prior to the evaluation of the logs, QC and editing are done to validate the correctness of the data acquired at each interval. The evaluation comprises of an analysis of the target intervals to estimate sand and shale volume percentage, porosity, P-wave velocity, S-wave velocity, σ, among other attributes. A log of $\frac{V_p}{V_s}$ is calculated which aids in the generation of the S-wave velocity volume in the multi-component processing stage. Additionally, to further analyze the petrophysical, geomechanical, and elastic properties of the formations of interest, relationships are generated by cross-plotting any given rock property (i.e. porosity vs. $\mu\rho$) and deriving a least-squares regression. Such relationships are utilized in the interpretation stage for the assessment of carbon dioxide sequestration.

Subsequently, the Amplitude Versus Offset (AVO) modeling phase of the project comprises of synthetic models generated from log data by forward modeling the elastic response of the amplitudes due to the geology in the subsurface. Along with the petrophysical evaluation of the data, wavelets are extracted from seismic, AVO models are generated, and sensitivity analysis in terms of porosity is done to understand the elastic models that accurately represent the area of evaluation. Synthetic models obtained from AVO studies are typically CDP gathers that vary with offsets with or without NMO correction. Such AVO models can be generated for PP and PS reflections, which are compared to the multi-component data. The forward models are calculated using a ray-tracing method or finite difference/element wave-equation methods. The accuracy of the models, computation power, and time depend on the approach chosen for the AVO model generation.

2.1 Petrophysics

2.1.1 Log editing

The role of petrophysics in seismic interpretation has taken a significant leap forward in the past ten years, resulting from essential advances in seismic data processing techniques, particularly seismic inversion, attribute analysis, and amplitude versus offset methods that showed we could estimate reservoir properties from such data (Crain, 2003). Seismic petrophysics is a term used to describe the conversion of seismic data into meaningful petrophysical or reservoir description information, such as porosity, lithology, or fluid content of the reservoir (Crain, 2003). Until recently, this work was qualitative, but as seismic acquisition and processing have advanced, the results are becoming more quantitative. Calibrating this work to well-log “ground truth” can convert the seismic attributes into useful reservoir exploration and development tools. Since there is an infinite number of possible inversions, it is significant to find the one that most closely matched the final edited logs or the computed results from those logs (Crain, 2003).

Geophysical well-logs suffer from many borehole and environmental problems that need to be repaired before being used for calibrating seismic models or seismic interpretations (Crain, 2003). The first step prior to geophysical analysis is the quality control (QC) of well data by ensuring the data does not suffer from incorrect measurement readings, wash-outs, spikes, and anomalies. Such inaccurate information may display non-geologic responses while analyzing reservoir, characteristics such as lithology, fluid saturation, and porosity. After such log anomalies are located and corrected within the well-log, petrophysical relationships can be applied to the logs available to obtain additional geophysical properties. The logs calculated in this study include, but not limited to, $\frac{V_p}{V_s}$, σ, sand volume, λ and μ elastic attributes, and porosity.

2.1.2 $\frac{V_p}{V_s}$ and σ

Compressional and shear sonic logs are measurements of P and S-wave slowness for a given lithologic formation in the subsurface. Such measurements are inversely related to the P and S-wave velocities, respectively; thus, a $\frac{V_p}{V_s}$ can be derived by dividing V_P by V_s obtained from sonic well measurements. Typical values range from 1.4 – 3.0 and can be indicative of fluid saturation due to the S-wave's insensitivity to fluid or porosity due to P-wave's velocity decrease with increased porosity. The Weber and Nugget sandstones have values of 1.71 – 1.85 which indicate a stiffer lithology. The sealing shale lithologies beneath the target sandstones display values of 1.84 – 1.96. An additional log calculated that aids in the characterization of the reservoir is the σ and is directly related to the $\frac{V_p}{V_s}$.

Values of σ typically range between 0 – 0.5 in rocks. The Weber and Nugget sandstones display values of 0.06 and 0.15; meanwhile, the sealing shale beneath has values of 0.24 and 0.37.

2.1.3 Sand volume and porosity

In reservoir characterization studies, it is imperative to characterize the rock by lithologic composition. In siliciclastic reservoir plays, the target sandstones can be analyzed for sandstone and shale percentages in composition. Wave propagation through rock siliciclastic media is heavily influenced by the number of clay compounds in shale strata; thus, to confidently characterize the seismic response, the differentiation between sands and shales is one of the main objectives in a petrophysical analysis.

Gamma-ray (GR) logging is a standard and inexpensive measurement of the natural emission of gamma-rays by a formation. GR logs are particularly helpful because shales and sandstones typically have different gamma-ray signatures that can be correlated readily between wells (Schlumberger Oilfield Glossary, 2019). GR is a log of the total natural radioactivity measured in API units. The measurement can be made in both open-hole and through the casing. The depth of investigation is a few inches so that the log usually measures the flushed zone. Shales and clays are responsible for most natural radioactivity, so the gamma-ray log often is a good indicator of such rocks (Schlumberger Oilfield Glossary, 2019). Shale is usually more radioactive than sand or carbonate. The gamma-ray log can be used to calculate the volume of shale in porous reservoirs. The volume of shale expressed as a decimal fraction or percentage is called V_{sh} (Saputra, 2008). The GR log has several nonlinear empirical responses as well as linear responses. The non-linear responses are based on geographic area or formation age. All non-linear relationships are more optimistic. That is, they produce a shale volume value lower than that from the linear equation (Saputra, 2008). Equation 2 can be used to determine the volume of shale facies by comparing the minimum and maximum baseline gamma-ray values for such facies with the current GR log value. The determination of the volume of sand merely is calculated by subtracting a value of one from the current shale volume value.

$$V_{sh} = \frac{GR_{log} - GR_{min}}{GR_{max} - GR_{min}} \tag{2}$$

Where V_{sh} is the volume of shale and GR_{log} is the gamma-ray value from the log at the depth of analysis. GR_{min} and GR_{max} are the minimum and maximum gamma-ray values for the analysis interval, respectively. From the shale and sand volume values calculated using the GR log, the sand percentages at the Weber sandstone are between 77.8% to 89.8%, while the values at the nugget sandstone are between 73.7% to 96.2% The shale values corresponding to the sealing shale lithology beneath the sandstones are between 16.2% to 49.2%.

In the petrophysical analysis, there is a correlation between the sand volume of lithology with the amount of porosity due to the sphericity of sand grains and subsequent compaction of such creating larger pore spaces in comparison with clays in shales. This study focuses on the analysis of porosity content in the Jim Bridger power plant area for the assessment of carbon dioxide sequestration. Wyllie et al. (1956), derived an equation that relates velocity to porosity measurements. The equation holds that the total travel time recorded on the log is the sum of the time the sonic wave spends traveling the solid part of the rock, called the rock matrix and the time spent propagating through the fluids in the pores (Wyllie et al., 1956). Sonic log measurements of travel time for rock matrix and saturating fluids can be used along with the reading values to estimate the effective porosity in a facies' regime. Wyllie's time average can be used to determine porosity by using Equation 3.

$$\emptyset = \frac{(\Delta t_{matrix} - \Delta t_{meas})}{(\Delta t_{matrix} - \Delta t_{fluid})} \tag{3}$$

Where $\emptyset$ is porosity, Δt_{matrix} is the slowness of the matrix, Δt_{fluid} is the slowness of the saturating fluid, and Δt_{meas} is the slowness at the depth of analysis. Higher porosity values correlate with higher sand volume percentages, as expected. For the Weber sandstone, porosity values range from 2.5% to 10.8%, while for nugget sandstone porosity values range from 6.0% to 18.8%. In comparison, the porosity values for the overlying shale have a lower value with an average of 1.5%.

2.1.4 Shear modulus and lame constant

Elastic attributes calculated from measured logs often provide additional quantitative analysis for a reservoir. Relationships previously described in this chapter are useful for determining the characteristic of specific lithology and facies. While such information is of utmost value in the reservoir, seismic signatures influenced by fluid saturation and rock properties must be differentiated. λ (lame constant) and μ (shear modulus) can be used as a lithology and fluid discriminator by translating P impedance and S impedance values into rigidity and incompressibility. Equation 4 and 5 are used for the calculations of λρ and μρ.

$$\lambda\rho = I^2{}_p - 2I^2{}_s \qquad (4)$$

$$\mu\rho = I^2{}_s \qquad (5)$$

Where λ is the lame constant, μ is the shear modulus, I_p is the P-wave impedance, I_s is the S-wave impedance, and ρ is the density. Cross plot analysis of λρ and μρ can aid in the discrimination of lithology and fluid (Goodway et al., 1997). Figure 2.1 demonstrate typical values of the attributes for different lithologic and fluid compositions. Values observed at the well location range from 13.1 units to 29.2 units for normalized λρ and from 28.8 units to 49.0 units for normalized μρ at the sand-rich intervals. A cross-plot of such values indicate a porous rich sandstone. Figure 2.2 displays the cross-plot of λρ and μρ at the RSU-#1 well location.

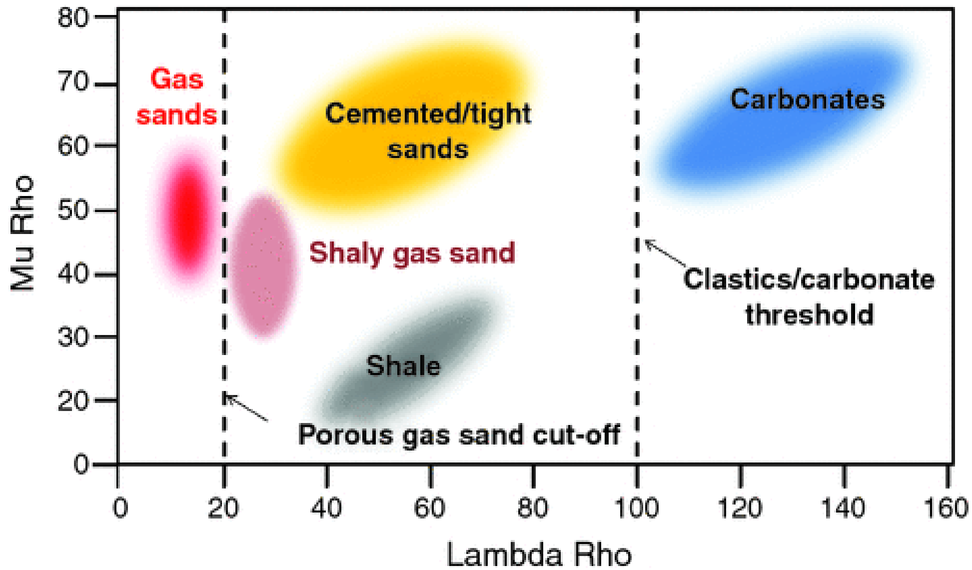

Figure 2.1: λρ vs. μρ theoretical cross-plot defining areas for various lithologies and fluid saturations (from Goodway et al., 1997).

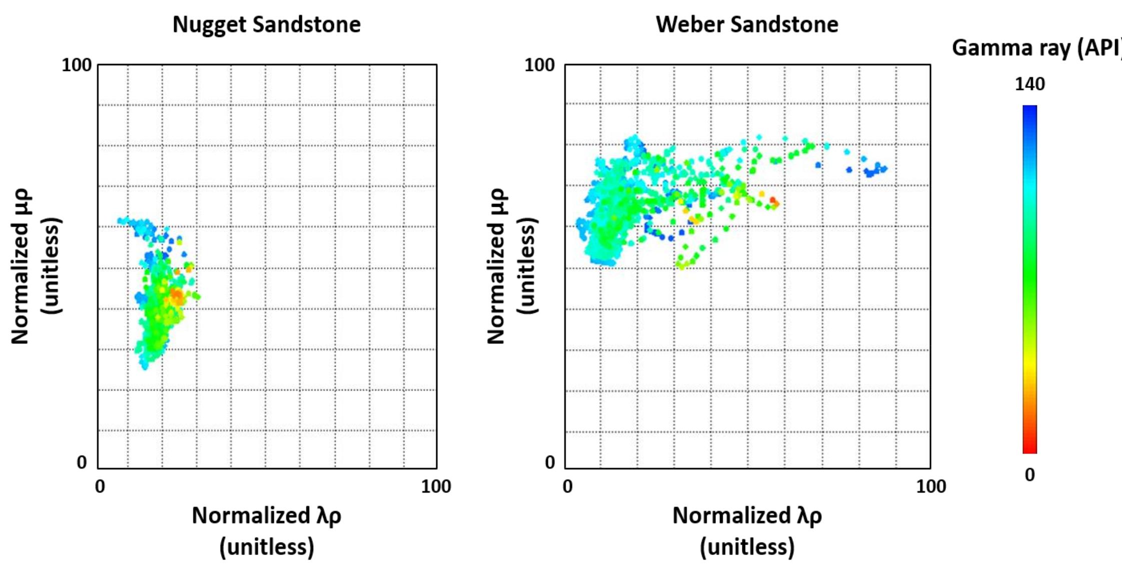

Figure 2.2: λρ vs. μρ at RSU-#1 well for the Nugget sandstone (left) and the Weber sandstone (right). Values are within the 20% cut-off for high-porosity sandstones. Color bar represents gamma-ray values scaled in American Petroleum Institute (API) units.

2.2 AVO seismic modeling

2.2.1 PP AVO modeling

AVO seismic modeling is typically integrated into a geophysical reservoir characterization project to be able to obtain fluid and lithology information from the wave propagation in the subsurface. Modeling is used to compare the seismic response expected at the well location, with the seismic response observed from the seismic data. To be able to relate rock properties from the well-logs to the seismic data, logs such as V_P, V_S, and density can be used for the generation of AVO synthetics. The zero-offset response can be described by the multiplication of P-wave velocity and bulk density, convolved with a wavelet. An approximation of the Zoeppritz equations must be utilized to gain insight into the complexity of wave propagation effects in the subsurface as a function of offset A well-known approximation to Zoeppritz equation used to describe the propagation behavior as a function of offset is the Aki-Richards equation that relates the amplitude versus angle of incidence at a reflection boundary. Aki-Richards approximation for PP reflection coefficients is displayed in Equation 6.

$$R_{pp}(\theta) = \frac{1}{2}\left(1 - 4\left(\frac{\alpha}{\beta}\right)^2 sin^2\theta\right)\frac{\Delta\rho}{\rho} + \frac{1}{2}(1 + tan^2\theta)\frac{\Delta\alpha}{\alpha} - 4(\frac{\beta}{\alpha})^2 sin^2\theta\frac{\Delta\beta}{\beta} \quad (6)$$

Where R_{pp} is the reflection coefficient for PP reflections, ρ is average density, α is average P-wave velocity, β is average S-wave velocity, and Δ refers to the change of the parameter. Finally, θ refers to the average of the incident and transmitted angles.

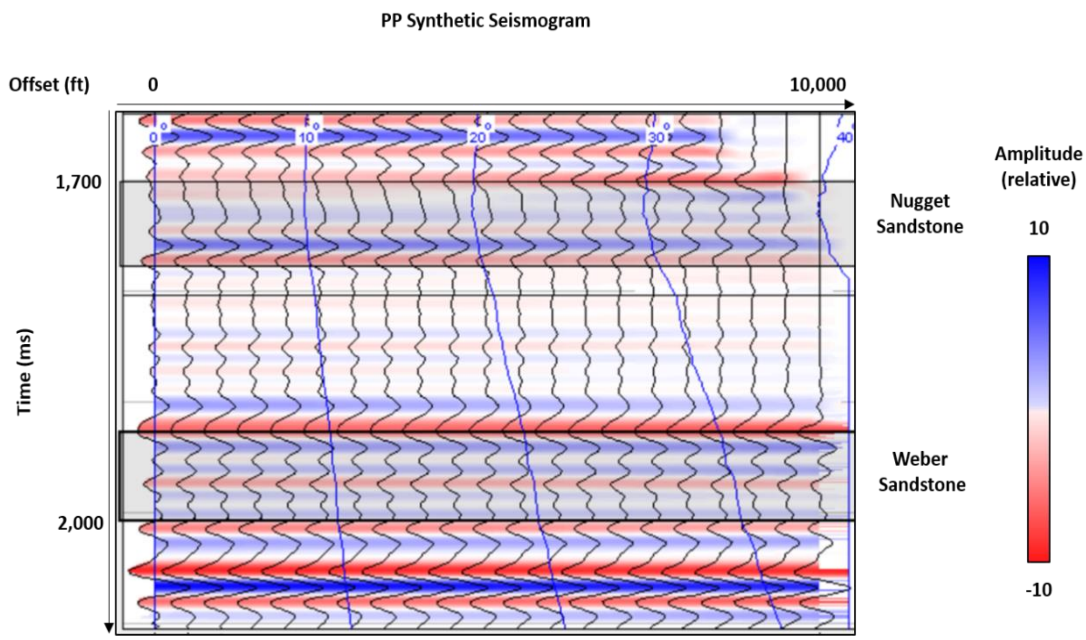

Figure 2.3: PP reflection AVO modeling at RSU-#1 well location. The upper target is defined as the Nugget sandstone, and the lower target is defined as the Weber sandstone.

Figure 2.3 shows the PP reflection AVO model for Nugget and Weber sandstones. The AVO response indicates a slight increase in amplitude with increasing offset, suggesting a class 3 AVO response.

2.2.2 PS AVO modeling

Converted-wave AVO modeling considers the mode conversion of the propagating wave from a P-wave to an S-wave at the boundary interface. Figure 1.3 displays a schematic diagram of a P-wave propagating and mode conversion occurring at the interface. Due to the difference in a wave's propagation from compressional motion (P-waves) to shear motion (S-waves), multiple rock properties can be analyzed for each of them. Fluids have zero rigidity; thus S-waves cannot travel through fluids. In principle, shear-wave velocities are significantly affected by lithologic properties and are much less affected by the saturating fluid within the rock matrix. Conversely, compressional primary waves are both affected by lithology and fluid saturation.

A distinct Zoeppritz approximation must be used, incorporating effects of mode conversion and S-wave propagation to be able to characterize the converted-wave amplitudes as a function of offset. Equation 1 displays the PS AVO equations used for such; thus, the converted-wave response depends only on the contrasts in shear velocity and density. This is substantially different and simpler than the PP case; where the response depends upon contrasts in the compressional velocity, shear velocity, and density (Gray, 2003).

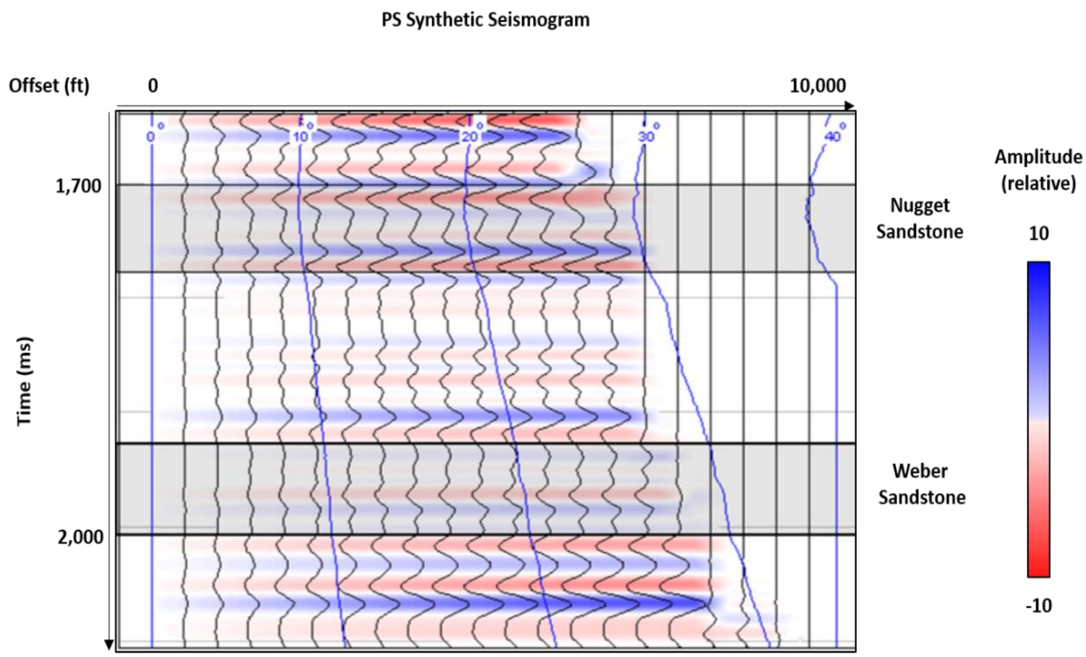

Figure 2.4: PS reflection AVO modeling at RSU-#1 well location. The upper target is defined as the Nugget sandstone, and the lower target is defined as the Weber sandstone.

Figure 2.4 shows the PS reflection AVO model for Nugget and Weber sandstones. The AVO response indicates small negative amplitudes in the near offsets and increasingly negative amplitudes in far offsets, suggesting a Class 3 AVO response.

2.3 Geophysical attributes

Rock elastic attributes derived from geophysical data, such as seismic and well-logs, are of extreme value when analyzing rock properties in the subsurface. If the seismic AVO response is known at well location, information can be inferred such as lithology, fluid saturation, shale volume estimation, and porosity. Pre-stack seismic data can be used to generate attributes that are a function of seismic amplitude variations with offset. These are attributes strictly inferring layer boundary properties and can be useful for reservoir characterization. Well-logs display continuous measurements at the well location, and layer attributes can be calculated characterizing rock and fluid properties throughout the stratigraphic column. Table 2.1 displays a list of boundary and layer attributes calculated for this study

Table 2.1: List of layer and boundary attributes analyzed in this study

Layer Attributes	Boundary Attributes
Mu-rho vs. Lambda-rho	Mu-rho vs. Lambda-rho
Poisson's Ratio vs. AI	Poisson's Ratio vs. AI
SI vs. AI	SI vs. AI
P velocity vs. Density	Gradient vs. Normal Incidence
P velocity vs. Porosity	Fluid Factor vs. AI
Bulk Modulus vs. AI	Poisson's Reflectivity vs. AI

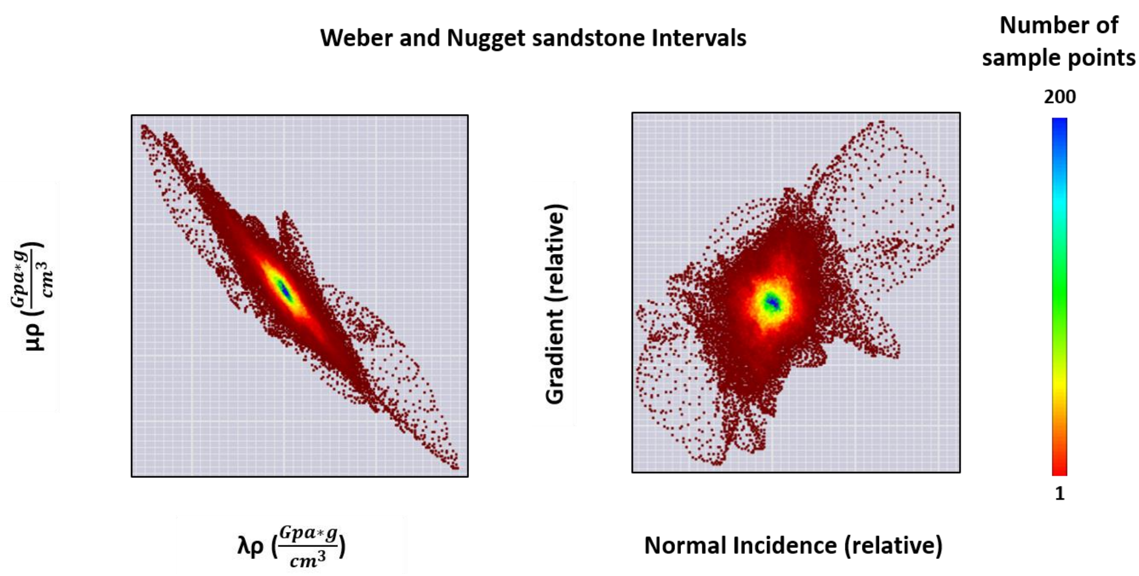

Figure 2.5: Boundary attributes from seismic data. λρ vs. μρ (left) and Normal Incidence vs. Gradient (left). The color bar represents the number of sample points in the graph.

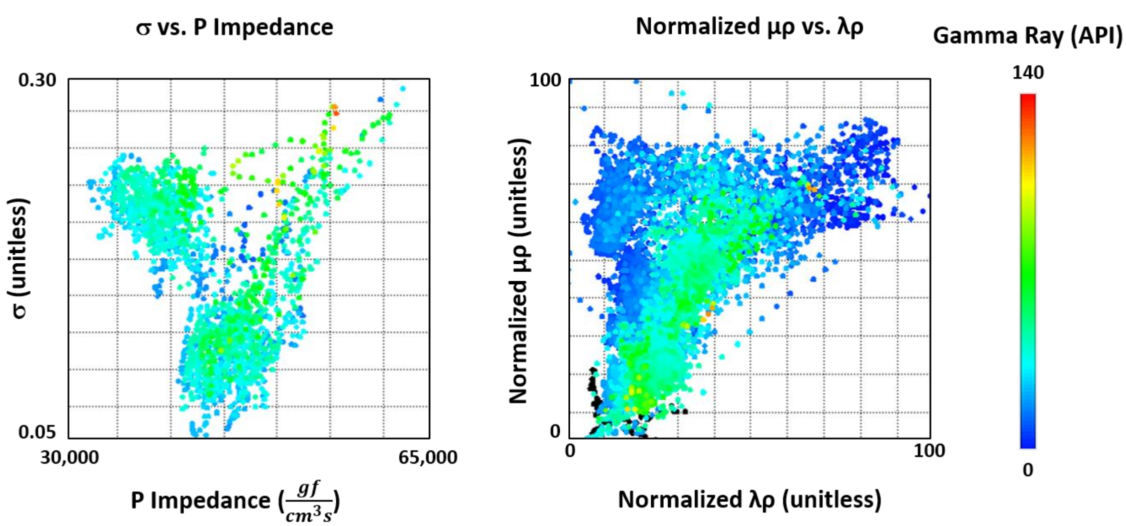

Figure 2.6: Layer attributes from well-logs. AI vs. σ (left) and normalized λρ vs. μρ (right). The color bar represents gamma-ray values.

2.4 Sensitivity analysis

2.4.1 Porosity

Sensitivities of reflection coefficients to each bulk elastic parameter can be computed as the partial derivative of the seismic reflectivities relative to each parameter (Gomez and Tatham, 2005). The sensitivity of reflectivity to porosity variations are calculated to determine the seismic signature of target sandstones with increased or decreased porosity for carbon dioxide sequestration purposes. According to Wyllie's time average equation (1954), porosity can be calculated as a function of velocity and density. To be able to characterize the seismic response due to changes in porosity, the variations in both velocity and density for a specific target sandstone are be calculated. Wyllie's time average equation has the form of Equation 4.

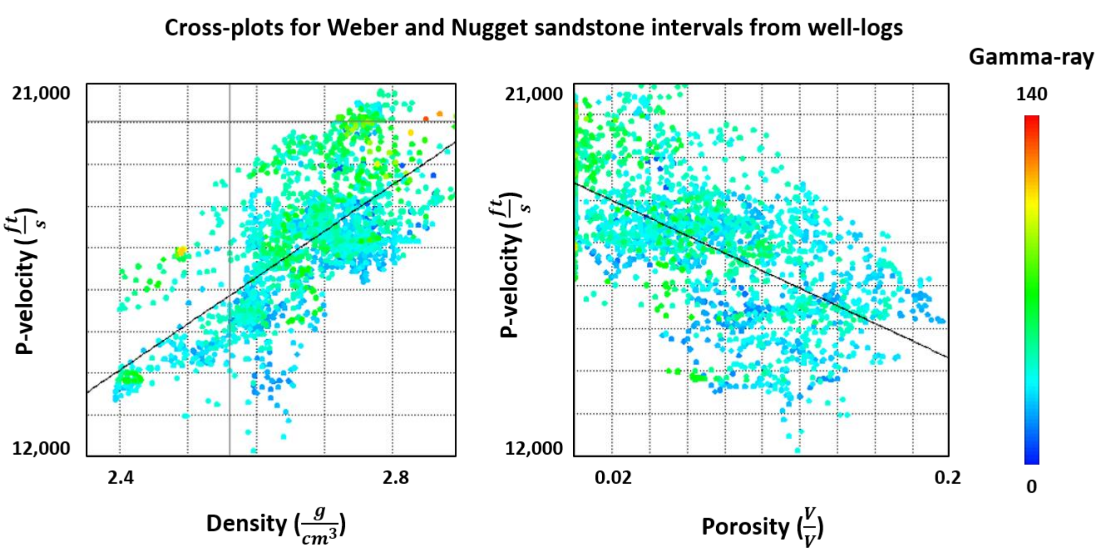

Figure 2.7: Rock physics relationships calculated for sensitivity analysis. V_P vs. Density (left) and V_P vs. Porosity (right). The color bar represents gamma-ray values.

In Figure 2.7, mathematical modeling utilizing Wyllie's time average relation is done for determining changes in porosity as a function of velocity and density for Weber sandstone. The graph on the left displays the relationship between velocity and density for Weber sandstone. Note the tendencies of velocity increase with the increase of density. On the graph to the right, a velocity to porosity relationship is displayed. Conversely, note the decrease in velocity as porosity is increased, as expected. By obtaining such relationships, modeling of increase/decrease of porosity is achieved.

2.4.2 Elastic attribute response

To obtain a reliable value for velocity and density for the Weber sandstone prior to the sensitivity analysis, blocking of the well-logs is done by averaging the log values throughout the sandstone interval. Similarly, this is done to the shale strata beneath to obtain the average velocity and porosity values of the overlying shale. The values obtained for the sensitivity analysis for the sandstone are V_P of 17,813 ft/s (5,430 m/s) and density of 2.55 g/cc, while the values to model a 5% porosity increase correspond to V_P of 16,184 ft/s (4,933 m/s) to a density of 2.48 g/cc. Figure 2.8 displays the blocked logs and the response of elastic attributes calculated for the case of 5% porosity increase. For the sensitivity analysis for this study, as porosity is increased the expected elastic response in terms of σ and $\mu\rho$ attribute is decreased significantly. In such a case, the expected seismic response for a higher porosity sandstone for CO_2 sequestration requires a decrease of both σ and $\mu\rho$ when elastic attribute analysis is done.

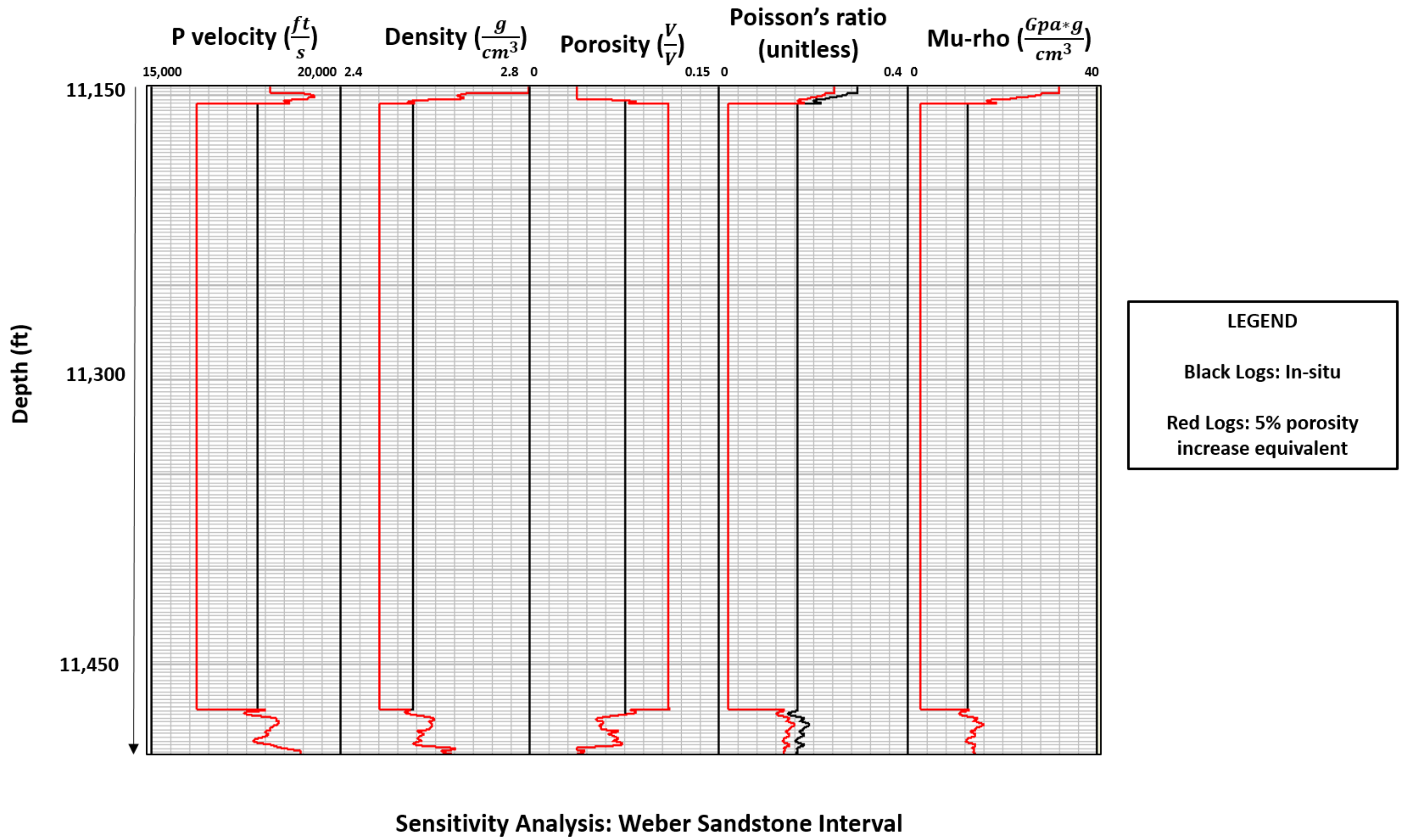

Figure 2.8: Sensitivity analysis results for V_P, density, porosity, $\mu\rho$, and σ. Black curve denotes in-situ logs, and red curves denote the logs with 5% porosity increase.

Chapter 3

PP reflection seismic processing

Seismic processing of conventional PP seismic data allows for the generation of a reliable image of the subsurface used in oil and gas prospecting or carbon dioxide sequestration studies. In this chapter, the time processing workflow for the vertical geophone acquired seismic data is described. Shot gather data processed by Geokinetics in 2010 is used as a starting point for Offset Vector Tile (OVT) generation prior to migration for the preservation of azimuthal amplitude information. Posterior to conventional time processing, remnant random/coherent noise and small errors in the velocity model used for NMO may still be present in the data. Generally, conditioning the gathers after processing is recommended for obtaining a subsurface seismic image that most accurately represents the actual geology. Gather-conditioning post-processing sequence utilized includes random/linear noise removal, residual velocity correction, removal of unwanted coherent energy (i.e. multiples), *f-k* filtering, and amplitude normalization. Figure 3.1 displays the time processing sequence while Figure 3.2 shows post-migration seismic conditioning of vertical geophone seismic data.

3.1 PP seismic processing workflow

3.1.1 Time processing workflow

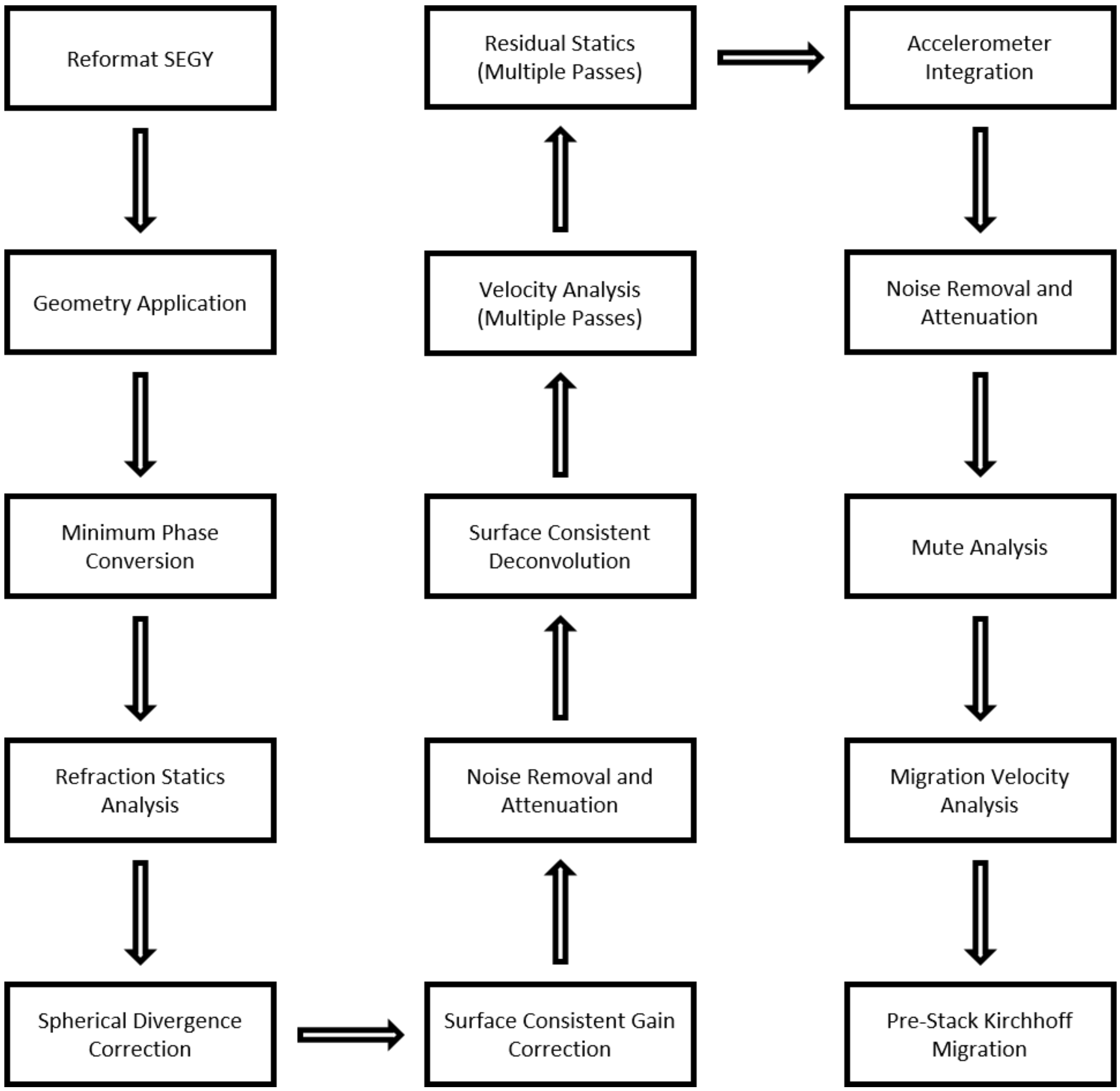

Figure 3.1: Time processing workflow for P-wave reflection seismic data.

3.1.2 Gather-conditioning workflow

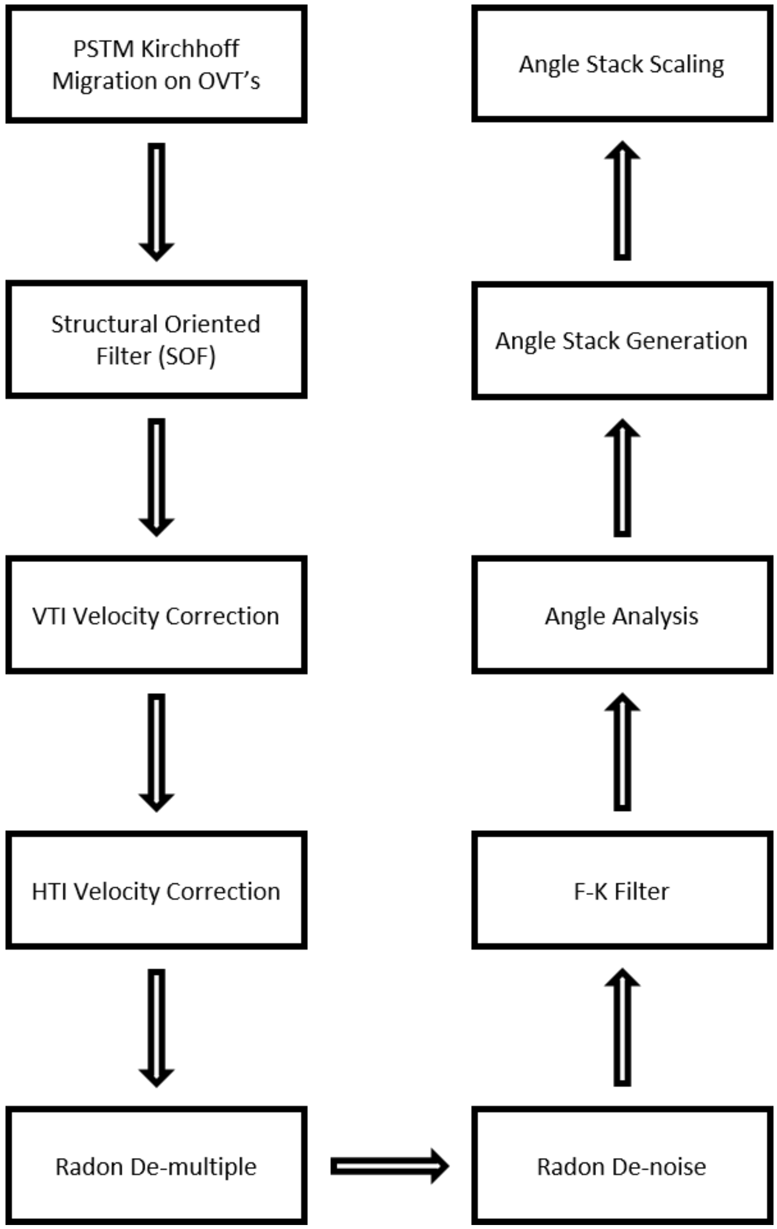

Figure 3.2: Representation of the seismic gather-conditioning workflow.

3.2 Offset vector tiles (OVT)

3.2.1 OVT definition

The offset vector tile (OVT) is a pre-stack seismic gather type and a seismic processing technology proposed by Vermeer (1998). The primary purpose of OVT processing is constructing a special common-reflection point gather with diversity in offsets and azimuths. For seismic surveys acquired as Wide-Azimuth (WAZ) seismic, OVT processing is an effective 3D seismic exploration technique used to improve quality and seismic resolution while preserving valuable information regarding offset and azimuth.

The basis of OVT technology is the “tile”. A seismic geometry system (or a seismic survey) can be divided into a set of tiles. A tile is a small cell with the shape of a rectangle (if the receiver lines are perpendicular to the source lines) or a parallelogram (if the receiver lines are not perpendicular to the source lines). An OVT gather corresponds to a tile. Each OVT cell is composed of several common midpoints (CMP) within a limited source and receiver range. These two ranges also restrict its offset and azimuth ranges (Shifan et al., 2018). For this survey, 60 OVTs with unique offset and azimuth information were calculated for migration and post-migration seismic conditioning.

The Jim Bridge 3D-3C survey has been acquired with reliable azimuth and offset ranges in the seismic acquisition geometry, thus making the data able for OVT processing. In Figure 3.3, a rose diagram shows azimuth and offset information for the survey. The diagram shows azimuths and offsets in the range 0 - 360 degrees and 0 – 22,000 ft (6,705 m) offset.

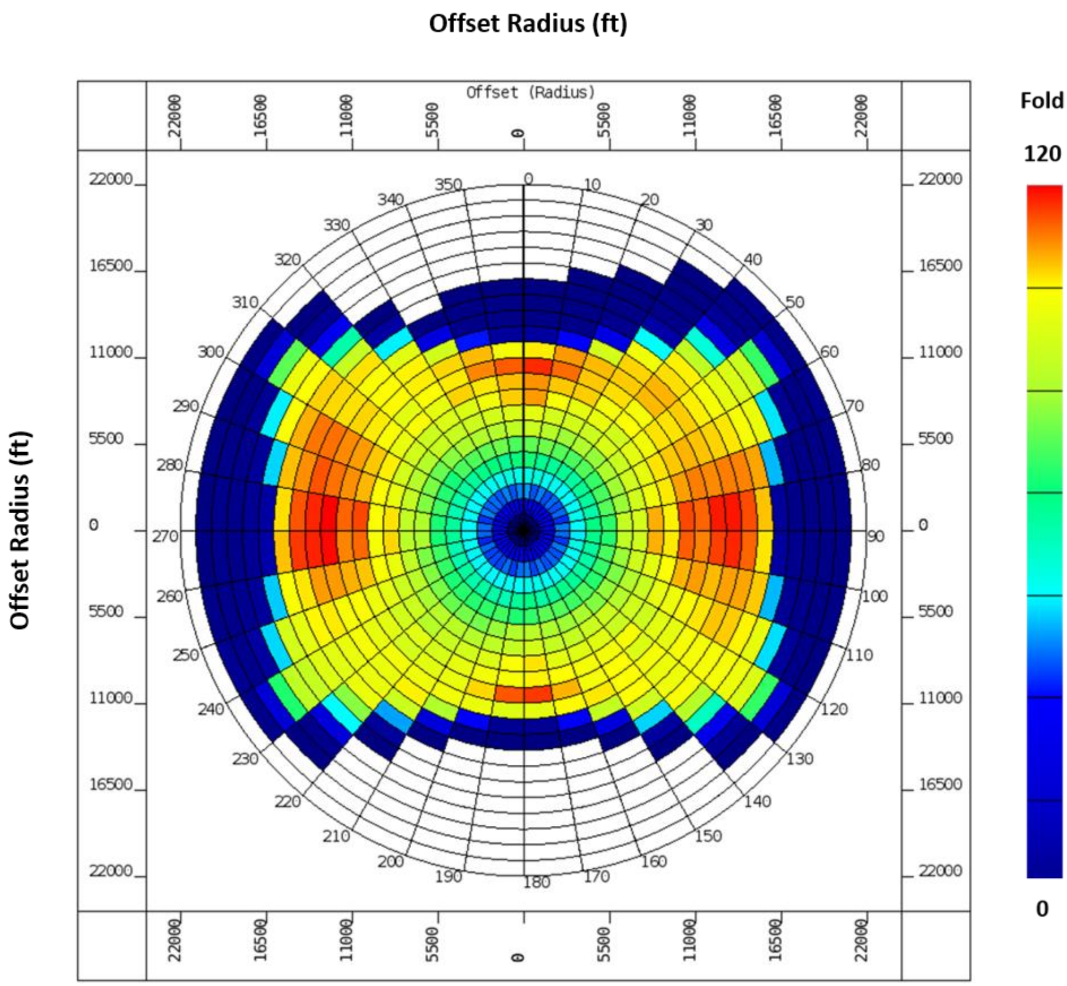

Figure 3.3: Rose diagram of azimuth – offset distribution for the Jim Bridger 3D survey. The color bar represents the fold number.

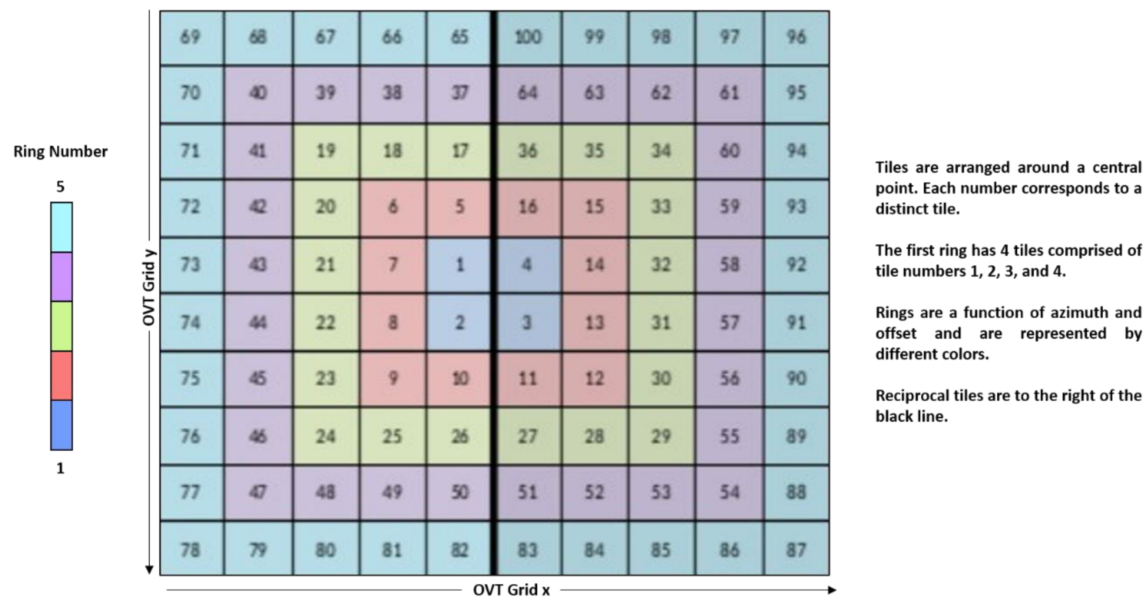

Figure 3.4: Offset vector tiles (OVT) theoretical distribution. The color bar represents the ring number.

Figure 3.4 displays a diagram for the assignment of each offset vector tile. Each tile corresponds to a unique azimuth – offset range and traces may be placed within each of these distinct bins. Only the reciprocal tiles are used to increase the number of traces within each bin. That is, azimuth values ranging from 0 – 180 degrees are used to avoid redundant azimuthal information. Furthermore, to maximize fold the data can be sorted in OVT sectors where a range of tiles are utilized for a larger azimuthal range such as encompassing bins within 15-degree sectors. After offset vector tiles area assigned, the CDP gathers can be sorted in terms of offset and azimuth to observe the changes in velocity with respect to offset, and azimuth corresponding to anisotropy for primary reflectors, such as CDP gathers in Figure 3.5.

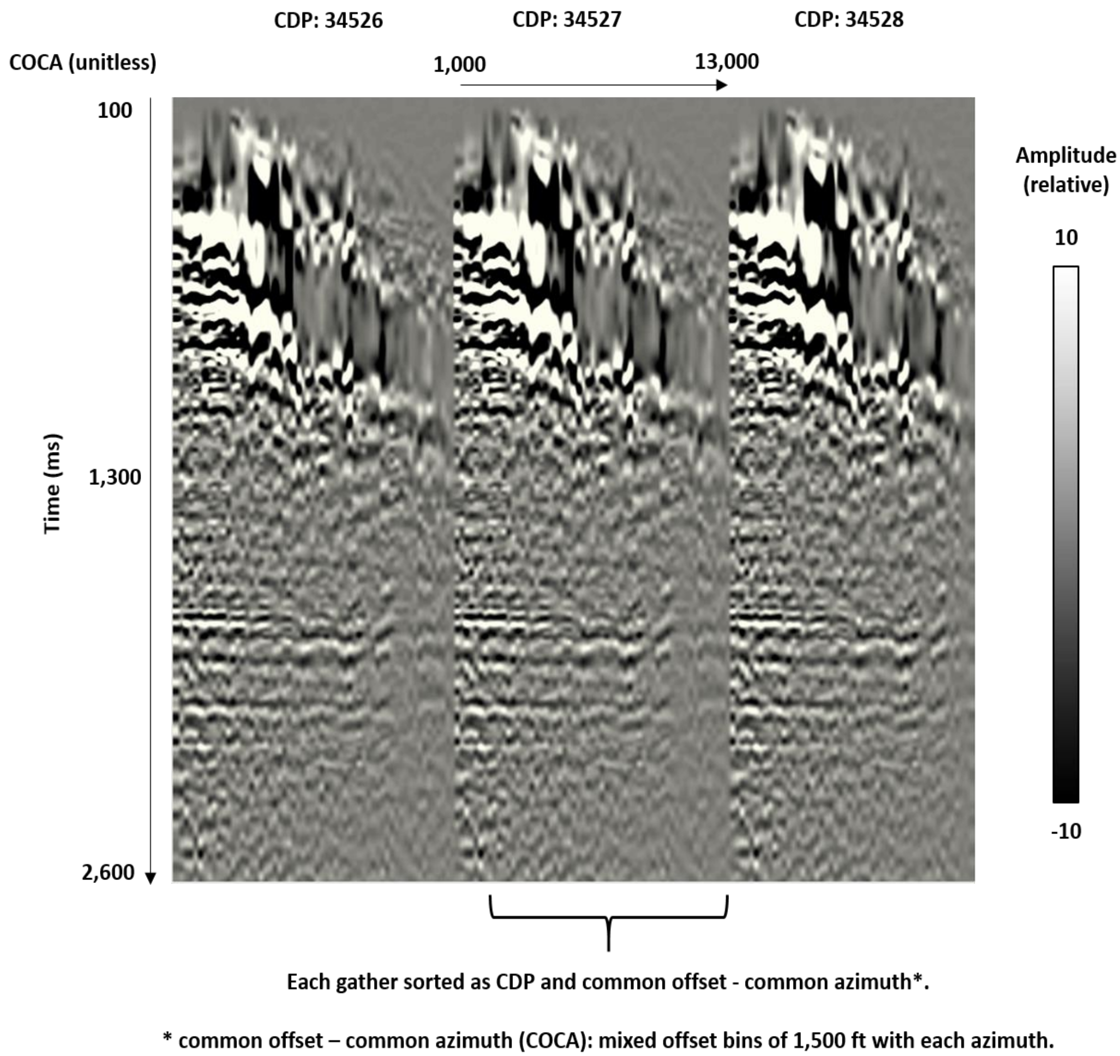

Figure 3.5: CDP gathers sorted as common offset and common azimuth to demonstrate the effect of azimuthal velocity variations. COCA values range from 1,000 to 13,000 for each CDP gather.

3.2.2 Kirchhoff migration on OVTs

Seismic migration is one of the most critical processing steps for subsurface imaging because seismic events are geometrically re-located in either space or time to the location the event occurred in the subsurface rather than the location that it was recorded at the surface, thereby creating a more accurate image of the subsurface (Yilmaz, 2001). Migration moves dipping reflections to their correct subsurface positions and collapses diffractions, thus increasing spatial resolution and yielding a seismic image of the subsurface. The goal of migration is to make the stacked section appear similar to the geologic cross-section in depth along a seismic traverse (Yilmaz, 2001). Kirchhoff time migration is applied to each calculated offset vector tile volume. Thus, the seismic energy will be imaged to represent geologic structure while preserving information regarding azimuth and offset, which may be useful in anisotropic studies. Table 3.1 displays parameters used for the Kirchhoff migration.

Table 3.1: Parameters used for the Kirchhoff Pre-stack Time Migration (PSTM)

Parameter	Value
Maximum angle (degrees)	60
Maximum aperture (ft)	30,000
Taper (percent)	20
Offset bin type	OVT

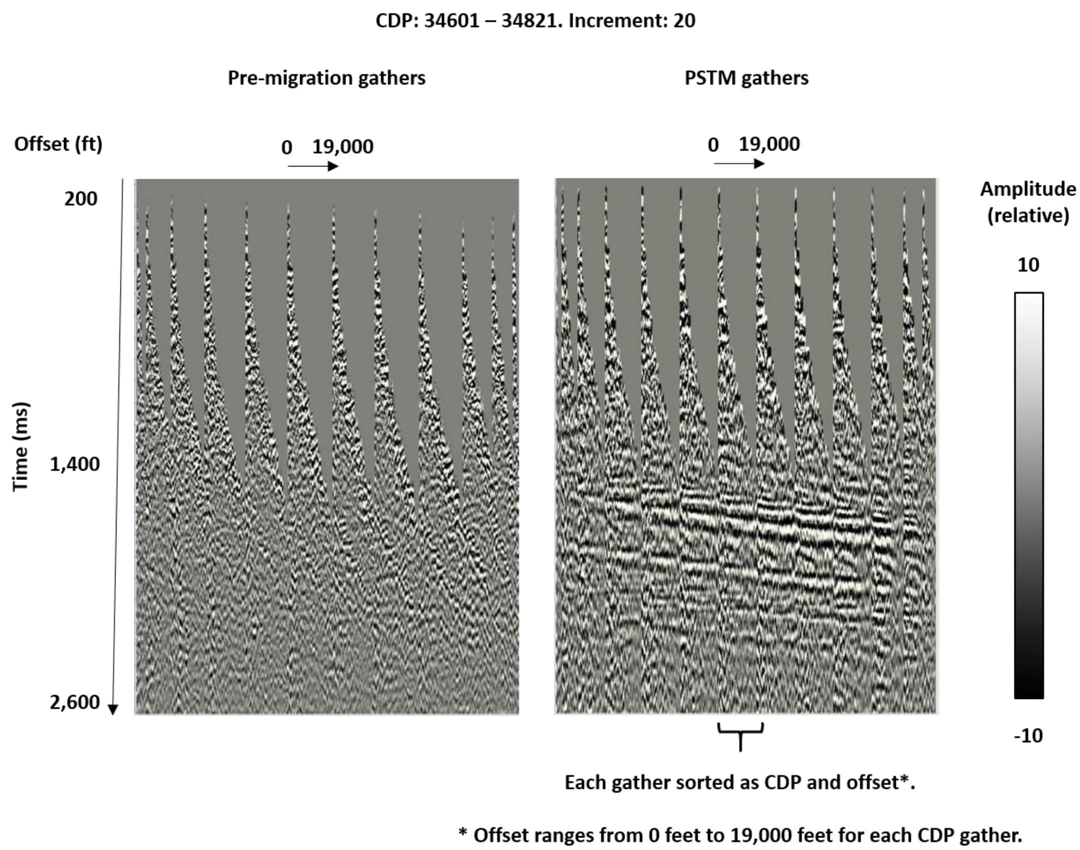

Figure 3.6: CDP gathers display for the Kirchhoff PSTM before (left) and after (right). Offset ranges from 0 – 19,000 ft for each CDP gather.

Prior to the application of Kirchhoff migration, reflection events in the CDP gathers were scarce and very dim in amplitude. Figure 3.6 displays the results after the Kirchhoff migration is applied to each OVT and sorted to CDP gathers. The migration algorithm collapses the reflection energy to the correct location in the subsurface, and the geologic events are wide-spread, especially for the target reflection events for the Nugget and Weber sandstones at a time range of 1600 – 1900 ms.

3.3 Gather-conditioning

3.3.1 Structure-oriented filter

Structure-oriented bilateral filtering (SOF) is the first processing step applied to the seismic data post-migration. SOF is a true 3D signal-to-noise enhancement algorithm for post-stack data which estimates the signal-to-noise value using a grid of surrounding traces performing structure-oriented-edge-preserving filtering on the input volume. SOF determines signal by finding the dipping plane of maximum semblance centered on the output point. It determines noise with an amplitude median/trim process exponentially by using their radial distance from the output point. By finding the dipping plane of maximum semblance, the algorithm creates a structural edge-preserving filter that removes incoherence noise from the data, thus creating a clearer more defined structural image of the subsurface. The parameters used for the algorithm are displayed in Table 3.2.

Table 3.2: Parameters used for the Structure-Oriented Bilateral Filtering (SOF)

Parameter	Value
Traces in Inline direction	5
Traces in Crossline direction	5
Dip scan Inline direction (ms)	20
Dip scan Crossline direction (ms)	6

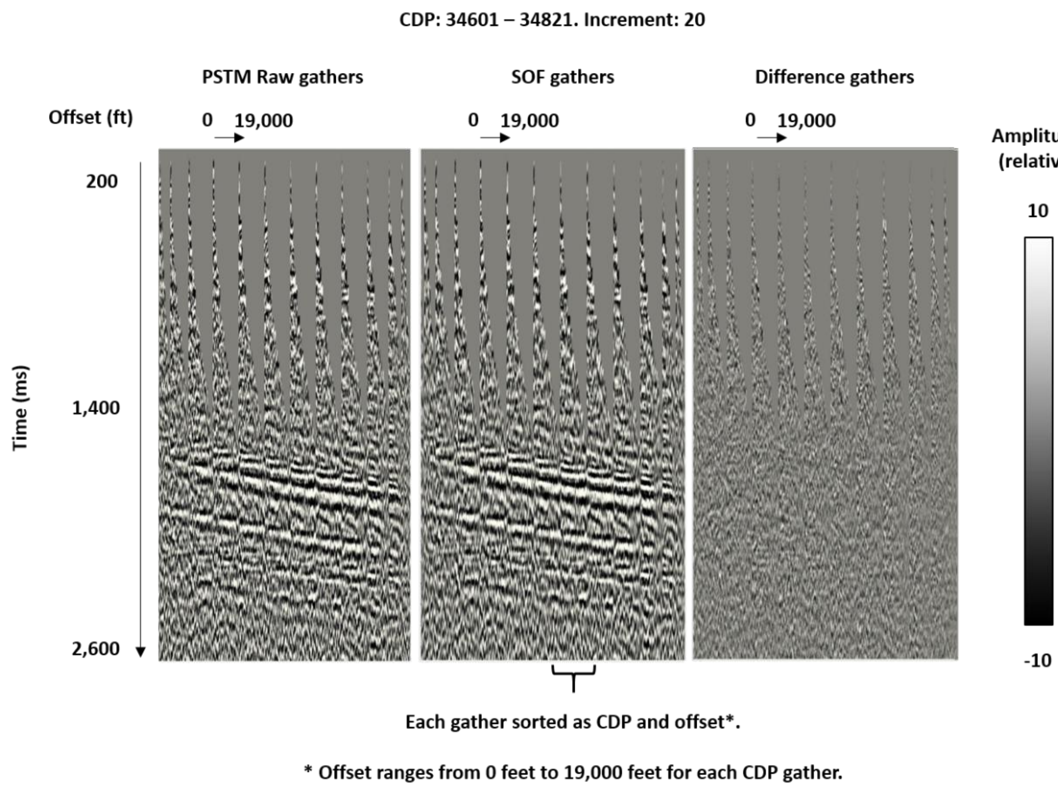

Figure 3.7: CDP gathers display for Structure-Oriented Filtering (SOF) before (left), after (middle), and difference (right). Offset ranges from 0 – 19,000 ft for each CDP gather.

The algorithm uses five traces in the inline and crossline direction for the smoothing operator while utilizing a maximum up/down dip of 6 ms to find the most coherent energy of the geologic structure. Figure 3.7 displays the before, after, and difference of the application of the SOF algorithm. It is evident that most random and incoherent noise is subtracted from the CDP gathers, which is expected. The difference display is a quality-control step taken to ensure that primary reflection events are not affected to ensure the preservation of AVO for later interpretation work.

3.3.2 VTI and HTI corrections

Vertical Transverse Isotropy (VTI) and Horizontal Transverse isotropy (HTI) induce changes in the propagating velocity of the waveform depending on the direction of travel. Such changes in anisotropy within the survey will create varying velocities required to flatten the reflection events on CDP gathers within the seismic volume. Anisotropic velocity variations due to VTI and HTI must be accounted for proper imaging of the geologic structure.

The VTI correction algorithm calculates the variations of velocity from Normal Incidence (NI) and Poisson's Reflectivity (PR) on a CDP gather. The algorithm by Swan (2001) describes the method for computing the residual velocity corrections based on AVO attributes for flattening the gathers. The technique typically corrects a 2% error in the RMS field. If the error is larger than 2%, then this method can be used in iterations (Swan, 2001). The algorithm outputs a volume of velocity changes which are then smoothed and added to the original velocity field. The initial velocity field is removed for NMO correction, and the new one is applied.

Azimuthal anisotropy, also known as HTI, produces a pattern of slowness versus azimuth which is elliptical. For azimuthal anisotropy corrections, the algorithm decomposes arrival time "errors" caused by anisotropy into parameters estimating the elliptical anisotropy and uses least-squares fitting to determine the parameters which best define the anisotropic ellipse.

Table 3.3: Parameters used for the VTI and HTI velocity corrections

VTI Parameters		**HTI Parameters**	
Time (ms)	Mute in p (ms)	Parameter	Value
Velocity change (%)	12	Min. Number of data values	3
Main frequency (Hz)	35	Minimum fit (%)	35
Time window size (ms)	48	Minimum velocity diff. (%)	1

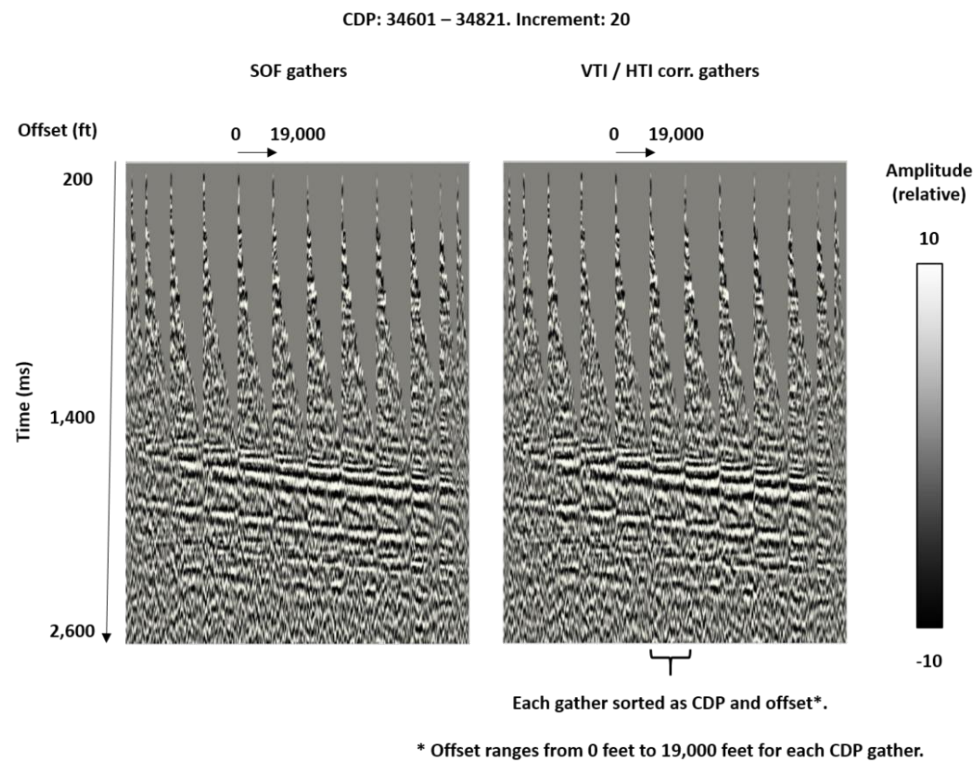

Figure 3.8: CDP gathers display for VTI/HTI velocity correction before (left) and after (right). Offset ranges from 0 – 19,000 ft for each CDP gather.

Table 3.3 shows the parameters used for the VTI and HTI corrections. For the VTI algorithm, a maximum of 12% change in velocity can be calculated for seismic energy with a central frequency of 35 Hz. A running window of 48 ms is used for the statistics calculations. The stack response is expected to improve significantly after applying corrections for vertical and horizontal anisotropy because the velocity errors from azimuthal variations are minimized and flattening of the gathers is expected. The stack should have increased focusing of events by increasing the amplitude for each CDP location while improving the reliability of the AVO response displayed in the stack. Figure 3.8 displays the CDP gathers before and after the anisotropic correction. It is evident the primary reflection events are flatter after the anisotropic corrections. Figure 3.9 shows the interval velocity field before and after the anisotropic velocity corrections.

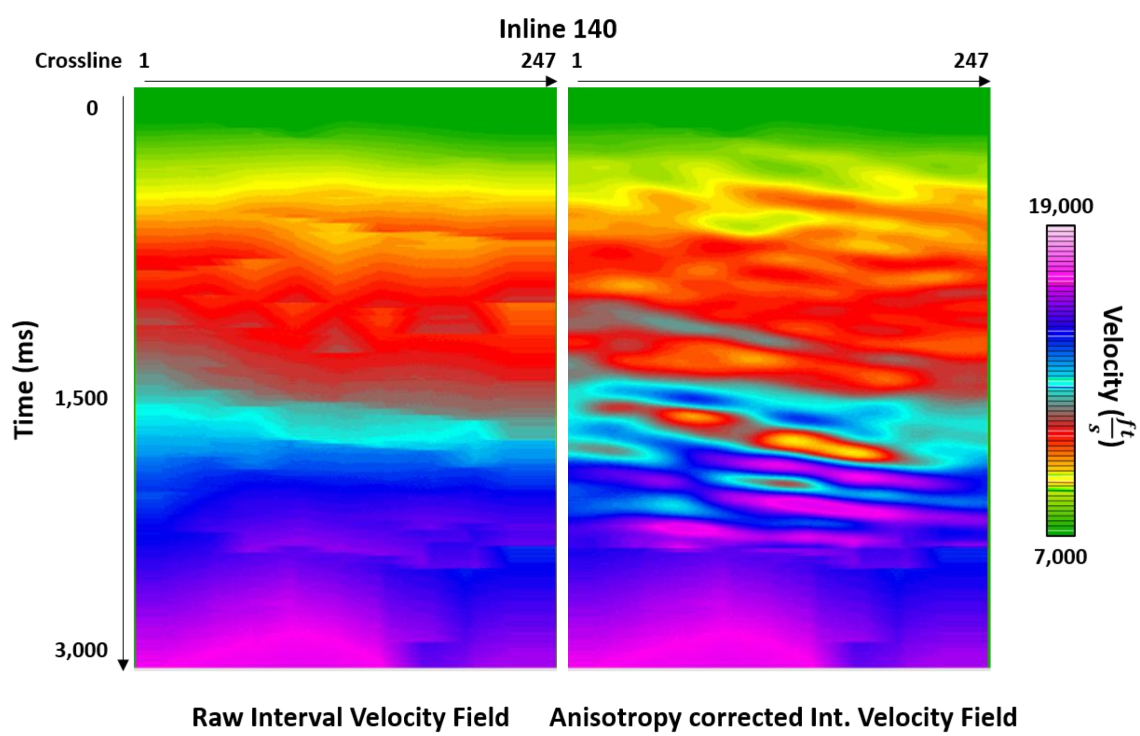

Figure 3.9: P-wave interval velocity field before (left) and after (right) the HTI/VTI anisotropic corrections.

3.3.3 Radon de-multiple

Multiples and converted-waves are coherent periodic noise in the seismic data with move-out that may destructively or constructively interfere with the primary reflections of interest. The geologic structure and amplitude-versus-offset (AVO) characteristics may be affected by such types of unwanted coherent signal. Such wave phenomena are required to be removed, so as not to be detrimental to the primary reflection signal to image the geologic structure reliably. A high-resolution Radon algorithm is used for the removal of multiples, converted-waves, and any unwanted signal from the data. Radon utilizes the coherent signal from the data and transforms the data from the space-time domain to the τ-ρ domain. In such a domain, the dipping hyperbolic events, such as multiples, in space-time domain will be defined as a "point" with a high numbered p (move-out) in the τ-ρ domain (Russell et al., 1990). By modeling the primary energy in this domain, the parabolic events with move-out in a CDP gather can be muted, and only the values of p (move-out) that correspond to zero, or close to zero, are kept (Russell et al., 1990).

Either linear or parabolic moveout can be modeled with the Radon transform. When the linear method is selected, the high-resolution method is used throughout the transform domain. The generalized least-squares method is used to minimize the differences between the input data and the computed model data. The advantage of doing this is that the wavelet shape and amplitude of primaries and multiples are accurately obtained, and multiples can be removed by simple subtraction without the need for adaptive subtraction techniques. The limitation with conventional Radon is that some energy from some events can appear in the "wrong place" in the transform domain due to aliasing. Radon addresses this problem by predicting where the main events lie in the transform domain, emphasizing these areas and suppressing other regions. This emphasis and suppression are done via a set of weights that vary with move out.

Table 3.4: Parameters (right) and polygon mute (left) in τ-ρ domain for Radon de-multiple

Polygon Mute in tau-p Domain		**Radon De-multiple Parameters**	
Time (ms)	Mute in p (ms)	Parameter	Value
0	800	Reference offset (ft)	5
300	300	Minimum RNMO (ms)	5
600	200	Maximum RNMO (ms)	20
1,000	100	RNMO increment (ms)	6
2,000	60	p taper (ms)	40
4,000	50	Minimum Fold	50

Table 3.4 shows the parameters used for the calculation of the tau-p transform and the polygon mute applied for the removal of multiple events. The reference offset for the estimate of the move-out in milliseconds is 19,800 ft (6,035 m) while the minimum and maximum RNMO are -300 ms and 650 ms, respectively. The τ-ρ transform works in the frequency range of 7 – 100 Hz and only on CDP gathers with a minimum of eight traces for accurate modeling of multiple events. The p (move-out) ramp is chosen to be of 80 ms. The polygon mute is designed to mute most of the multiple near the target area at 2,000

ms with a mute value of 60 ms while allowing more energy to pass in the shallow area as it is not affected by multiples as much.

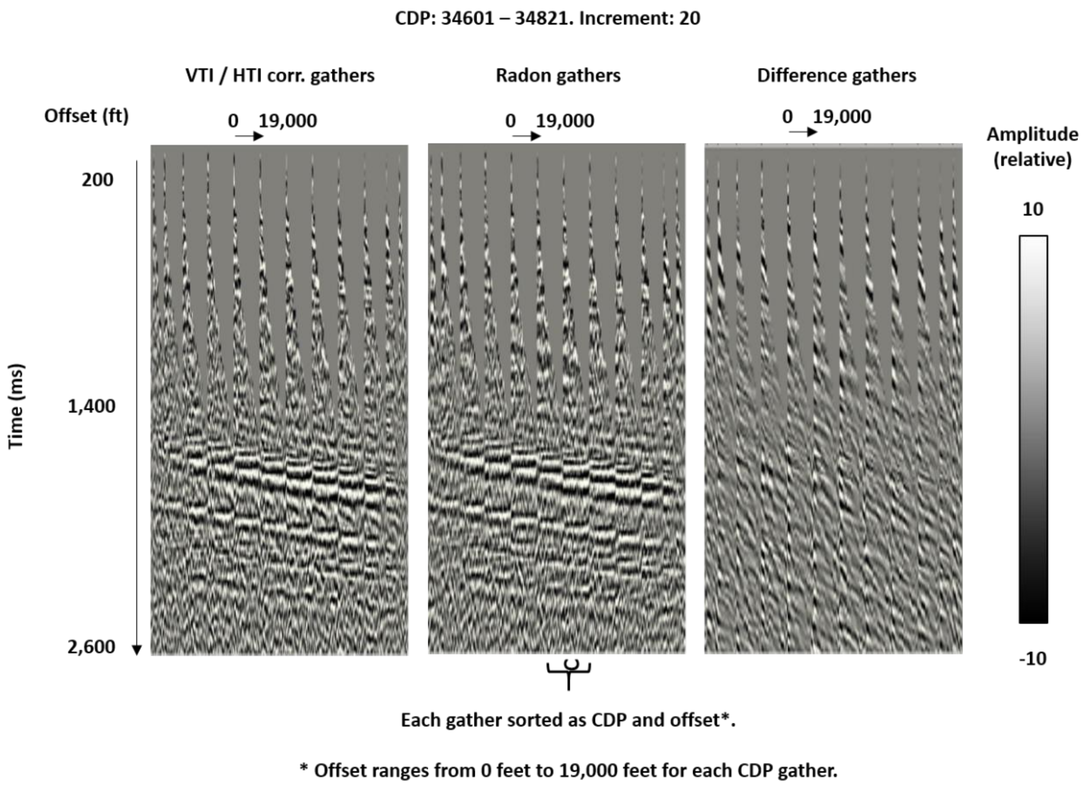

Figure 3.10: CDP gathers display for Radon de-multiple before (left), after (middle), and difference (right). Offset ranges from 0 – 19,000 ft for each CDP gather.

Figure 3.10 shows CDP gathers before, after, and the difference from the application of Radon de-multiple. The primary reflection events should be unaltered after the application of the algorithm and only coherent energy with a move-out should be removed from the CDP gathers.

3.3.4 CDP domain noise attenuation

Remnant linear coherent and incoherent noise may still be present in the data, which may have to be removed for the imaging of the subsurface. Linear noise attenuation and a τ-ρ domain noise attenuation method are used on CDP gathers for removal of such coherent and incoherent noise.

The linear noise present in the data is removed utilizing a frequency-wavenumber (*f-k*) filter by transforming the data into the *f-k* domain and applying a mute to the data not corresponding to primary flat reflections. This module attenuates events with slopes (up and down) smaller than the corresponding slope of the specified input velocity. The process works by transforming an ensemble of seismic shot data from the time-space domain to spatial frequency domain. Each frequency is convolved with a select weighting function, which is formed from the array of the signals with the desired frequency band. Velocities up to 12,000 ft/s (3,658 m/s) are attenuated by developing a filter in the *f-k* domain to remove such data with the corresponding velocity.

A technique is used utilizing the Radon transform for removal of incoherent and random energy in the CDP gather. The primary events are modeled in the τ-ρ domain using a high-resolution Radon transform (refer to section 3.3.3). The primary-only model is output from the algorithm and scaled down to 66.667%, while the input dataset is scaled down to 33.333% and the result is obtained by addition of both the input and primary-only model. This method ensures that energy that is not from the primary events are attenuated greatly.

Table 3.5: Parameters for the *f-k* filter (right) and the Radon de-noise polygon mute (left)

Polygon mute in tau-p domain

Time (ms)	Mute in p (ms)
0	-600
300	-500
600	-400
1,000	-350
2,000	-300
4,000	-250

Linear noise attenuation parameters

Parameter	Value
CDP distance (ft)	110
Maximum velocity (ft/s)	12,500
Maximum frequency (Hz)	5
Minimum frequency (Hz)	40

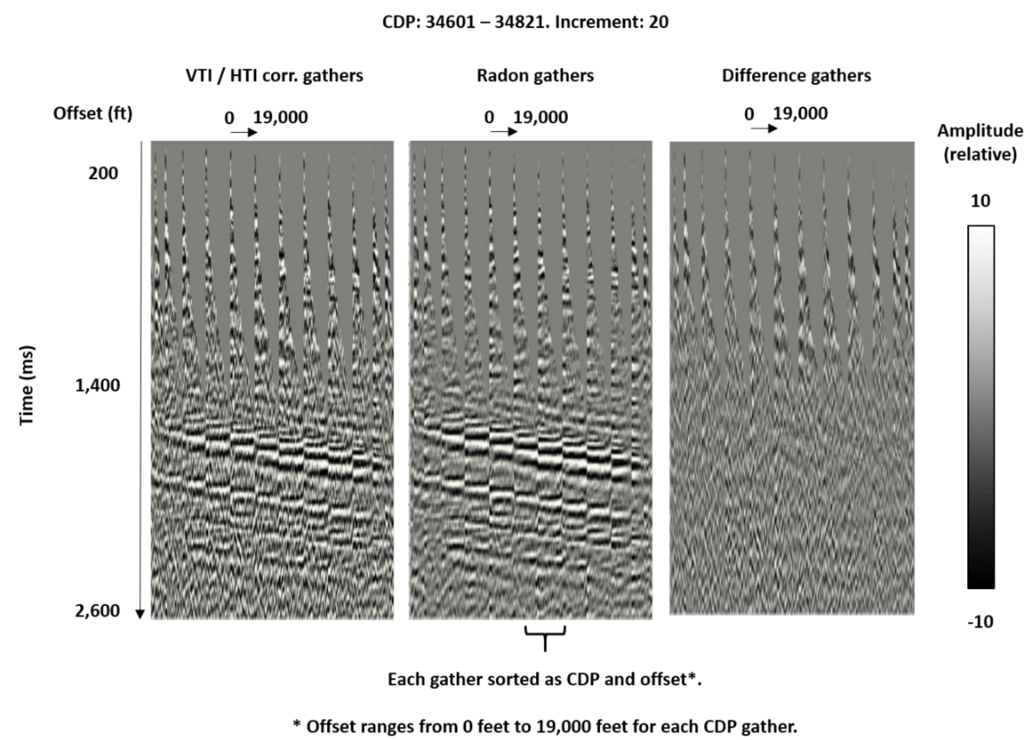

Figure 3.11: CDP gathers display for CDP domain noise attenuation before (left), after (middle), and difference (right). Offset ranges from 0 – 19,000 ft for each CDP gather.

Table 3.5 shows the parameters used for the Radon denoise and *f-k* filter. The τ-ρ polygon mute is opposite and milder than the one applied previously for the de-multiple, as its primary purpose is removing any random remnant noise. Similarly, the *f-k* filter's maximum velocity to attenuate is 12,500 ft/s (3,810 m/s) for data within a range from 5 – 40 Hz. Figure 3.11 shows the before, after, and the difference for the CDP domain noise attenuation workflow. To compare the improvement from the post-migration seismic conditioning on the stack section, Figure 3.12 shows the raw input stack after migration and the final conditioned stack. From the post-migration processing, it is evident the conditioned stack is a better representation of the geologic structure by improving the signal-to-noise value, eliminating multiples and converted-wave, removing random and incoherent noise, and focusing on reflection events.

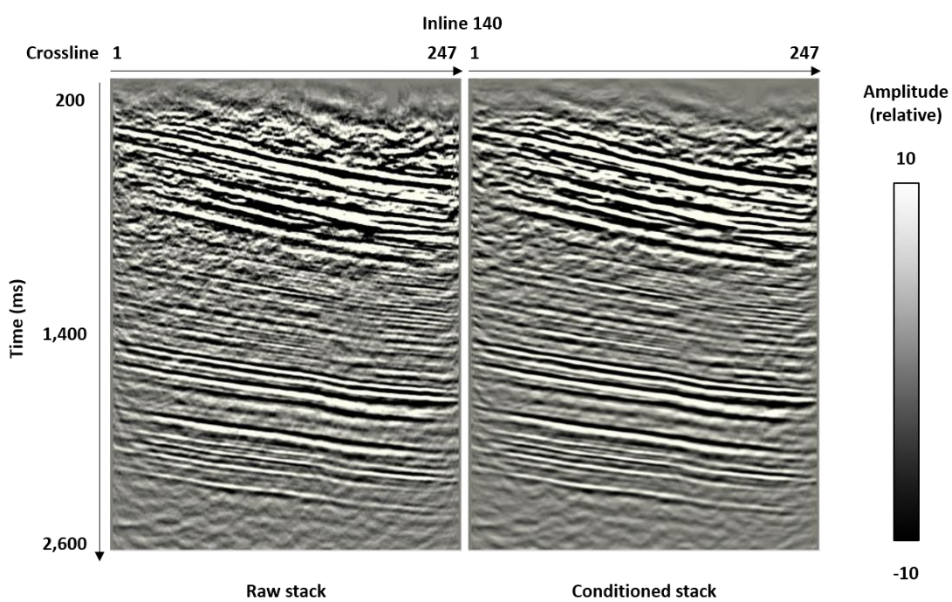

Figure 3.12: Full stack section before (left) and after (right) post-migration seismic conditioning.

Chapter 4

AVO simultaneous inversion

IFP's (Institut Francais du Petrole) pre-stack AVO simultaneous three-term inversion algorithm is a Bayesian non-linear data fitting method with an objective of extracting accurate information of the subsurface elastic and petrophysical properties from the seismic data. A prediction of properties can be calculated by solving the Aki-Richards AVO equation using an initial model of the subsurface along with the seismic data. In an iterative process, the model is updated to minimize the error or misfit of the predicted data from a background model and observed data (seismic). Various iterations are completed until the misfit is reduced sufficiently. During inversion, geological knowledge, pre-stack seismic amplitude, and well-log information are combined to build optimal elastic parameter distributions, which is consistent with all input data. IFP Pre-stack inversion is based on a Bayesian formalism, in which the seismic noise and the elastic model uncertainties are assumed to be described by Gaussian probabilities having zero mean, with a covariance operator in the data space and the model space. The algorithm has been developed by IFP and integrated into Paradigm Geophysical Software.

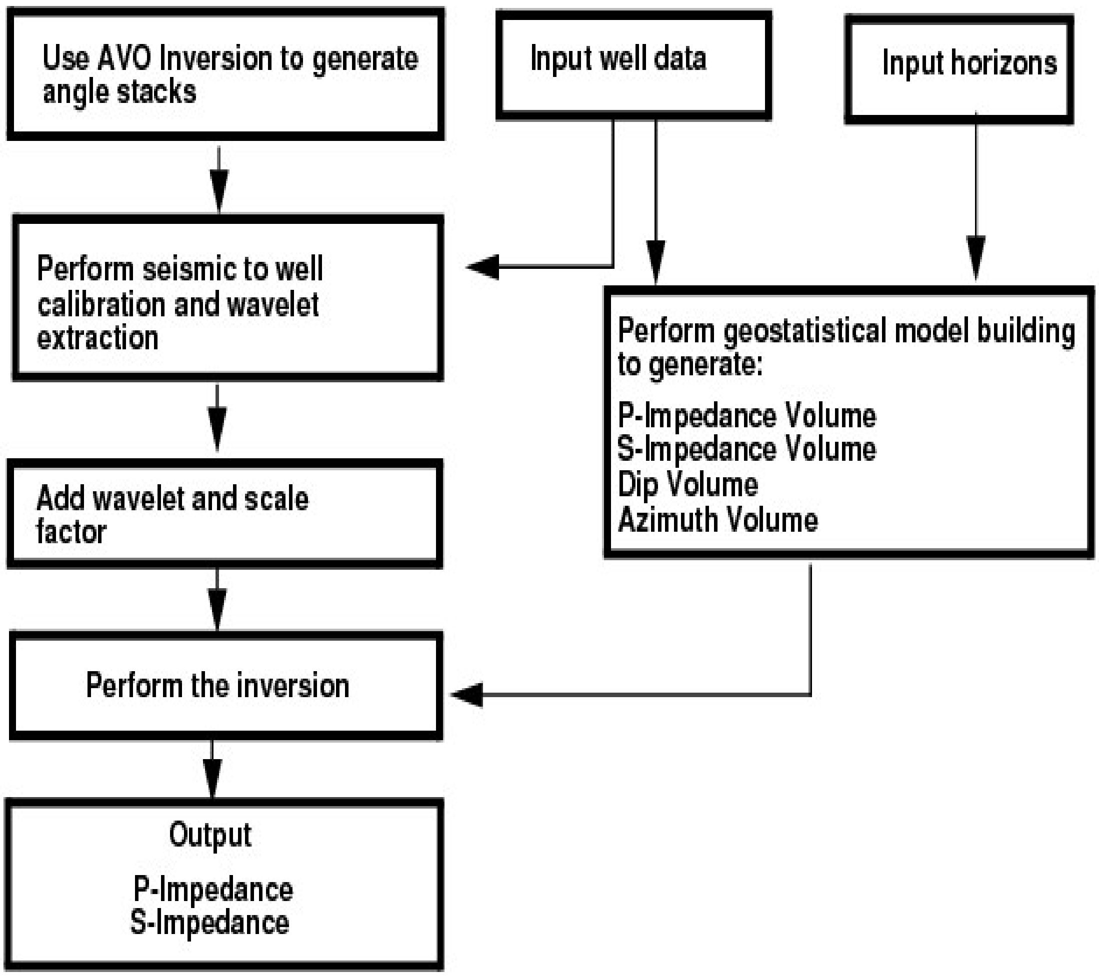

Figure 4.1: Schematic diagram defining the methodology for IFP's pre-stack AVO simultaneous inversion.

4.1 Seismic – well correlation

4.1.1 Convolutional model

Rock physics relationships derived at the well location can be used in conjunction with seismic data to obtain physical properties throughout the seismic survey. To be able to acquire petrophysical information from seismic, a correlation from the well to the seismic data is made. The well data can be related to the seismic data at the well location by a convolutional model, where V_P and density are used to compute a P impedance log and subsequently to calculate a reflectivity time series. The reflectivity at each interface is derived by dividing the change in impedance by twice its average (Russell, 2012). The convolutional model states that a reflectivity series convolved with a wavelet yields a seismic a trace. Figure 4.2 displays a schematic diagram showing how a synthetic seismogram is obtained.

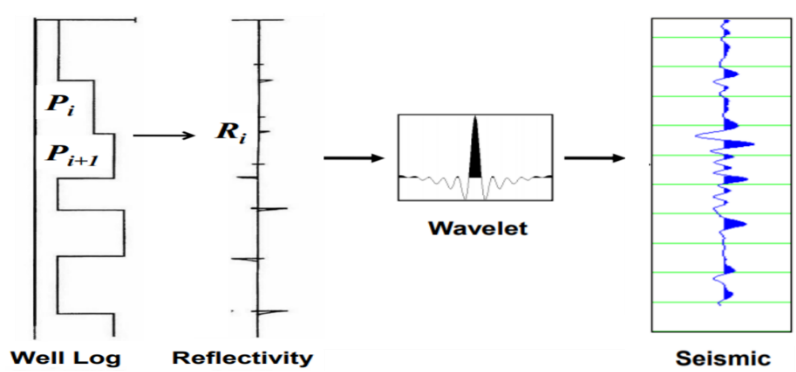

Figure 4.2: Schematic representation of a synthetic seismogram generated using the convolutional model (modified from Russell, 2010).

4.1.2 Wavelet and synthetic seismogram

A wavelet is required to convolve with the reflectivity series from the well to obtain a seismic trace corresponding to the rock properties from the well. A wavelet is generated by obtaining the frequency content near the target area, from 1.5 – 2.3 seconds, and extracting a wavelet using a least-square minimization method. The algorithm uses a least-squares method to minimize the error from the fit from the synthetic and seismic trace to obtain the phase of the wavelet accurately. Once a phase and amplitude spectrum are obtained for a wavelet, stretch-and-squeeze methods are utilized to correct for errors due to the difference of seismic and well properties, such as velocity dispersion and interference from multiples and converted-waves. Figure 4.3 displays an approximate wavelet -55 degrees in phase and a frequency bandwidth of 10 – 40 Hz. A seismic-to-well tie is displayed in Figure 4.4. The cross-correlation is between the synthetic and seismic trace and is approximately 80% within the target interval.

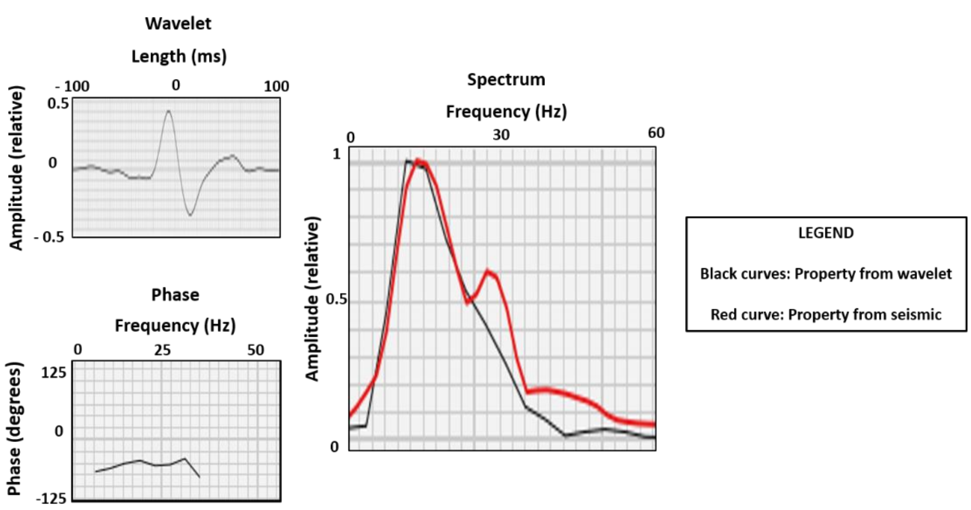

Figure 4.3: Wavelet, spectrum, phase, and cross-correlation extracted at RSU-#1 well location.

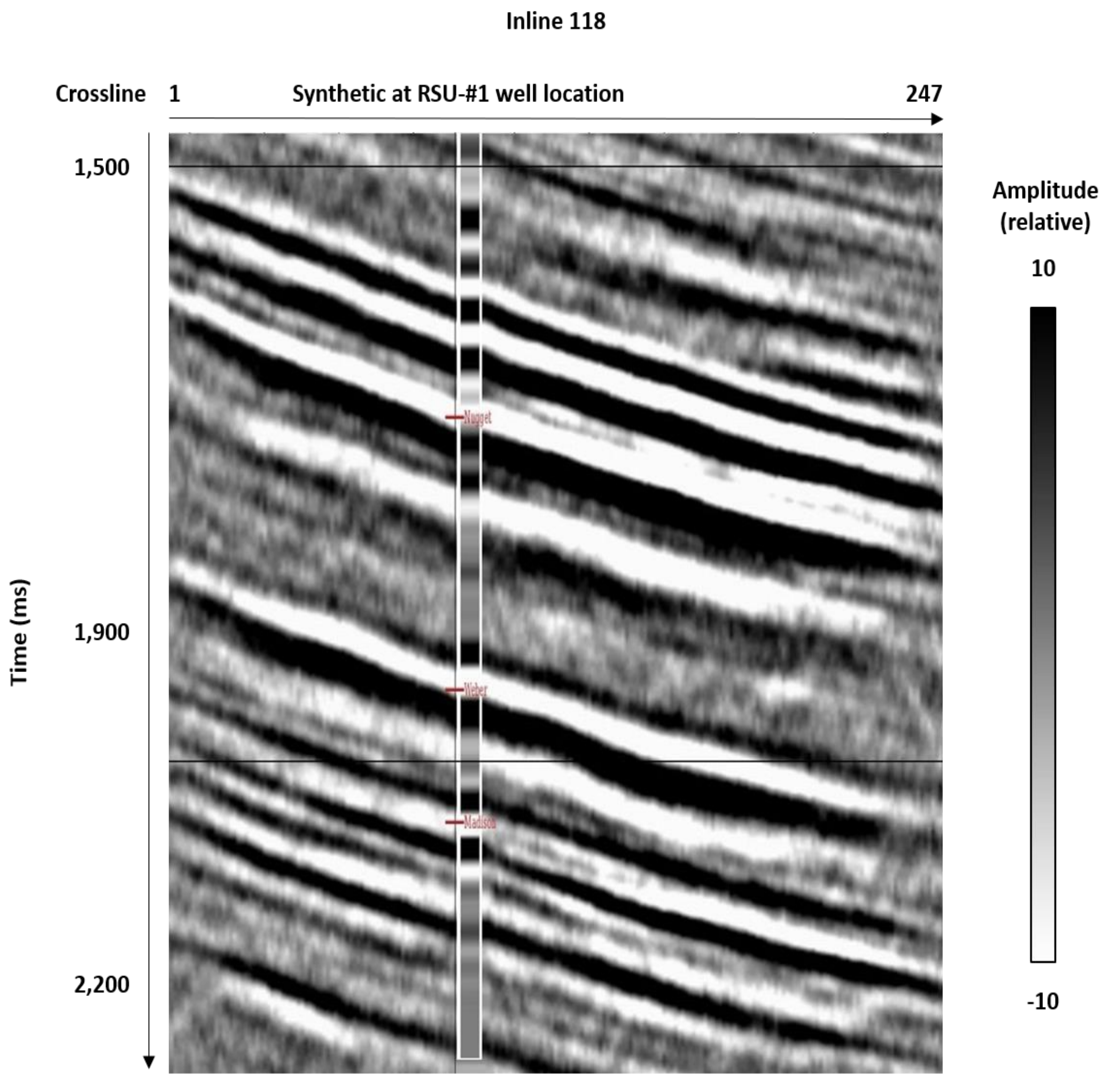

Figure 4.4: Seismic-to-well correlation at RSU-#1 well location. Synthetic generated from the well is overlain to compare to the seismic section amplitudes.

4.2 Angle stack generation

4.2.1 Angle rage analysis

The Aki-Richards AVO equations relate the incidence angle of the wave propagation to reflection amplitude in terms of V_p, V_s, and density. Pre-stack simultaneous AVO inversion utilizes information from the seismic data within various incident angle ranges to obtain a solution to the AVO equation and obtain the elastic properties of interest (P impedance, S impedance, and density). The pre-stack seismic data is analyzed for incident angle information to generate angle stacks which are input for the AVO inversion. Ray-tracing techniques are used for calculating the path of waves propagating through the subsurface that have different propagation velocities, absorption characteristics, and reflecting surfaces to calculate incident angle information from CDP gathers (Rawlinson et al., 2007).

Figure 4.5 displays an overlay of angle ranges with the CDP gathers for angle range analysis. The seismic data is analyzed for each angle range to determine the angle stacks that display similar signal-to-noise values, coherent amplitude energy, and attenuation absorption characteristics. Angle ranges utilized for the generation of angle stacks are 00 – 13 degrees, 08 – 22 degrees, 18 – 32 degrees, and 28 – 42 degrees. Angle range overlap is desired to maximize the amount of angle information per each angle range. Such angle ranges display information from the near, middle, and far angles from the seismic data that are used for the derivation of P impedance, S impedance, and density.

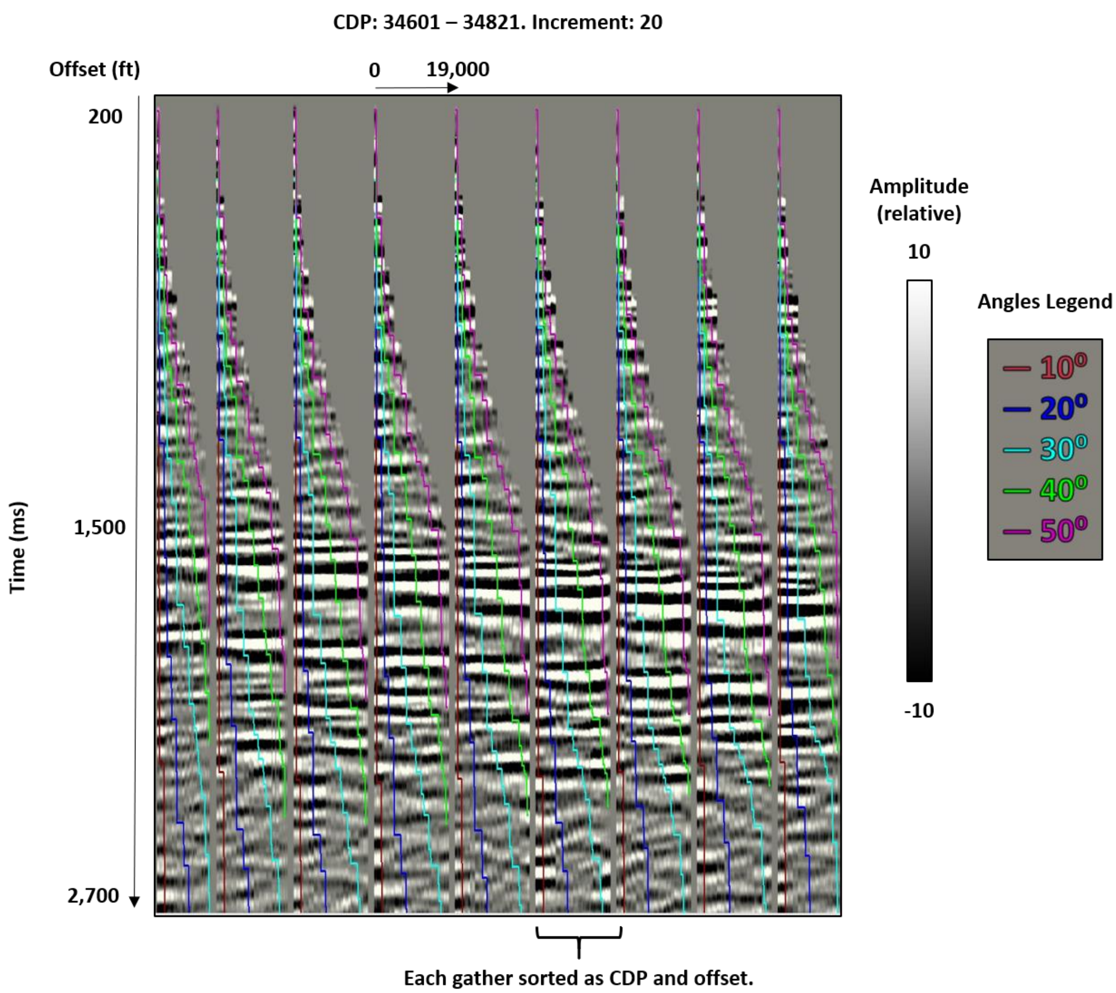

Figure 4.5: Angle range analysis on CDP gathers. Ray-traced incident angles are overlain on the CDP gathers.

4.2.2 Angle stacks

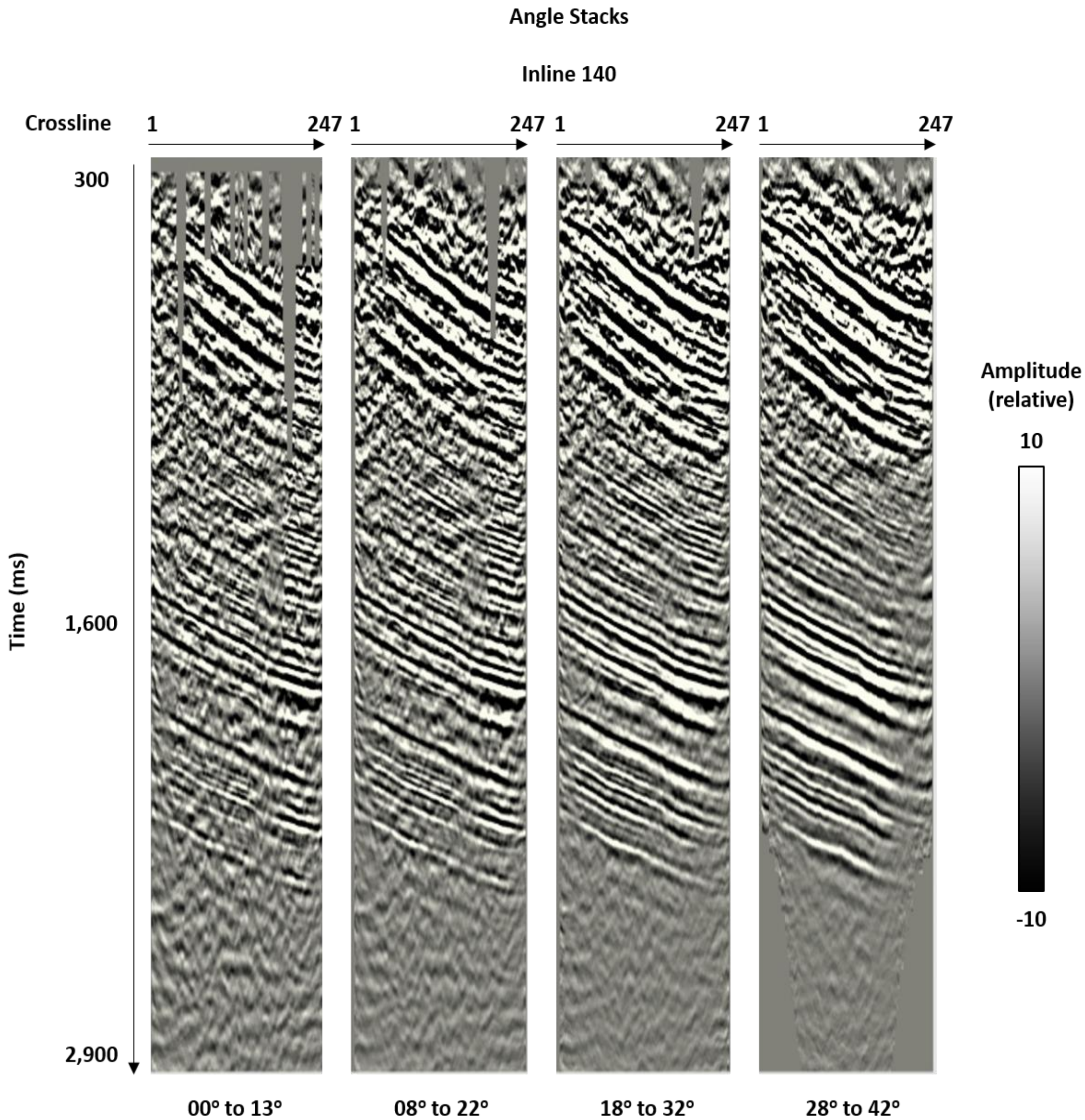

Figure 4.6: Angle stacks generated from the gathers using a ray-tracing technique. Angle ranges are displayed for each angle stack.

4.3 Wavelets

4.3.1 Wavelet extraction

Roy-white wavelet extraction method is used, and it estimates the wavelet by correlating the well-log and seismic data and minimizing the error using least-squares techniques to determine the phase and frequency spectrum (White and Simm, 2003). Wavelets are estimated for each of the angle stacks utilizing the RSU-#1 well. Each wavelet characterizes the phase and frequency spectrum for each specific angle range, thus determining the response for P impedance, S impedance, and density. The angle stack is rotated to SEGY American standard polarity by a phase rotation of 55 degrees and is used for the estimation of a zero-phase wavelet for each angle stack. Along with the wavelets, a wavelet scalar must be obtained that relates the amplitude of the wavelet to the amplitude of the seismic data.

The wavelets extracted are expected to be characterized by similar wavelet characteristics such as frequency spectrum and phase to obtain a coherent inversion response throughout all incident angles. The phase obtained for the wavelets vary from -10 to 10 degrees with the main phase component close to zero phase. The frequency bandwidth for each of the wavelets is similar in the range of 10 – 50 Hz. The scalars obtained that relate the amplitude of the wavelet to the amplitude of the seismic data are 5.1e-05, 4.3e-05, 2.9e-05, and 2.2e-05, for angles 00 - 13, 08 -22, 18 – 32, and 28 – 42 degrees, respectively

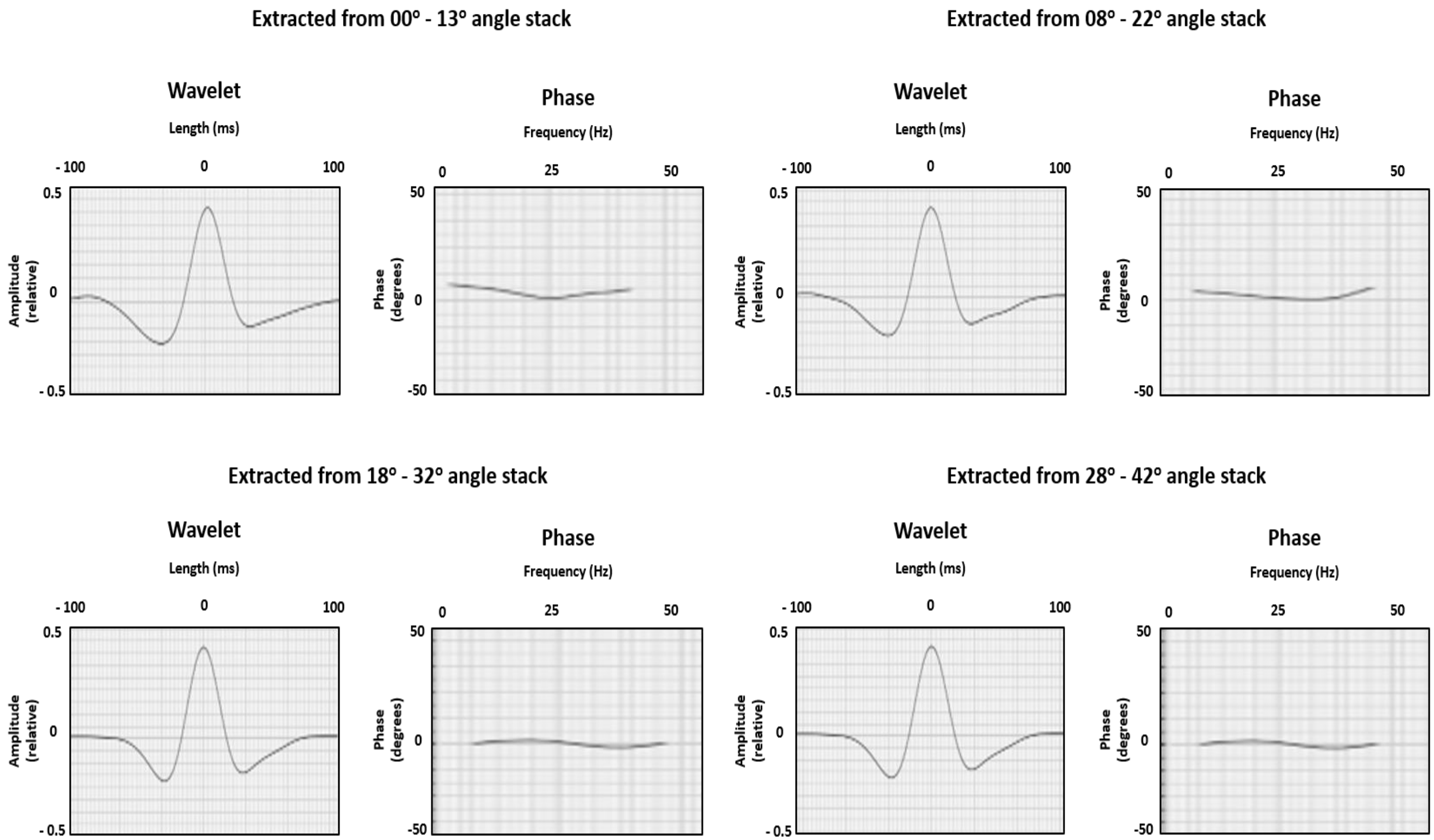

Figure 4.7: Wavelets and phase extracted from the angle stacks. The phase is roughly zero phase for all angle stacks.

4.4 Low-frequency background model generation

4.4.1 Collocated cokriging of well-logs

Kriging and cokriging are geostatistical techniques used for interpolation (mapping and contouring) purposes. Both methods are generalized forms of univariate and multivariate linear regression models, for estimation at a point, over an area, or within a volume (Chambers et al., 2000). They are linear-weighted averaging methods, similar to other interpolation methods; however, their weights depend not only on distance but also on the direction and orientation of the neighboring data to the unsampled location (Chambers et al., 2000).

Traditional regression methods only use data available at the target location and fail to use existing spatial correlations from secondary-data control points and the primary attribute to be estimated. Cokriging methods are used to take advantage of the covariance between two or more regionalized variables that are related and are appropriate when the primary attribute of interest (well data) is sparse, but related secondary information (seismic) is abundant. Geostatistical-data-integration methods yield more-reliable reservoir models because they capitalize on the strengths of both data types (Journel, 1989).

4.4.2 Low-frequency background models

Collocated cokriging method is used for the extrapolation of petrophysical properties from the well throughout the survey area guided by seismic horizons and background P impedance, S impedance, and density models. Such models obtain the high frequencies from the well-logs and must be filtered to the missing frequencies from the seismic data for the pre-stack AVO inversion. The co-kriged extrapolated models are high cut filtered by 0 – 0 – 6 – 12 Hz, which correspond to the low frequencies missing from the seismic data. Such low frequencies, along with the higher frequencies from the seismic data generate a more accurate inversion result. Figure 4.8 displays the P impedance, S impedance, and density filtered background models.

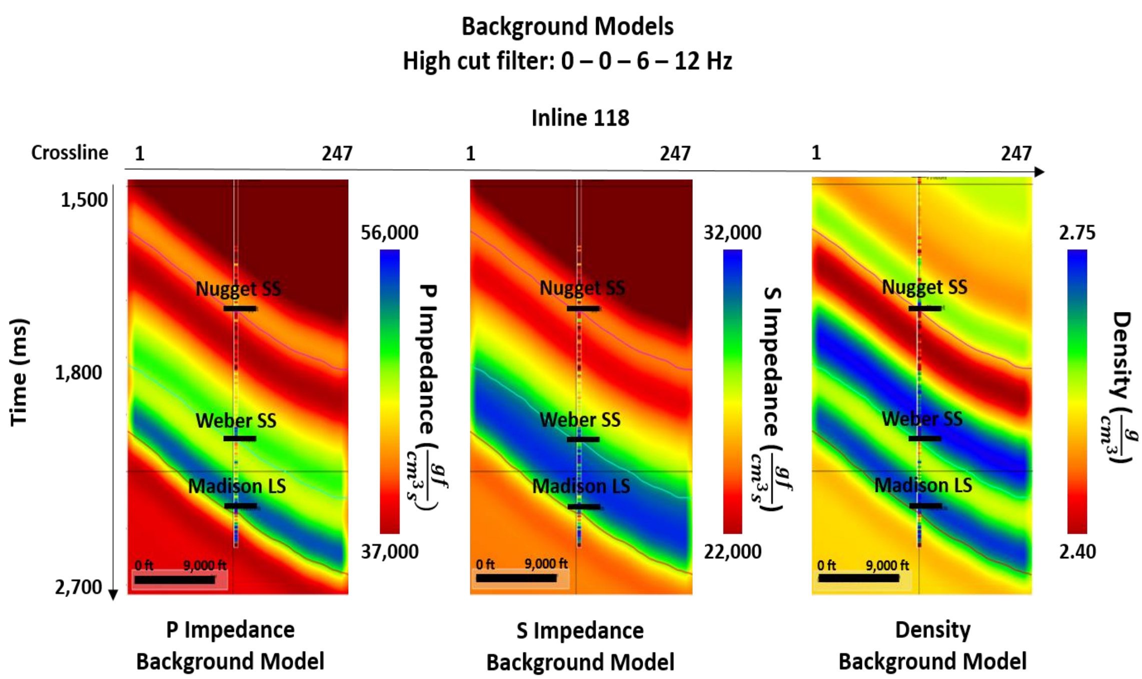

Figure 4.8: P impedance (left), S impedance (middle), and density (right) high-cut filtered background models.

4.5 AVO Inversion

4.5.1 AVO inversion background

IFP Pre-stack Constrained Stratigraphic Inversion performs simultaneous inversion of multiple angle stacks to provide P and S impedance volumes and optional density data. Required for the inversion are two or more angle stacks, a wavelet for each angle stack, a micro-layer geometry in the form of dip and azimuth volumes, confidence information for both the seismic data and the background model, a low-frequency background model, and optional formation volumes. The output from the inversion is P impedance, S impedance, and density. The inversion can also be used as a standard AI inversion using one seismic attribute. The IFP Pre-stack Constrained Stratigraphic Inversion application performs inversion simultaneously for all elastic parameters. The inversion is a Global 3D and model-based Aki-Richards modeling for consistent estimates of both P and S impedances.

During the inversion, geological knowledge, pre-stack seismic amplitudes, and well-log information are combined to build optimal elastic parameter distributions, which are consistent with all input data.

4.5.2 Parameters

The pre-stack AVO simultaneous inversion requires for parametrization of distinct variables such as low-frequency background models, noise level content, standard deviation from background models, geologic dip and azimuth orientations, wavelets, and wavelet scalars. Optimization of parameters is of utmost importance for obtaining the best possible results that yield petrophysical parameters that are used for interpretation. Noise level variations from near, middle, and far angles stacks defined the seismic information allowed in the inversion. The lower the percentage of noise level, more information from the seismic data is input in the inversion; thus, more noise is added as well. The noise level chosen is 5% for each of the angle stacks in the near, middle, and far angles. Standard deviation parameter defines how much the values can deviate from the input background model. After testing, the values chosen are 4,000 $\frac{gf}{cm^3 s}$ for P impedance, 3,000 $\frac{gf}{cm^3 s}$ for S impedance, and 0.15 $\frac{g}{cm^3}$ for density.

Table 4.1: Parameter list for the generation of the low-frequency background models and AVO inversion volumes

Parameter	Value	Parameter	Value
Extrapolation method	Co-kriging	Noise level (%)	5 through all angle stacks
Extrapolation data	RSU-#1 well logs	P impedance stdev. (gf/ccs)	4,000
Co-kriging model	Seismic int. velocity field	S impedance stdev. (gf/ccs)	3,000
High-cut filter (Hz)	0-0-6-12	Density stdev. (g/cc)	0.15

4.5.2 AVO inversion volumes

The outputs from the AVO inversion algorithm are P impedance, S impedance, and density volumes. Figure 4.9 displays the volumes obtained from the AVO inversion with a synthetic overlain respectively. For the P impedance volume, the values range from 25,000 $\frac{gf}{cm^3 s}$ and 60,000 $\frac{gf}{cm^3 s}$, for S impedance the values range from 12,000 $\frac{gf}{cm^3 s}$ and 35,000 $\frac{gf}{cm^3 s}$, and for the density volumes the values range from 2.3 $\frac{g}{cm^3}$ and 2.85 $\frac{g}{cm^3}$. The synthetic overlain with the inversion volumes display high correlation indicating the inversion converged to a reliable result. Such inversion volumes are used for the generation of additional elastic properties, and in conjunction with rock physics relationships, a reliable study for carbon dioxide sequestration is made.

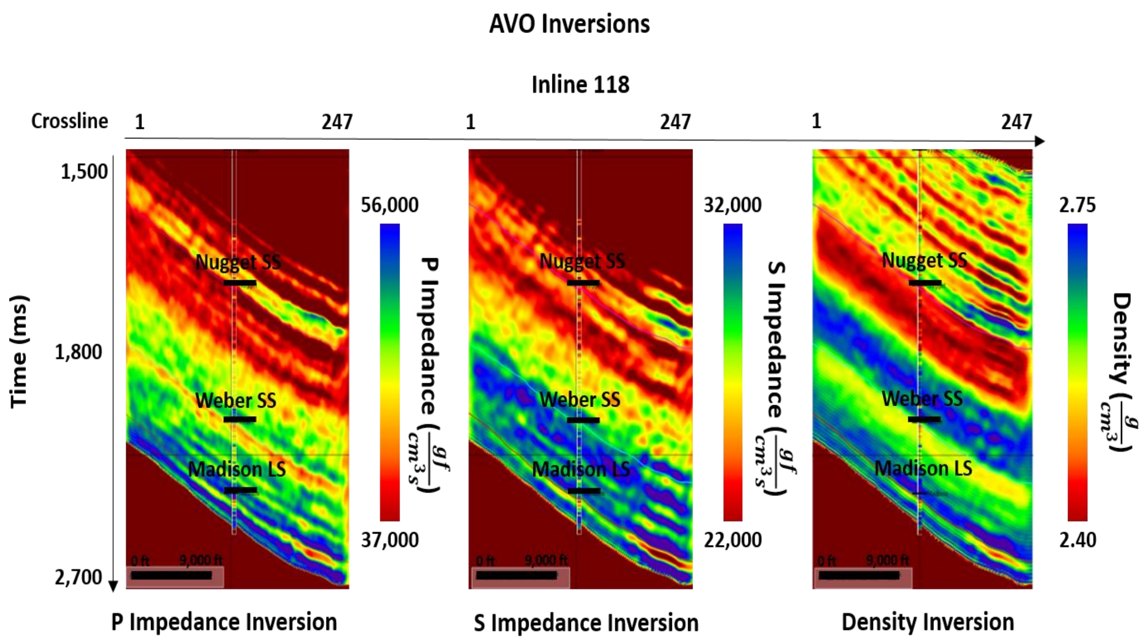

Figure 4.9: P impedance, S impedance, and density inversion results at inline 118 with log values overlay.

4.5.3 Inversion QC

Various quality-control methods are used for the verification and validity of the AVO inversion prior to interpretation. Figure 4.10 displays cross-plots from the log values at the well (x-axis) and the inversion results at the well location (y-axis). The values should fall within a 45-degree line from axis-origin to demonstrate high values of correlation. The cross-plot analysis shows values of correlation of 86.7%, 88.8%, and 71.0% for P impedance, S impedance, and density, respectively. An additional method for validating the inversion results is to overlay the well-log, the background model, and the inversion extracted at the well for P impedance, S impedance, and density, such as the display in Figure 4.11.

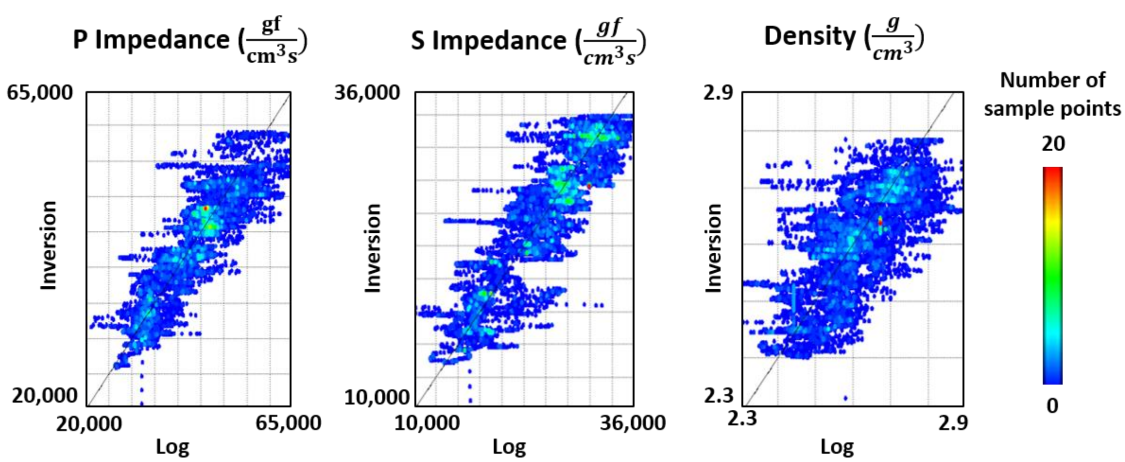

Figure 4.10: P impedance, S impedance, and density inversion QC cross-plots. The x-axis corresponds to the well-log and y-axis to the inversion extracted at RSU-#1 well location. The color bar represents the number of sample points in the cross-plot.

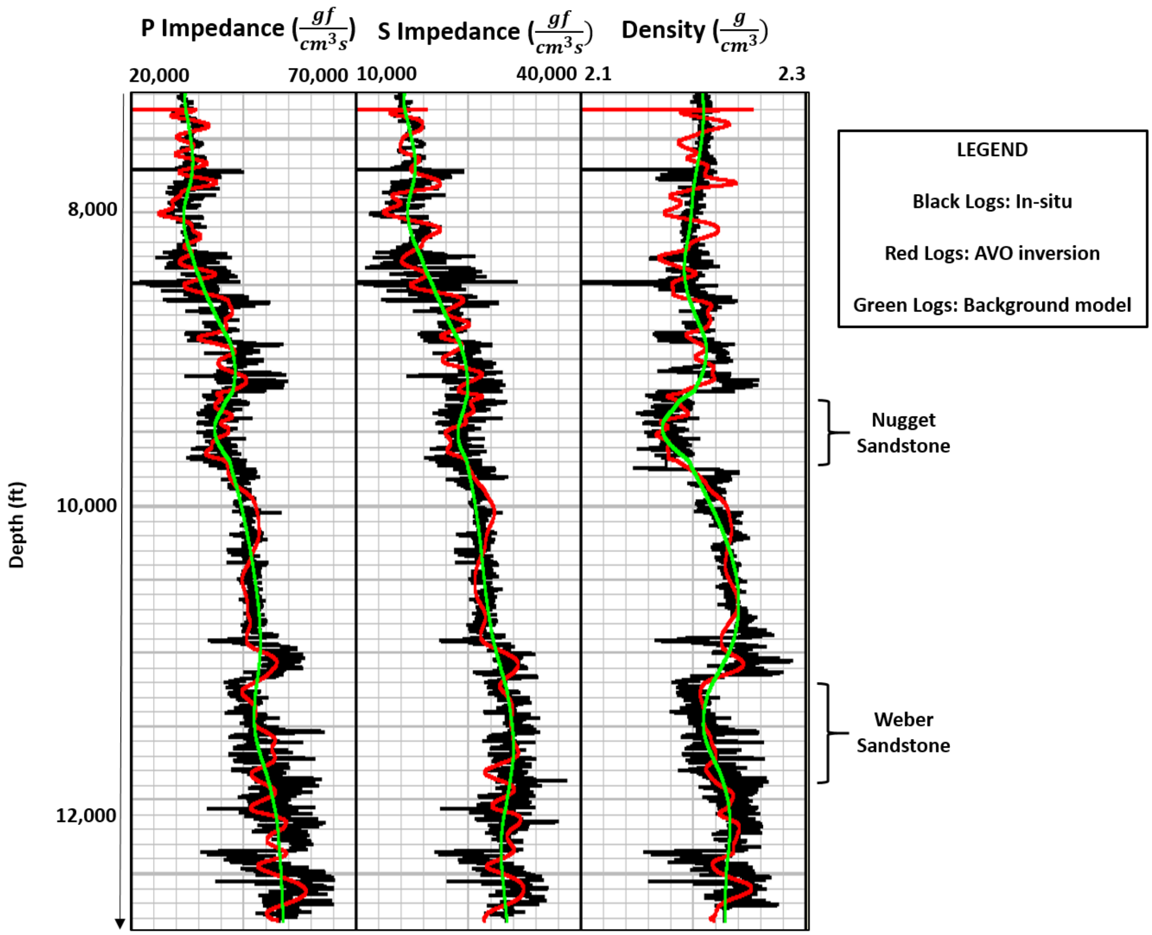

Figure 4.11: P impedance, S impedance, and density logs (black), background models (green), and inversion (red) overlay extracted at RSU-#1 well location for QC.

Chapter 5

PS reflections seismic processing and inversion

Although the industry standard is to analyze the vertical component (PP reflection) data, converted-wave reflections (PS mode conversion) can be used to help determine additional information such as density with higher reliability due to the sensitive variations of the S-waves to density compared to the P-waves. Processing of the horizontal component dataset requires having prior information regarding the static solution and velocity model of the P-wave data. The PS processing sequence includes steps for analysis of PP reflection data but involves some additional steps such as component rotation, Asymmetrical Conversion Point (ACP) binning, $\frac{V_p}{V_s}$ analysis, shear-wave splitting analysis and rotation, and PP – PS event registration. The PS image is used to generate the post-stack inversion to obtain a volume of S impedance, that is more accurate than the one derived from the PP AVO inversion.

5.1 PS seismic processing

5.1.1 Processing workflow

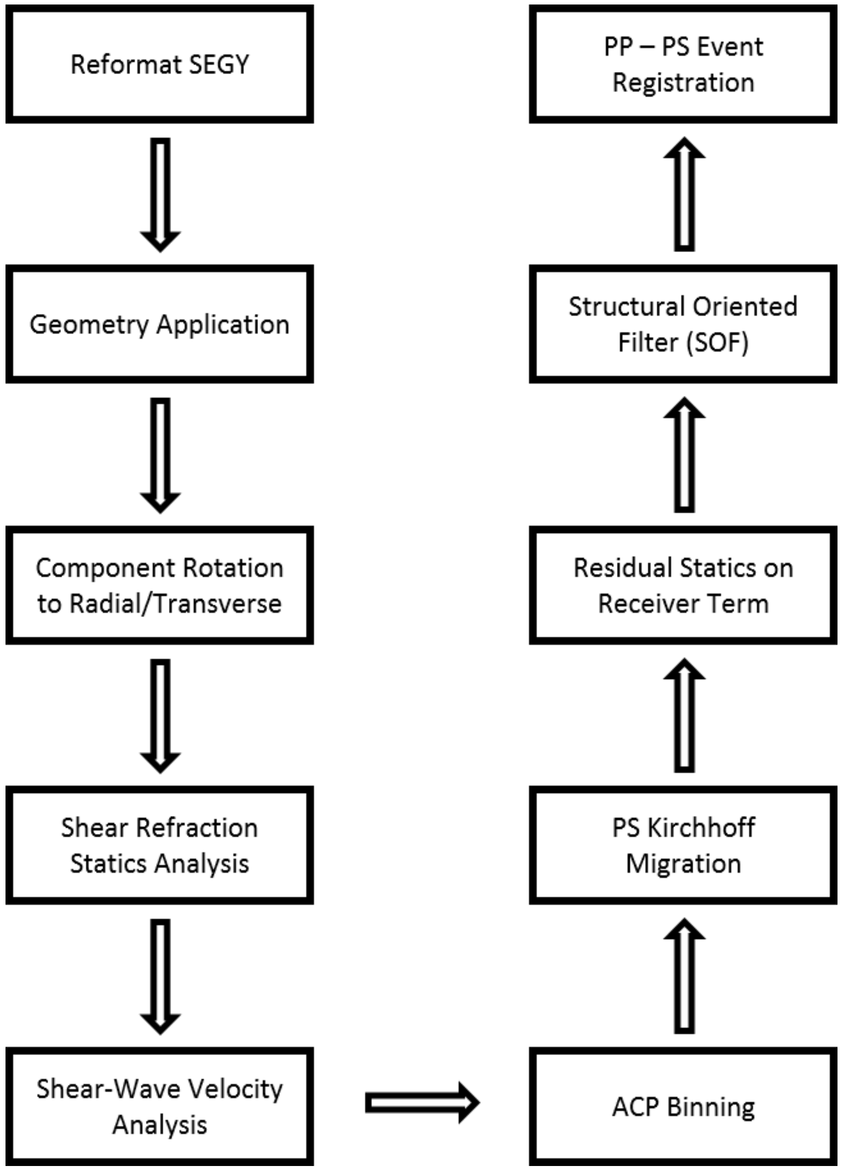

Figure 5.1: Representation of the PS processing workflow.

5.2 Statics

5.2.1 Shear statics determination methods

Accurate velocities and statics solution are crucial for obtaining a reliable image of the subsurface. To derive the S-wave velocity model, the velocities derived from vertical component processing are used, and a rough scalar is applied; usually obtained from the $\frac{V_p}{V_s}$ log obtained at the well location. Such a velocity volume will be a starting point for the velocity analysis for the radial and transverse components. For the analysis of the shear-wave statics one of the following three methods can be used:

1. Refraction statics generated from picking shear-wave refractions predominantly observed on the radial component.

2. Refraction statics from PP reflection processing with the application of a scalar to the receiver term. This is due to the difference of the travel-times of the up-going wave.

3. Receiver stack of PP reflections and PS reflections, then observe near-surface reflections and calculate the static shifts required to apply to the PS reflections to obtain a coherent and continuous reflection.

A method proposed to determine the shear-wave statics is to calculate a scalar that can be multiplied to the PP receiver refraction statics and used such statics along with the PP shot refraction statics. Typically, this scalar ranges between 1.5 to 5 and is related to the $\frac{V_p}{V_s}$ ratio in the near-surface and is determined by trial-and-error to align converted-wave reflection events in the stack. Figure 5.2 displays a map for the survey of P-wave shot refraction and receiver refraction statics. The receiver refraction statics are multiplied by a value of 2 and applied to the data, but further work is required for more accurate shear-wave statics.

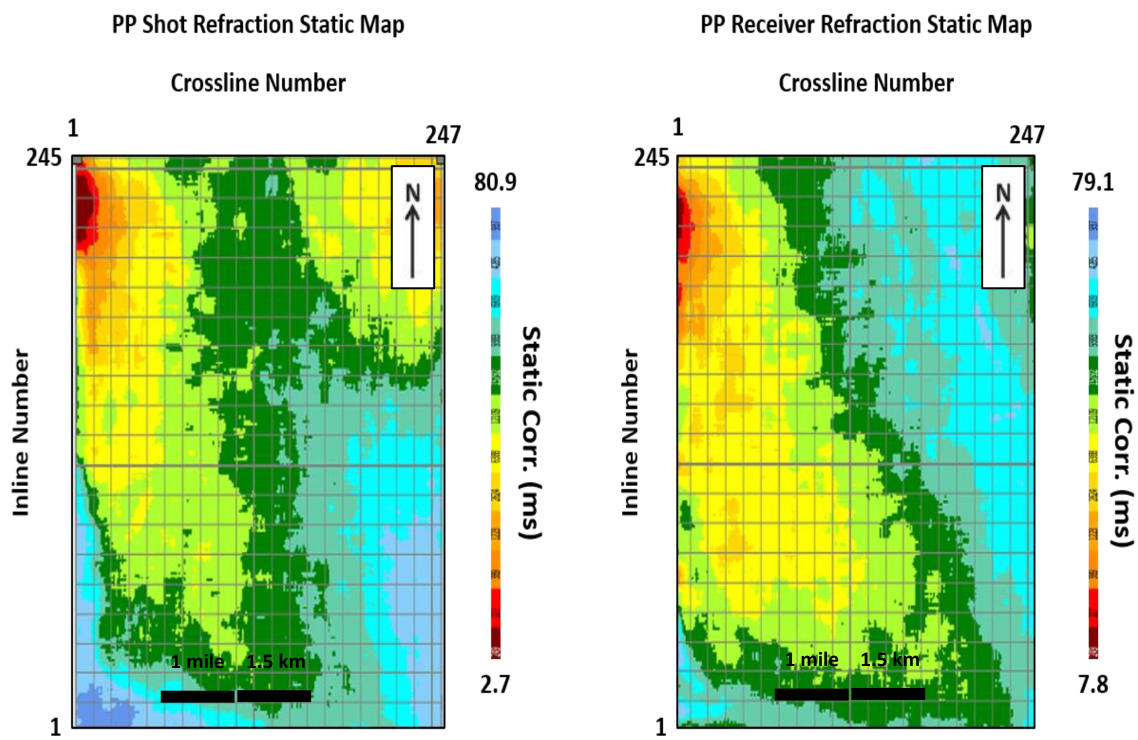

Figure 5.2: Shot (left) and receiver (right) refraction statics map determined from PP refraction events.

5.2.2 Shear-refraction picking

An additional method to determine shear statics to align converted-wave reflection events is to pick the shear-wave refraction from shot data from the radial component. This method utilizes pure shear-wave refractions to estimate the velocity and delay time in milliseconds of the near-surface for converted-waves. In such a method, the statics solution determined from the receiver term should be utilized, while the shot term discarded since only the shear-waves traveling up are of interest and are represented by the receiver term. The refractions of the shear-wave for this dataset has a slope equivalent to a velocity predominantly between 5,000 ft/s (1,524 m/s) to 6,000 ft/s (1,829 m/s) and can be visualized between 500 to 2500 milliseconds in time underneath the PP refractions. Figure 5.3 shows a shot gather displaying primary and shear-refractions with refraction picks in pink. The refraction is picked between 3,000 (914 m) to 8,000 ft (2438 m) because most shear-wave energy is found to be in this range.

Figure 5.4 shows a cross-section for north-south and east-west directions, displaying topography and velocity determined from statics solution in the near-surface. The values for the velocity of the shear-waves determined from the shear-waves statics picked range from 2,008 ft/s (612.0 m/s) to 2,430 ft/s (741 m/s). Considering the PP near-surface velocities in the range of 5,832 ft/s (1,778 m/s) and 6,428 ft/s (1,959 m/s), the $\frac{V_p}{V_s}$ determined for the survey in the near-surface ranges roughly between 2.4 and 3.3.

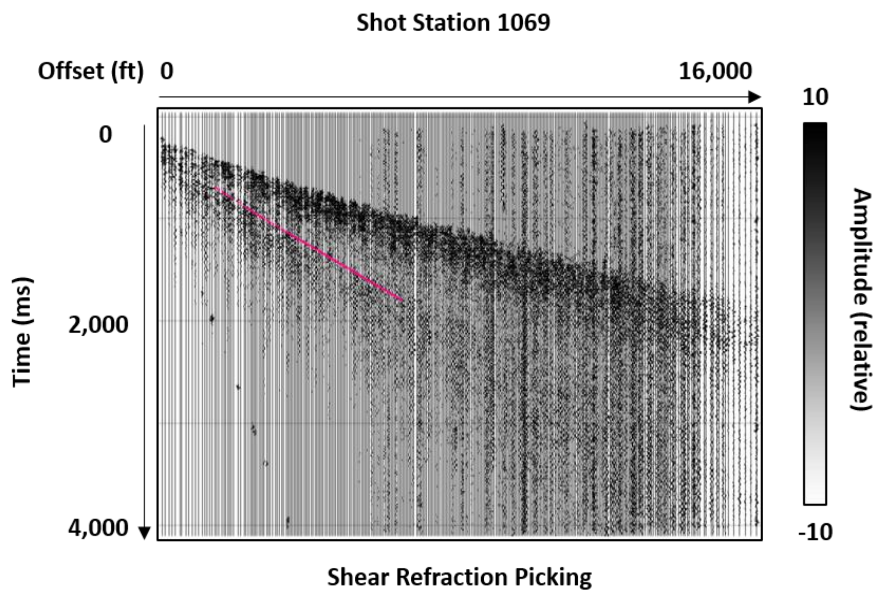

Figure 5.3: A shot gather with refraction statics picking. Manual picks (pink) done for an offset range of 3,000 ft (914.4 m) to 8,000 ft (2,438 m).

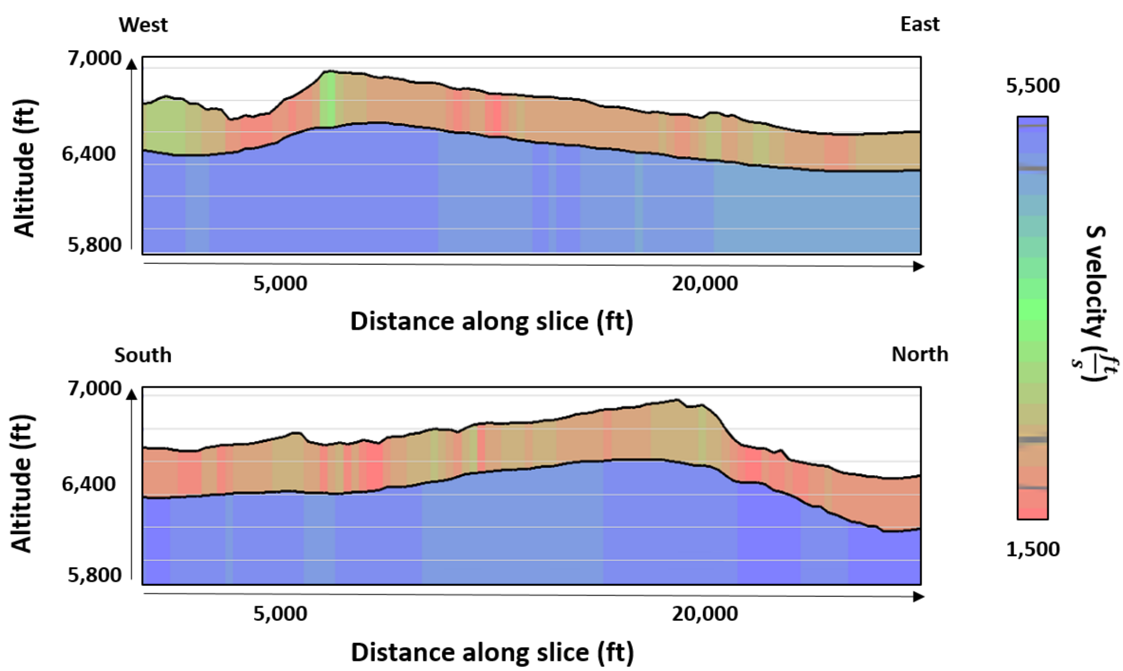

Figure 5.4: Cross-section for the north-south and east-west directions, displaying velocity values from refraction picks.

After picking the shear-wave refraction from the shot gathers in the survey, the algorithm utilizes the refraction times and velocities to determine the delay time in millisecond that is required to apply to the data to align the reflection events. Figure 5.5 displays a map of delay time calculated from the shear-wave refraction picks. The values of the delay times range from 74.8 ms and 162.6 ms. The receiver term from the statics solution is then applied to the data along with the PP shot refraction statics to align the converted-wave reflection events.

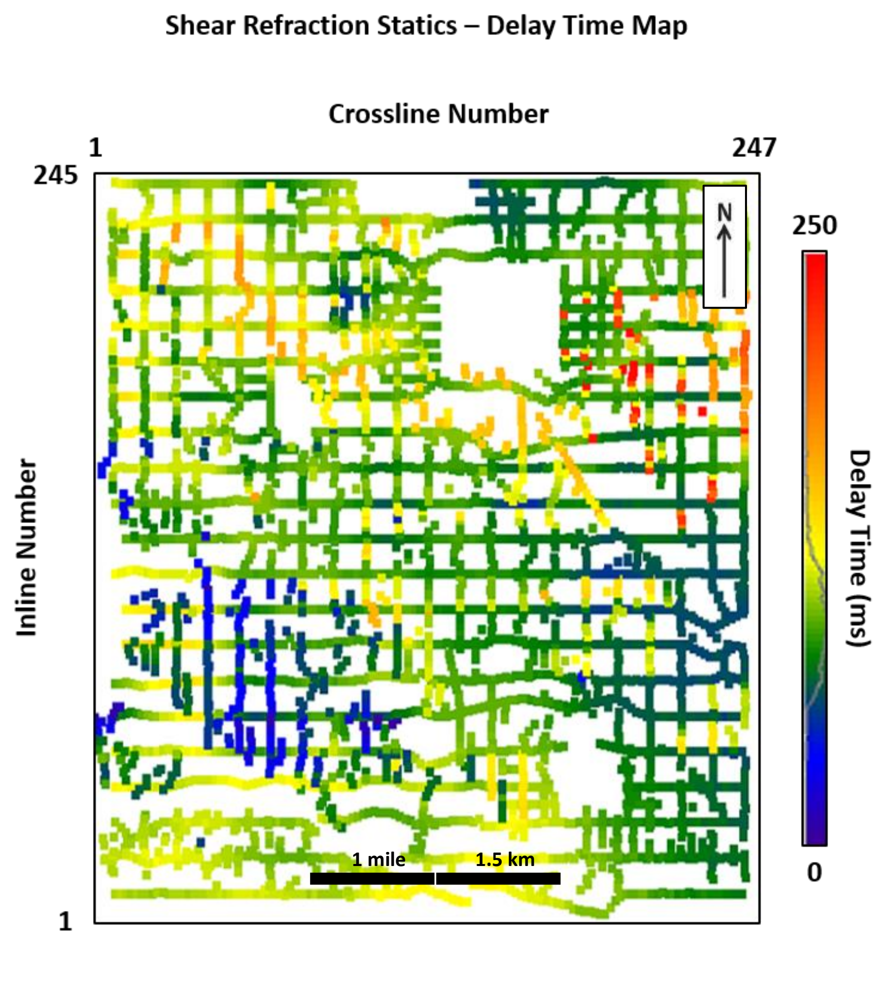

Figure 5.5: Delay time map in milliseconds from the shear-refraction statics solution.

5.3 Velocity analysis

5.3.1 Linear regression

Velocity analysis for shear-waves is of the utmost importance when imaging for converted-waves. An initial estimation of the shear-wave velocity is done by generating a relationship of P-wave velocity and S-wave velocity from well-logs at RSU-#1 well. Such a relationship of V_s in terms of V_P is generated by linear regression and is then applied to the P-wave migration velocity volume from PP reflection processing. The shear-wave velocity is of critical importance in the converted-wave processing and can be used in NMO application, ACP binning, and Kirchhoff migration. Figure 5.6 displays the $\frac{V_p}{V_s}$ relationship determined at the well location. The Equation of Vs in terms of V_P is displayed in Equation 7.

$$V_s = -1905.4 + 0.7V_p \tag{7}$$

Where V_s is S-wave velocity and V_p is P-wave velocity. Figure 5.7 shows the P-wave migration velocity field and the calculated S-wave velocity field. The values of shear-wave velocity range from 3,974 ft/s (1,211 m/s) and 13,880 ft/s (4,231 m/s). The values for $\frac{V_p}{V_s}$ range from 1.58 to 3.3.

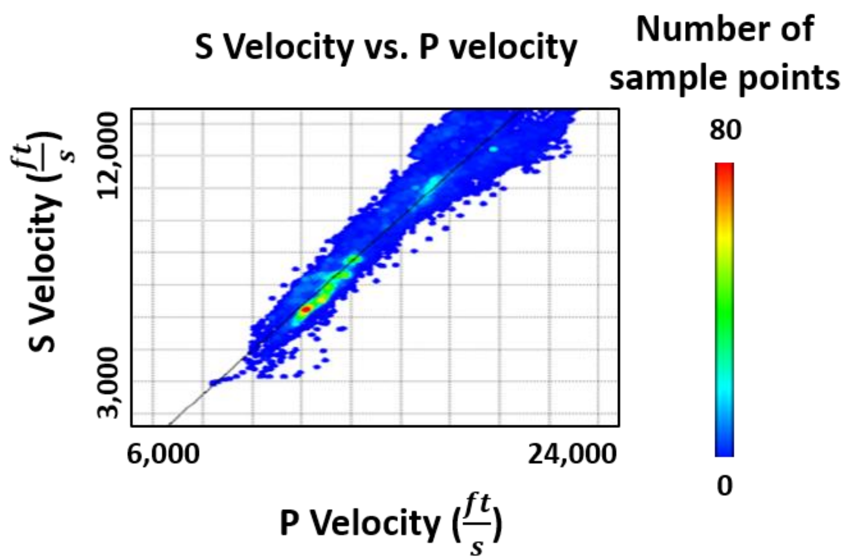

Figure 5.6: $\frac{V_p}{V_s}$ cross-plot utilized for the linear-regression generation. The color bar represents the number of sample points in the cross-plot.

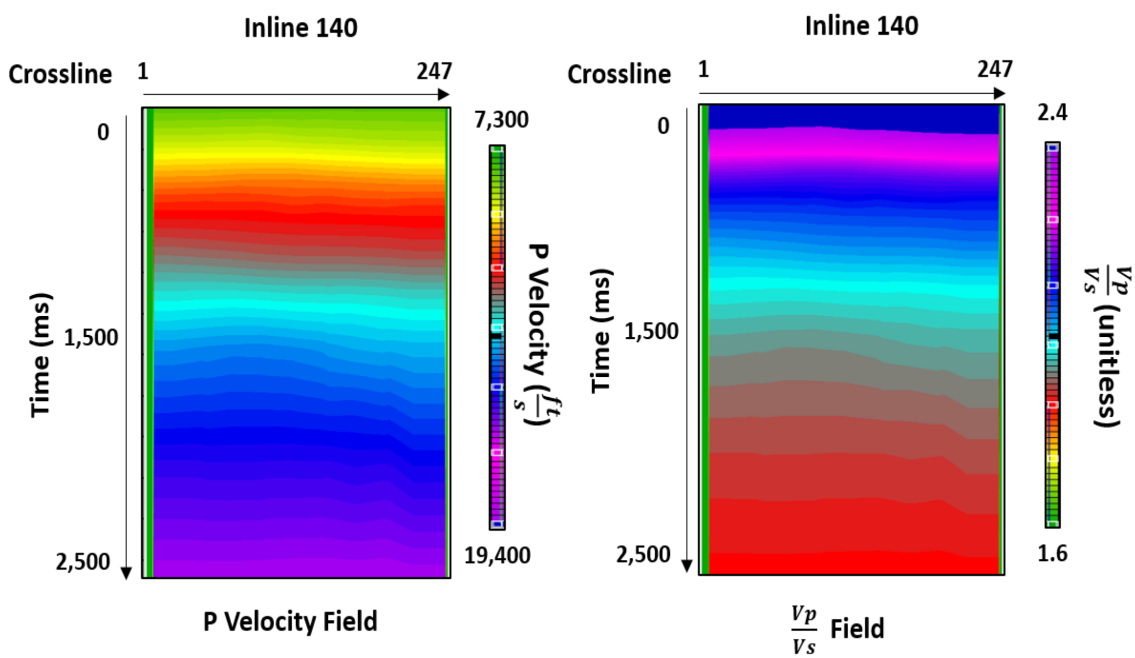

Figure 5.7: V_P migration velocities from PP processing and $\frac{V_p}{V_s}$ field volume calculated from the linear regression.

5.3.3 Migration-velocity analysis

Although a shear-wave velocity model from linear regression is accurate at the well location, the values of shear-wave velocities may vary within the survey due to lithology, fluid saturation, or near-surface condition variations. Shear-wave velocities are generated with more spatial accuracy by a migration-velocity analysis.

This velocity determination method involves the migration of target lines within the survey with increasing percentages from the initial shear-wave velocity model and utilizing the migrated result to determine the optimal velocity that can be used for migration. The migration is done with 50% - 300% of the initial velocity model for each of the target lines. Subsequently, stacks are generated with each of the migrated gathers from each percentage as well as coherency traces for semblance analysis. The optimal shear-wave velocity is then picked by analyzing the highest coherency points as well as the highest signal-to-noise ratio from the stack response using migrated stacks and coherency volumes.

Figure 5.8 shows velocity picks from the semblance analysis and migrated stack response for the migration-velocity analysis. From coherency values and migrated stacks, the near-surface $\frac{V_p}{V_s}$ indicates to be around 3.0, while the target interval indicates to be approximately 1.72. Such $\frac{V_p}{V_s}$ from the migration-velocity analysis picks are conformant with the information gathered at the well and near-surface statics velocity for converted-waves.

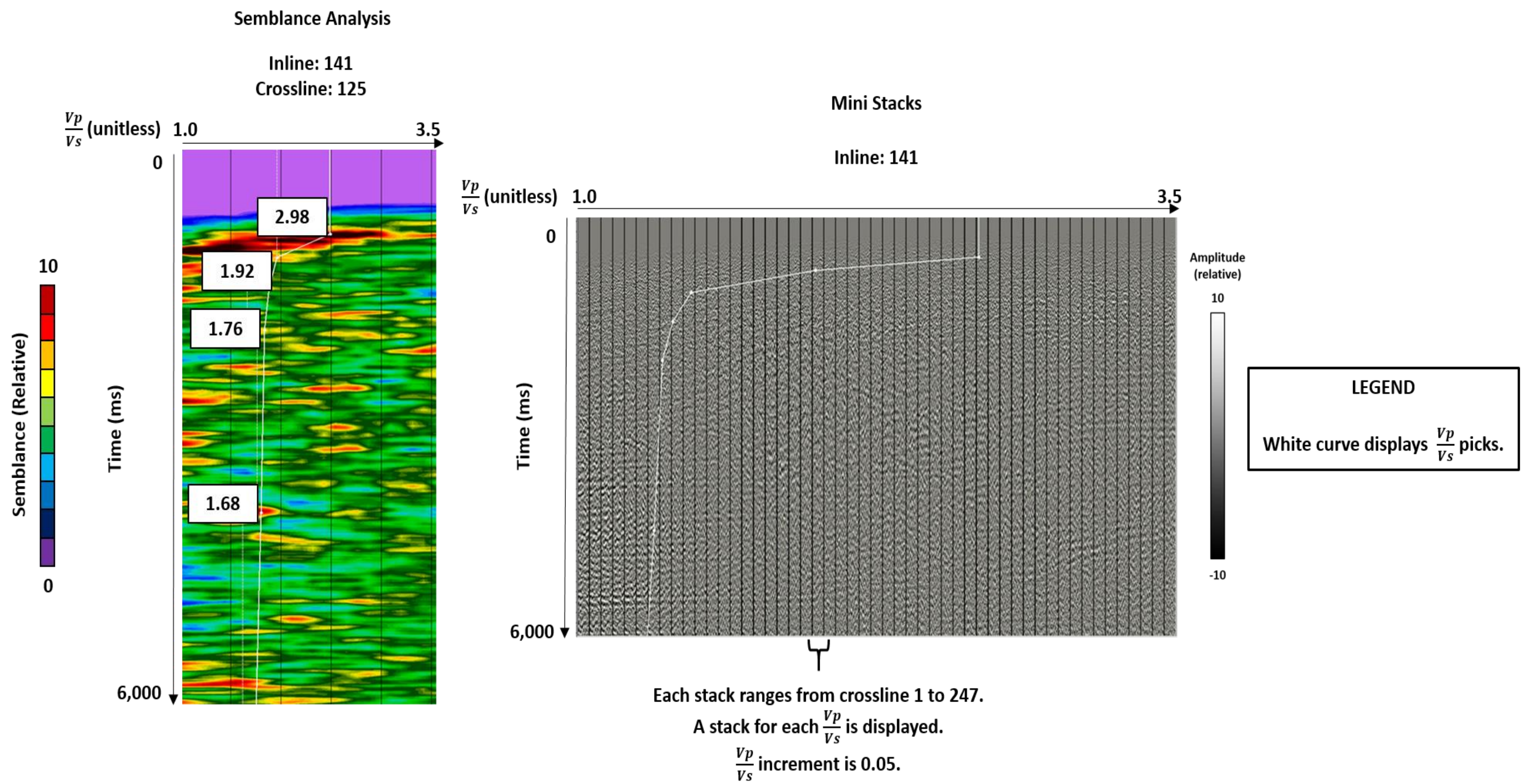

Figure 5.8: Migration velocity analysis demonstrated from velocity picks from semblance analysis (left) and migrated stack response (right).

5.4 Processing

5.4.1 Radial and transverse rotation

Rotation from field coordinates to radial and transverse coordinates is of importance to obtain higher signal-to-noise values for converted-waves (Grossman et al., 2013). In preparation for further processing PS Kirchhoff migration, the sources and receivers are mathematically rotated into radial and transverse coordinates (Gaiser, 1999; Simmons, 2001), where the radial direction, R, is defined as the azimuth of the vector originating from the source and pointing toward the receiver, and the transverse direction, T, is perpendicular to the radial direction (Figure 5.9) (Grossman et al., 2013). Figure 5.10 displays CDP gathers for the X and Y components before and after rotation to the radial and transverse directions.

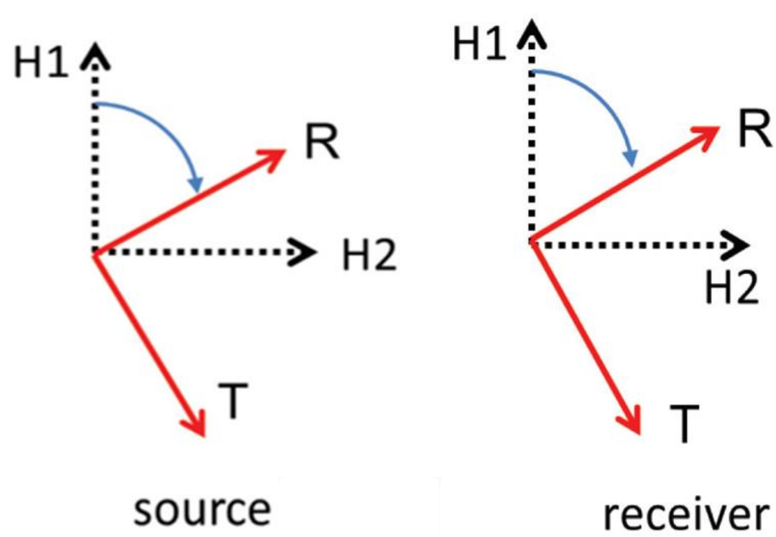

Figure 5.9: Schematic diagram displaying radial and transverse directions along with acquisition shot and receiver lines, H1 and H2 (from Grossman et al., 2013).

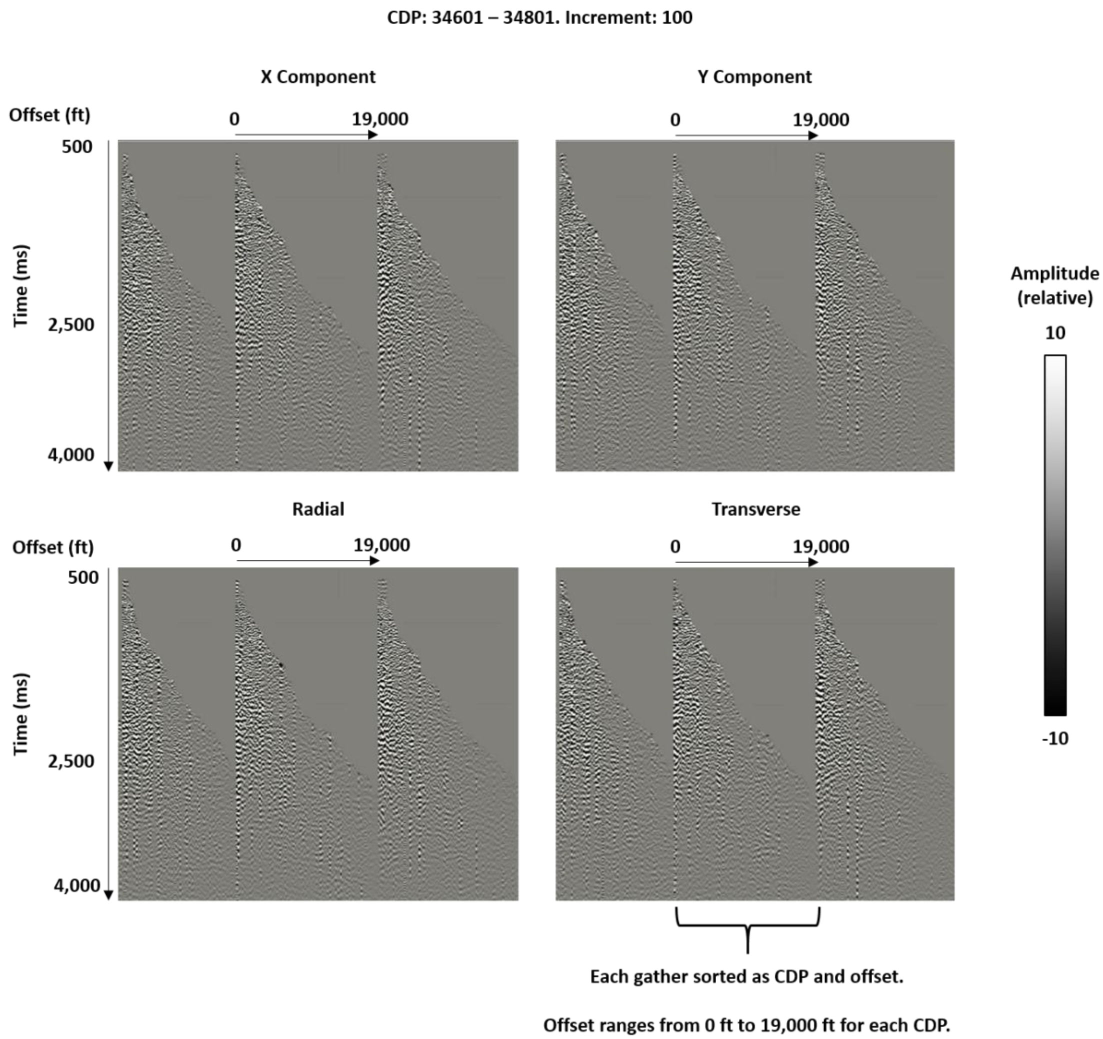

Figure 5.10: Converted-wave CDP gathers for X and Y components before and after rotation to its corresponding radial and transverse. Offset ranges from 0 – 19,000 ft for each CDP gather.

5.4.2 Converted-wave binning

For an earth model with flat layers, the PP reflection points coincide with the midpoint locations (CMP), whereas, the PS conversion points do not. As a direct consequence, the notion of a CMP gather based on sorting PP data from acquisition coordinates does not apply to PS seismic data. Instead, a Common Conversion Point (CCP) sorting is done for PS data that gathers traces in the same conversion point coordinate. An essential aspect of CCP sorting is that the asymmetric ray path associated with the PS reflection gives rise to a periodic variation in the fold of the CCP gathers. At infinite depth, the CCP reaches an asymptotic conversion point (ACP) coordinate with respect to the source location (Figure 5.11) (Tessmer and Behle, 1988). ACP binning is done to the radial and transverse seismic volumes by using the P and S-wave velocities.

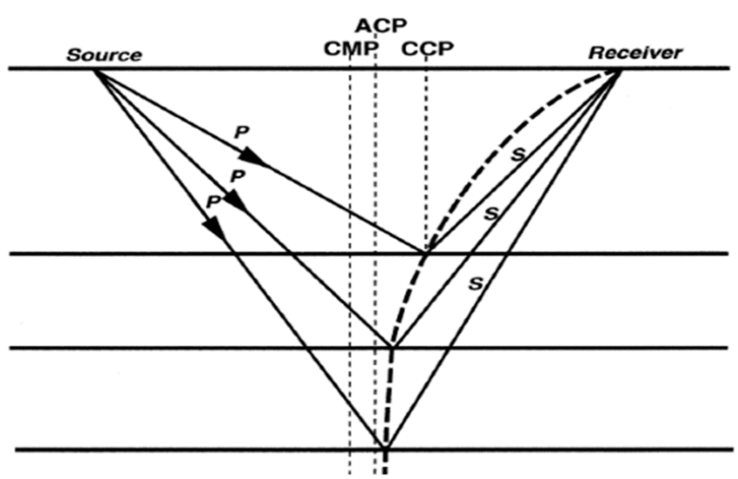

Figure 5.11: Schematic diagram showing the CMP, CCP, and ACP coordinates for a source and receiver pair (modified from Tessmer and Behle, 1988).

5.4.3 Kirchhoff migration

Converted-wave Kirchhoff migration images the subsurface by utilizing the P-wave velocity from the source to the image point and the S-wave velocity from the image point to the receiver. The algorithm output is migrated in PS time by applying a 1.5D isotropic ray-tracing technique to image converted-waves in the subsurface. The migration aperture used is 20,000 ft (6,096 m) and maximum angle to migrate is set to 60 degrees. The velocity used for the down-going wave velocity is the P-wave migration velocity while the up-going velocity used is the S-wave velocity from the migration-velocity analysis picking. Additionally, residual statics are applied by using the PP stack in PS time as a pilot trace and allowing +20 / -20 ms shifts to the traces to align the reflection events further. Figure 5.12 shows a stack section for before and after the converted-wave Kirchhoff migration and residual statics are applied.

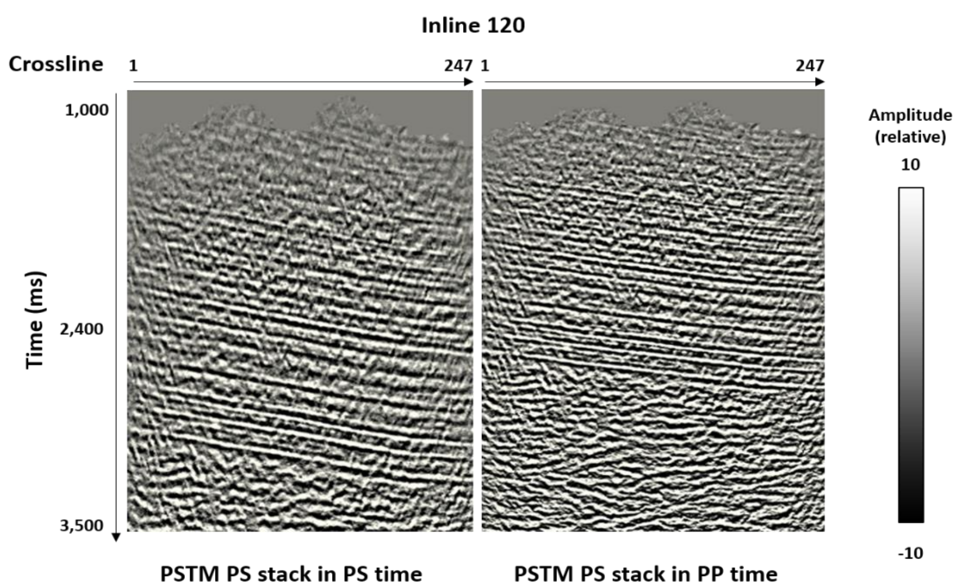

Figure 5.12: Display of converted-wave stack before (left) and after (right) the Kirchhoff migration and residual statics are applied.

5.4.4 PP – PS event registration

Travel time variations from the PP and PS reflection events occur from the difference in P and S-wave propagation velocity. This results in the signal from the converted-wave being recorded by the receiver in a long time in comparison to the primary wave reflections. After an image of converted-waves is generated for the subsurface, a comparison of arrival times for target events in the PP and PS migrated seismic data is done. The difference in arrival times for the same reflection event is compensated by applying bulk shifts along with stretches and squeezes to match the same reflection events in the PP and PS reflection stacks. Reflections of interest include the Frontier shale, Nugget and Weber sandstones, and Madison limestone. Figure 5.13 displays a stack section before and after the event registration.

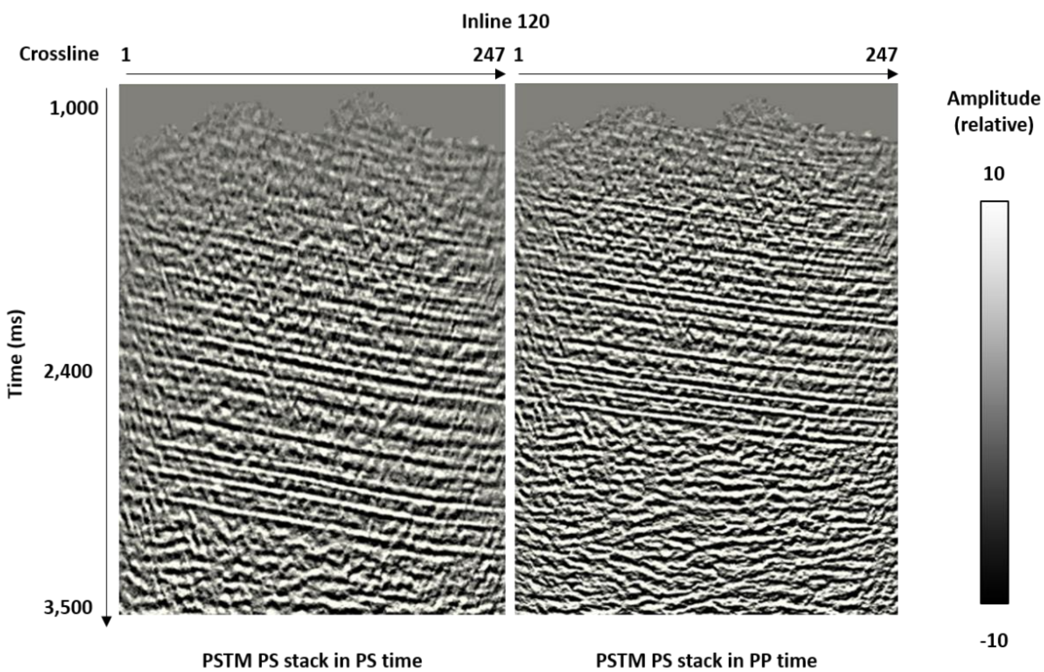

Figure 5.13: Display of stack before (left) and after (right) the event registration.

The PP and PS stacks are compared, in PP time, after the event registration is applied to the PS stack (Figure 5.14). The top of the nugget sandstone is represented by a trough at roughly 1,700 ms, while the top of Weber sandstone is represented by a trough at roughly 1,950 ms. The top of Madison limestone is also represented by a trough at roughly 2,050 ms. The PP and PS stacks in PP time show the major geologic reflections are aligned after the event registration.

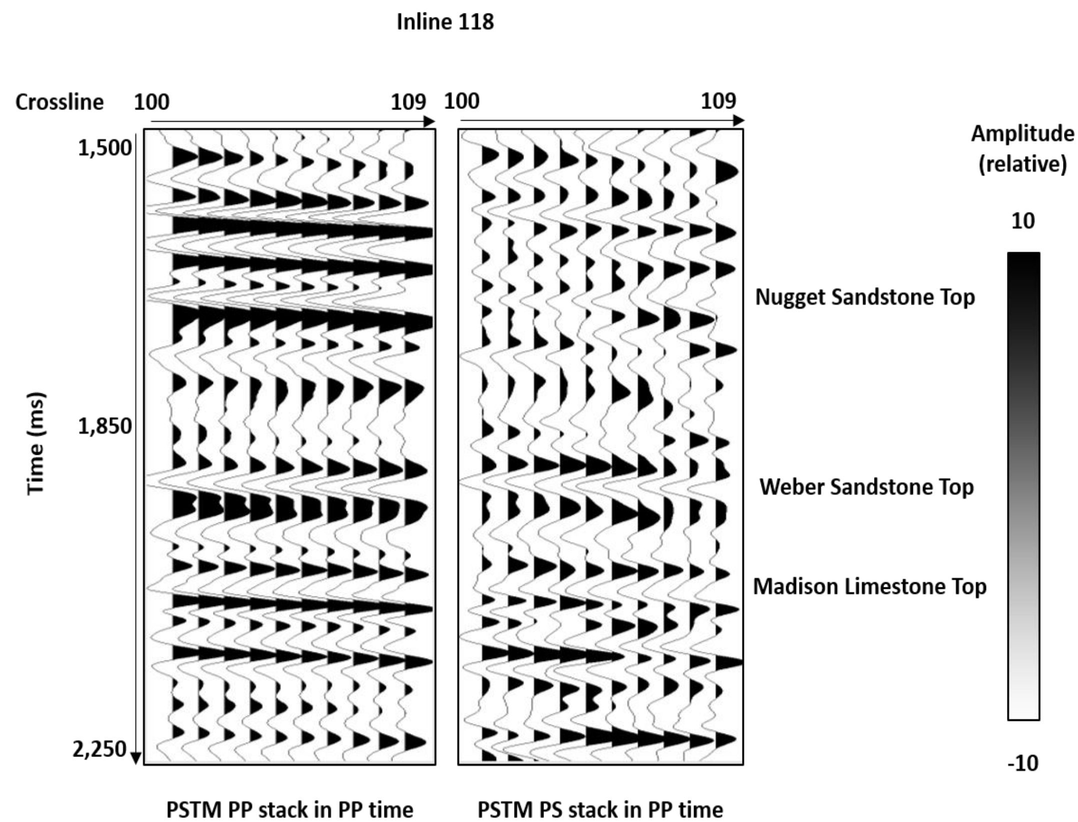

Figure 5.14: Comparison of the PP stack and PS stack after the event registration in PP time. The Nugget sandstone, Weber sandstone, and Madison limestone tops are annotated.

5.5 Shear post-stack inversion

5.5.1 Shear well-to-seismic correlation

Well-to-seismic correlation with the converted-wave data in PP time is done to understand the seismic response and generate a relationship from well rock properties to converted-wave amplitudes. A spectral and wavelet analysis is also done to determine the frequency bandwidth and phase of the data. A synthetic is generated using the convolutional model with V_s and density logs. Figure 5.15 demonstrates the well-to-seismic correlation utilizing a synthetic calculated from logs at RSU-#1 well. The seismic data and the synthetic show a high correlation of approximately 68% within the target window.

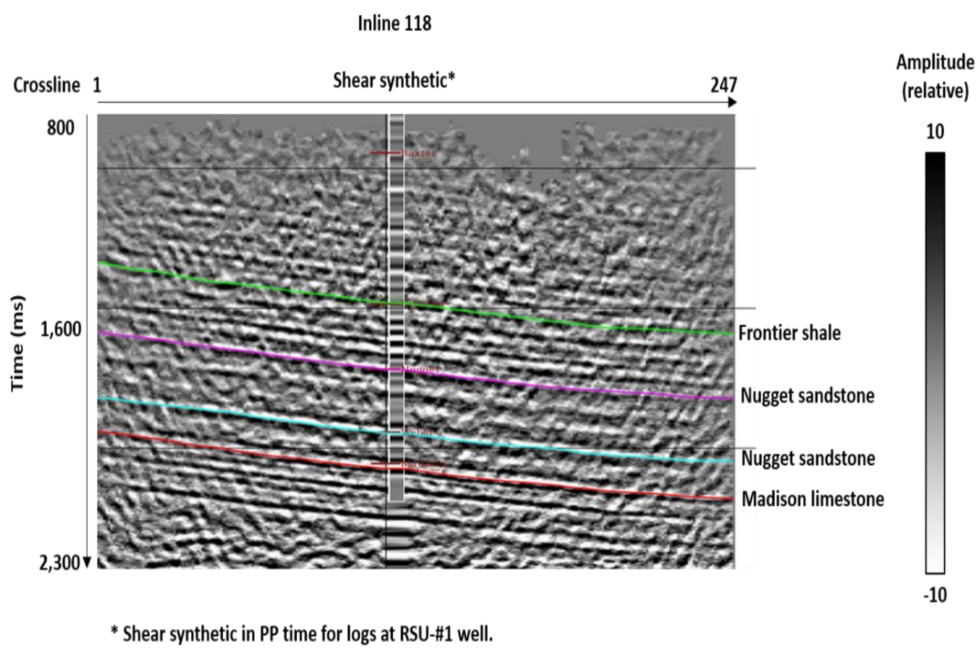

Figure 5.15: Well-to-seismic correlation for the converted-wave stack at the RSU-#1 location.

The wavelet extracted at the RSU-#1 well location for the converted-wave stack demonstrates a frequency bandwidth of approximately 5 Hz to 60 Hz, higher in comparison to the PP seismic stack; thus, a higher resolution is expected from the converted-wave seismic data. The phase of the extracted Roy-White wavelet at the target interval ranges from 0 to -10 degrees. Figure 5.16 displays the extracted wavelet, spectrum, phase, and cross-correlation for the converted-wave stack at RSU-#1 well location. The wavelet scalar extracted for the seismic data is 0.018. The wavelet and scalar extracted are used in conjunction with the S impedance frequency background model and converted-wave stack to generate an S impedance volume through a post-stack inversion.

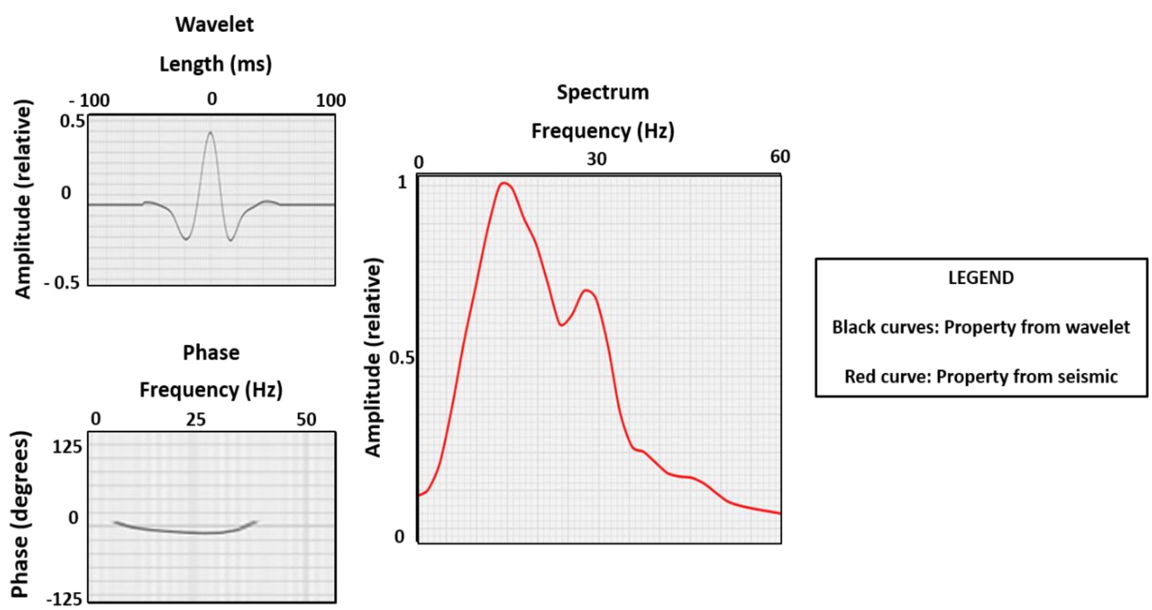

Figure 5.16: Extracted wavelet, spectrum, phase for the converted-wave seismic stack at the RSU-#1 well location.

5.5.2 Post-stack inversion

Converted-wave post-stack inversion utilizes the stack section, S impedance background model, extracted wavelet and scalars to generate a volume of shear impedance. In a model-based inversion, a simple initial acoustic impedance model is convolved with the wavelet to obtain a synthetic response that is compared with the actual seismic trace. The impedance model is altered iteratively until the difference between the inverted trace and the seismic trace is reduced to a threshold value (Veeken and Da Silva, 2004). A model with a minimal difference is accepted as a solution. An advantage of model-based inversion is that it gives satisfactory results, even with limited well control and poor-quality seismic. The seismic dataset itself acts as the guide for the inversion, and a wavelet can be easily derived straight from the seismic. The least-squares inversion method is a type of model-based inversion where the threshold value is the smallest least-squares error (Veeken and Da Silva, 2004).

Post-stack inversion for shear impedance is calculated by assuming the seismic response of shear-shear reflections is characterized by the converted-wave data. Figure 5.17 shows a section of the shear impedance inversion at inline 118, the location of the well RSU-#1. The values of the shear impedance range from 11,495 $\frac{gf}{cm^3 s}$ and 31,368 $\frac{gf}{cm^3 s}$. The inversion volume is used to extract shear impedance RMS maps at the target Nugget and Weber sandstones to determine anomalies that may be correlated to high-porosity areas within the survey.

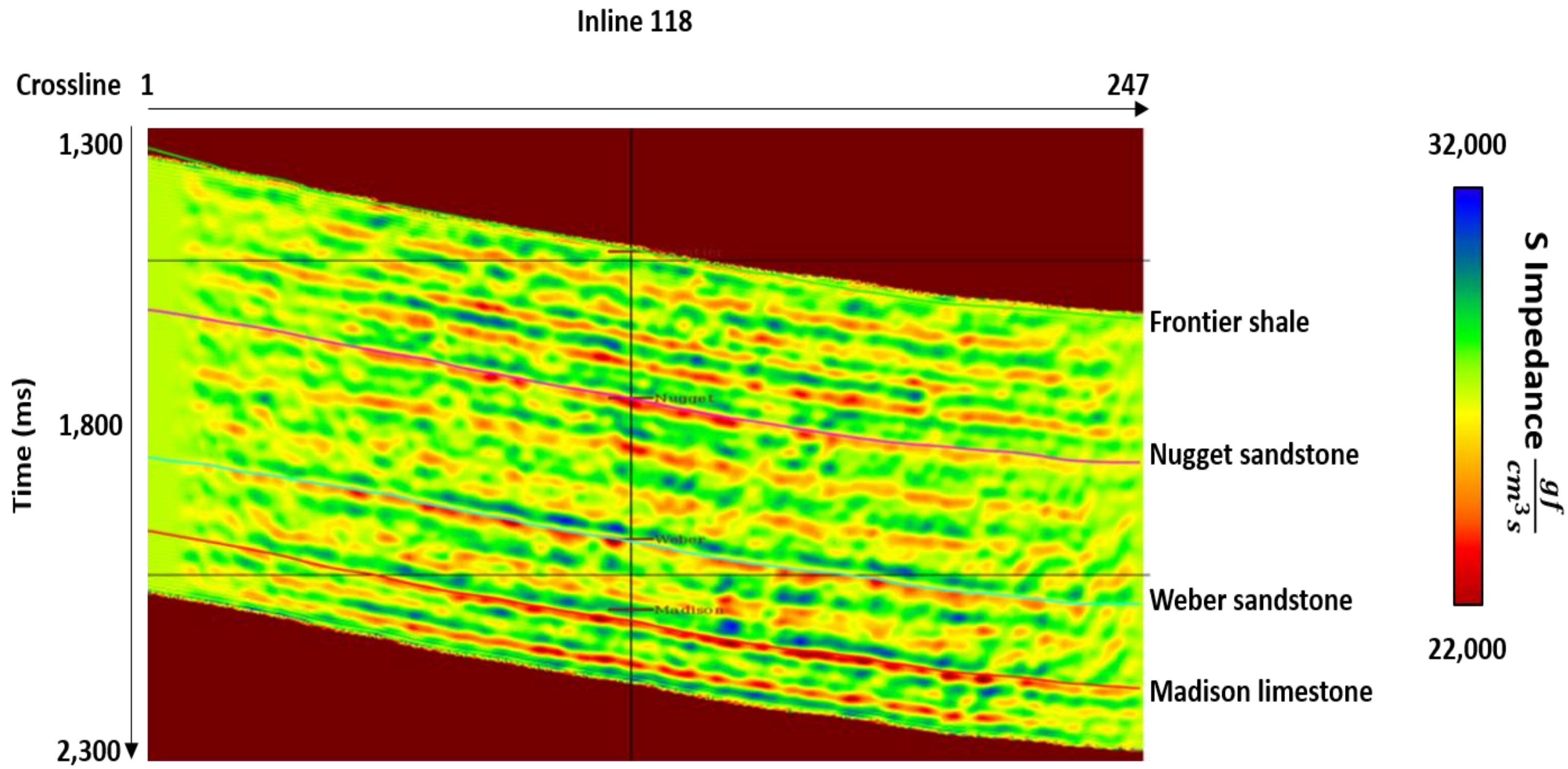

Figure 5.17: Shear impedance volume generated from the converted-wave seismic section. Shear impedance inversion volume is displayed at the well RSU-#1 location.

Chapter 6

Interpretation

To characterize the reservoir and determine the potential volume for carbon dioxide storage within the survey area, the outputs from the AVO inversion, calculated elastic and seismic attributes, and azimuthal anisotropic analysis from velocity variations with azimuth are analyzed together to gain insight into areas with increased void volume within the target sandstones. A rock physics relationship is generated at the well to determine porosity in terms of shear modulus, and such a relationship is applied to the inversion volumes to obtain a spatial characterization of porosity. Porosity anomalies are validated through multi-attribute analysis, and a regional stress field is derived from the azimuthal anisotropic analysis. A location for carbon dioxide sequestration is proposed within the Jim Bridger 3D survey area. A carbon dioxide injection model is created, and a volumetric analysis is done to determine the potential capacity and possible duration of carbon dioxide sequestration for the Jim Bridger power plant.

6.1 Porosity estimation

6.1.1 Linear regression

To estimate porosity, a linear regression is fit using various attributes derived from the well-logs such as P impedance, S impedance, density, $\mu\rho$, and $\lambda\rho$. Linear relationships between porosity and such attributes are generated to identify the attribute pair demonstrating the highest cross-correlation. Density is known to be highly correlated to porosity values, but additional factors such as fluid saturation can alter this trend. The cross-correlation of density and porosity from cross-plot analysis at the well is 66%.

As additional attributes are investigated, a normalized $\mu\rho$ is determined to be highly correlated with porosity values with a cross-correlation value of 93%. Since $\mu\rho$ is the product of squared shear impedance times density, the effect of fluid saturation is neglected as S-waves do not propagate through fluids; thus, normalized $\mu\rho$ is found to be a reliable proxy for porosity values at the well-location, and such a derived relationship can be applied to attributes obtained from the AVO pre-stack inversion. Equation 8 demonstrates the equation derived at the well location.

$$\phi = 0.25 - 0.0034\mu\rho \tag{8}$$

Where ϕ is porosity, μ is the shear modulus, and ρ is density. Figure 6.1 displays a cross-plot of porosity vs. density and porosity vs. λρ. From the cross-plots, μρ and density have higher a cross-correlation. It is noted that lower density values and lower μρ values correspond to higher porosity values, but the trend is better defined utilizing the μρ attribute since it discriminates fluid saturation.

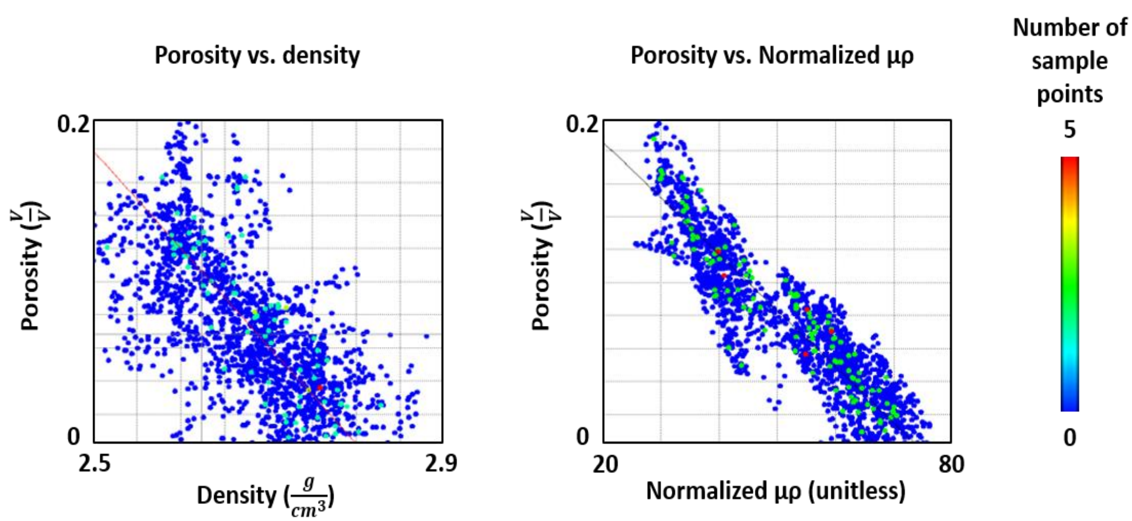

Figure 6.1: Linear regression analysis from well attributes. Porosity vs. density (left) and porosity vs. μρ (right).

6.1.2 Porosity volume

The equation relating porosity to μρ derived from the well, Equation 8, is applied to the μρ attribute obtained from the AVO pre-stack inversion to determine a porosity volume. Figure 6.2 displays a porosity section from inline 118. The top and base horizons for the Nugget and Weber sandstones are displayed on the section. These horizons are picked to later obtain isopach maps of the target intervals for volumetric calculations of CO_2. The values from the porosity volume range from 5% to 22%. The Nugget sandstone displays an average value of 16% porosity, while the Weber sandstone displays an average value of 12% porosity.

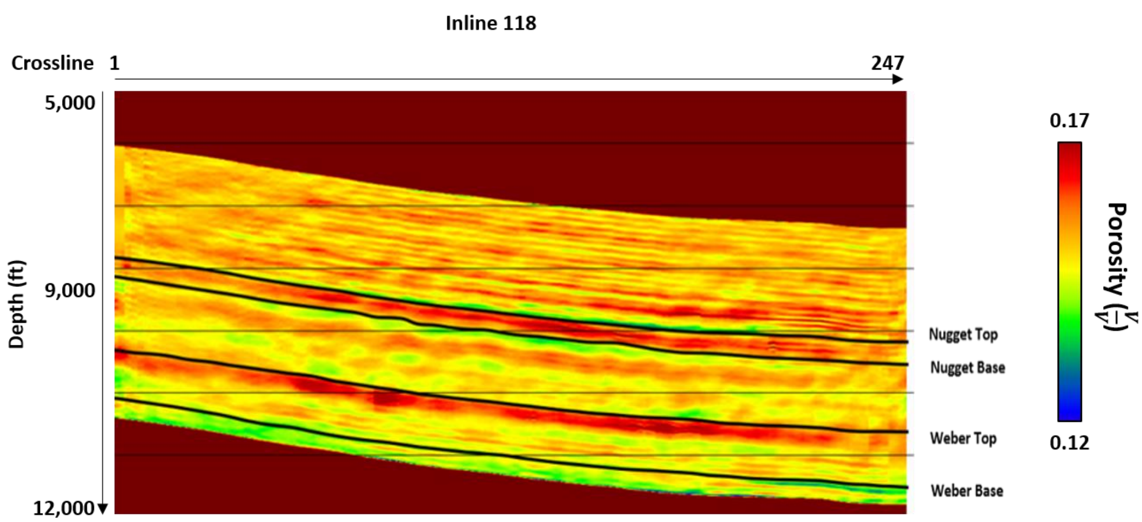

Figure 6.2: Porosity section derived by applying the porosity – μρ transform to the μρ volume from the AVO inversion. Top and base of the Nugget and Weber sandstone horizons are displayed.

Equation 8 is also applied to the μρ volume obtained from post-stack inversion from the PS stack in PP time. Shear-waves have a higher sensitivity to the rock matrix and are not influenced by the saturating fluid within the formation; thus, the resultant porosity volume obtained from PS post-stack inversion is potentially more accurate. Figure 6.3 displays the porosity volume obtained from the S impedance post-stack inversion. The porosity volume also displays higher resolution that could aid in the interpretation for CCS.

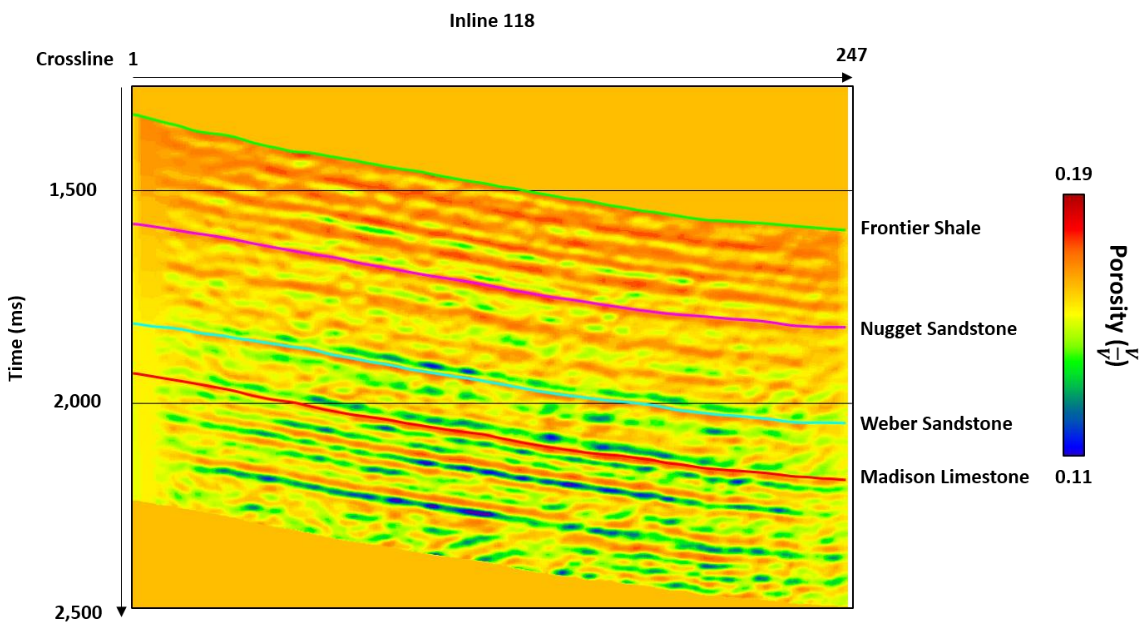

Figure 6.3: Porosity section derived by applying the porosity – μρ transform to the μρ volume from the PS post-stack inversion. Frontier shale, Nugget and Weber sandstones, and Madison limestone horizons are displayed.

6.1.3 Porosity map

Porosity maps are generated by extracting the RMS value from the top of the formation to the base of the geologic formation for the entire volume. Analysis of the RMS map indicates the geographic locations within the survey where higher or lower porosity values can be expected for each geologic formation of interest. Figure 6.4 displays a porosity map for the geologic formations of the Nugget and Weber sandstones. The map shows higher values can be found on the east side of the survey with porosity values ranging from 12.6% to 18.4% for both the Nugget and Weber sandstones. For CCS, higher porosity is of utmost importance, since a high-volume geologic compartment is required for the storage of large volumes of carbon dioxide. Although analysis suggests the east-side is of interest, further investigation with additional attributes is done to verify the high-porosity sandstone locations within the survey.

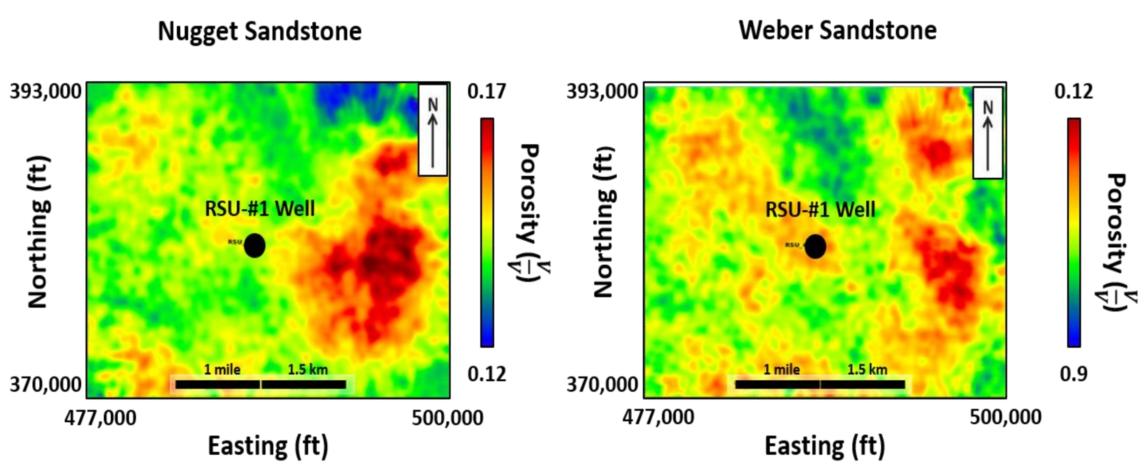

Figure 6.4: Porosity maps extracted from top to base of the formation for the Nugget sandstone (left) and the Weber sandstone (right).

6.2 Attribute volumes

6.2.1 λρ and μρ

λρ and μρ attributes are indicators of fluid saturation, lithology, and rock properties. λ is inherently indicative of fluid saturation since it largely uses information from P-wave propagation, which is profoundly affected by fluid saturation. On the other hand, μ is a function of the matrix, which is not affected by fluid saturation within the rock's pores and is thus a proxy for lithology and high porosity. Attributes of λρ and μρ are extracted for the formation interval for both Nugget and Weber sandstones. Figure 6.5 displays extracted RMS maps for the Nugget sandstone for λρ and μρ. Higher values of λρ and lower values of μρ are observed in the east-side of the survey, suggesting higher reservoir quality lithology.

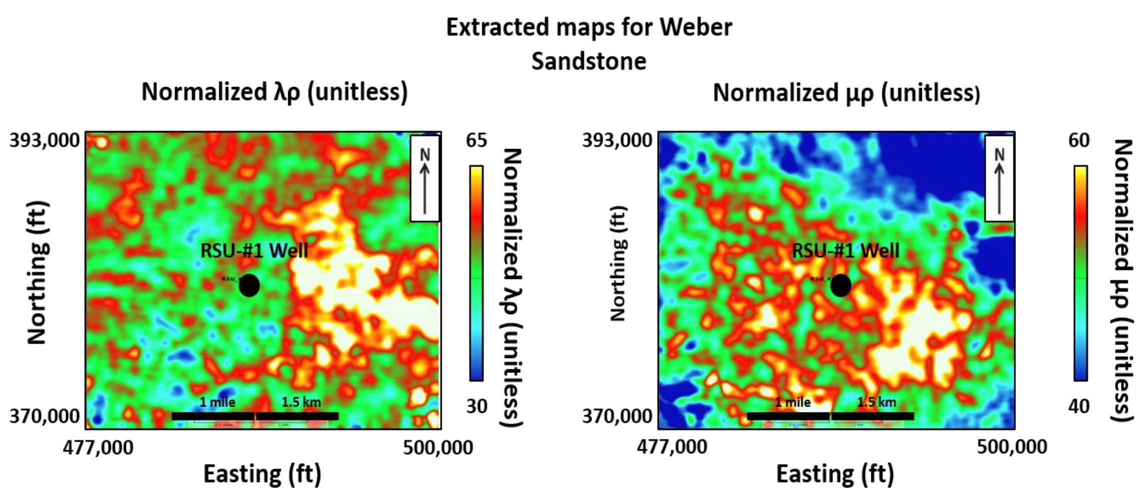

Figure 6.5: λρ and μρ map for the Nugget sandstone interval.

6.2.2 Gradient and fluid factor

The AVO gradient and fluid factor are pre-stack derived attributes that can indicate high-porosity sandstones and fluid saturation type (Jensen et al., 2016). Both seismic attributes take advantage of the AVO effect for the reflection events and can indicate fluid saturation and rock properties.

The Gradient (G) can be estimated from seismic data by a least-squares regression applied to constant time slices of moveout corrected common reflection point gathers. Care must be taken when determining the G to avoid bias caused by the curvature term either by excluding large angles, typically above 30^{o}, or by using a 3-term fit and discarding the third term (Wiggins et al., 1985; Aki and Richards, 2002). Aki-Richards linearization of the Zoeppritz equation is demonstrated by Equation 9. The gradient is the second term, B, which is used as an attribute with information regarding V_P, V_S, and density. Where k is a constant.

$$R(\theta) \approx A + Bsin^2\theta + Csin^2\theta tan^2\theta \tag{9}$$

Where

$$A = \frac{1}{2}\left(\frac{\Delta V_p}{V_p} + \frac{\Delta \rho}{\rho}\right) \quad B = \frac{\Delta V_p}{2V_p} - 4k\left(\frac{\Delta V_s}{V_s}\right) - 2k\left(\frac{\Delta \rho}{\rho}\right) \quad C = \frac{\Delta V_p}{2V_p}$$

Smith and Gidlow (1987) used the ARCO mud-rock equation, which is the straight-line fit that appears to hold for water-bearing clastic around the world, to derive the fluid factor. Equation 10 can be differentiated and expressed in ratio form. The fluid factor, F, can be defined as Equation 11 (Castagna and Backus, 1993).

$$V_p = 1360 + 1.16V_s \left(velocities\ in\ \frac{m}{s}\right) \tag{10}$$

$$\Delta F = \frac{\Delta V_p}{V_p} - 1.16\frac{V_s}{V_p}\frac{\Delta V_s}{V_s} \tag{11}$$

Figure 6.6 displays extracted RMS maps for the gradient and fluid factor attributes for the Weber sandstone formation. Both attributes display anomalies in the eastern side of the survey, suggesting a possible area for higher porosity sandstones and ultimately for CCS.

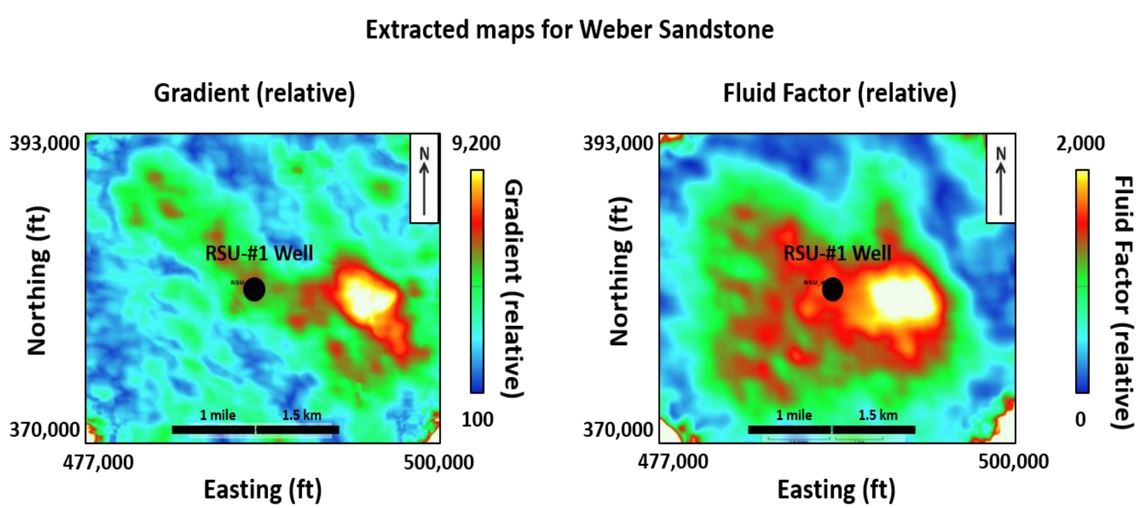

Figure 6.6: Gradient (left) and fluid factor (right) RMS maps for Weber sandstone formation.

6.2.3 Poisson's ratio

Poisson's ratio is an elastic parameter that defines the ratio of transverse contractional strain to longitudinal extensional strain. It is a measure of the degree to which a material expands outwards when squeezed, or equivalently contracts when stretched (Sheriff, 2002). The following equation 15 is used to calculate σ for isotropic homogeneous media.

$$\sigma = \frac{(\frac{V_p}{V_s}^2) - 2}{2(\frac{V_p}{V_s}^2) - 2} \tag{12}$$

Where σ is Poisson's ratio. Typically, lower values of Poisson's ratio defined a "softer" higher porosity lithology or a fluid-saturated rock. From the sensitivity analysis in chapter 2, it is evident that a decrease in σ indicates a higher porosity rock. Figure 6.7 displays an RMS map for Nugget sandstone for σ. Results demonstrate lower values in the eastern side for Nugget sandstone indicating a region of higher porosity, which correlates with the previous extracted RMS porosity map.

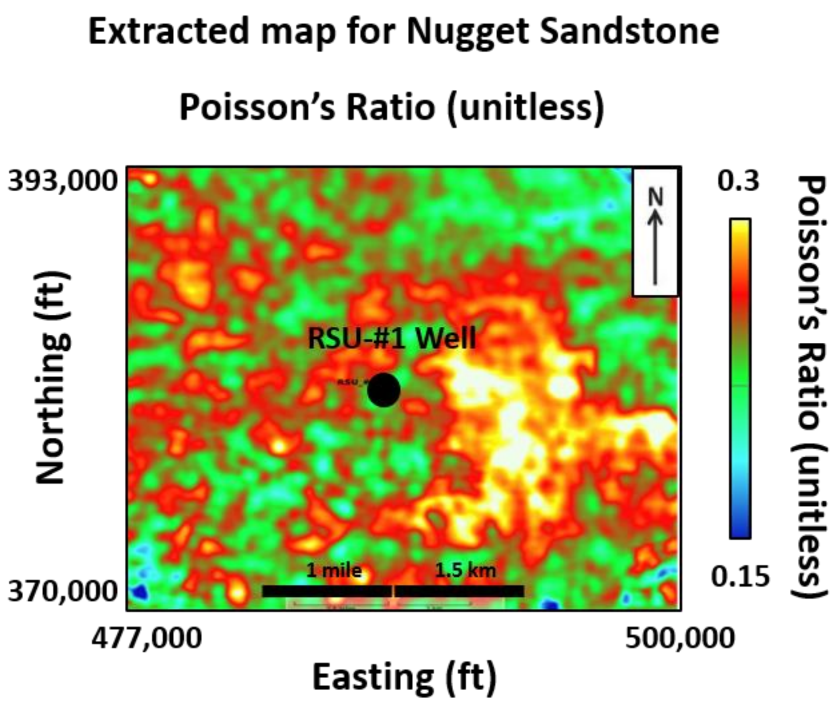

Figure 6.7: Poisson's ratio RMS map extracted for the interval of the Nugget sandstone.

6.2.4 Sweetness and spectral decomposition

Sweetness is calculated by dividing the instantaneous amplitude (amplitude envelope) by the square root of the instantaneous frequency (Hart, 2008). The amplitude envelope is the magnitude of each pair of polar values produced by applying a Hilbert transformation to the original seismic trace.

The value of the instantaneous amplitude is independent of phase. Higher amplitudes events are often associated with changes in lithology or act as DHI's (Hart, 2008). On the other hand, the instantaneous frequency is the vertical derivative of the phase. In other words, how the phase changes with each sample. Sweetness is a composite seismic attribute used to highlight thick, clean reservoirs, along with hydrocarbons contained within. Areas containing higher amplitudes and lower frequencies (sandy intervals) will display the highest values for sweetness, while the lower amplitude and higher frequency sediments (thinly bedded shales) will show lower values for sweetness (Hart, 2008).

Figure 6.8 displays sweetness attribute RMS map extracted for the Weber and Nugget sandstone interval. Both attributes demonstrate anomalies on the eastern side of the survey, although the Weber sandstone also shows an anomaly in the north-west side of the survey.

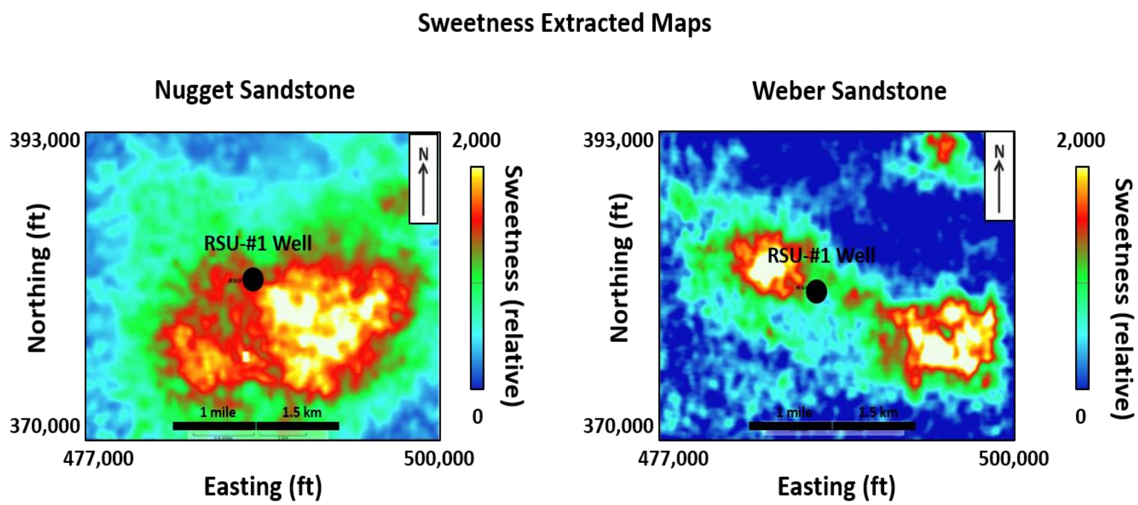

Figure 6.8: Sweetness attribute RMS map extracted for Nugget and Weber sandstone interval.

Additionally, spectral decomposition attributes are employed to decompose the data into multiple frequencies to investigate anomalies at different bandwidths. In this study, a spectral decomposition for 10 Hz, 30 Hz, and 50 Hz are computed, and RMS maps are extracted for the Nugget and Weber sandstones. Figure 6.9 displays the spectral decomposition RMS maps extracted. The nugget sandstone displays anomalies predominantly in the eastern side of the survey throughout all frequencies. Other anomalies also appear in the south-western side of the survey. For the Weber sandstone, the 10 Hz map shows an anomaly in the south-west side of the survey while the higher frequencies display anomalies in the eastern side of the survey. This suggests a possible hydrocarbon saturated area with lower frequency content in the south-western corner of the survey while a higher porosity area on the eastern side of the survey.

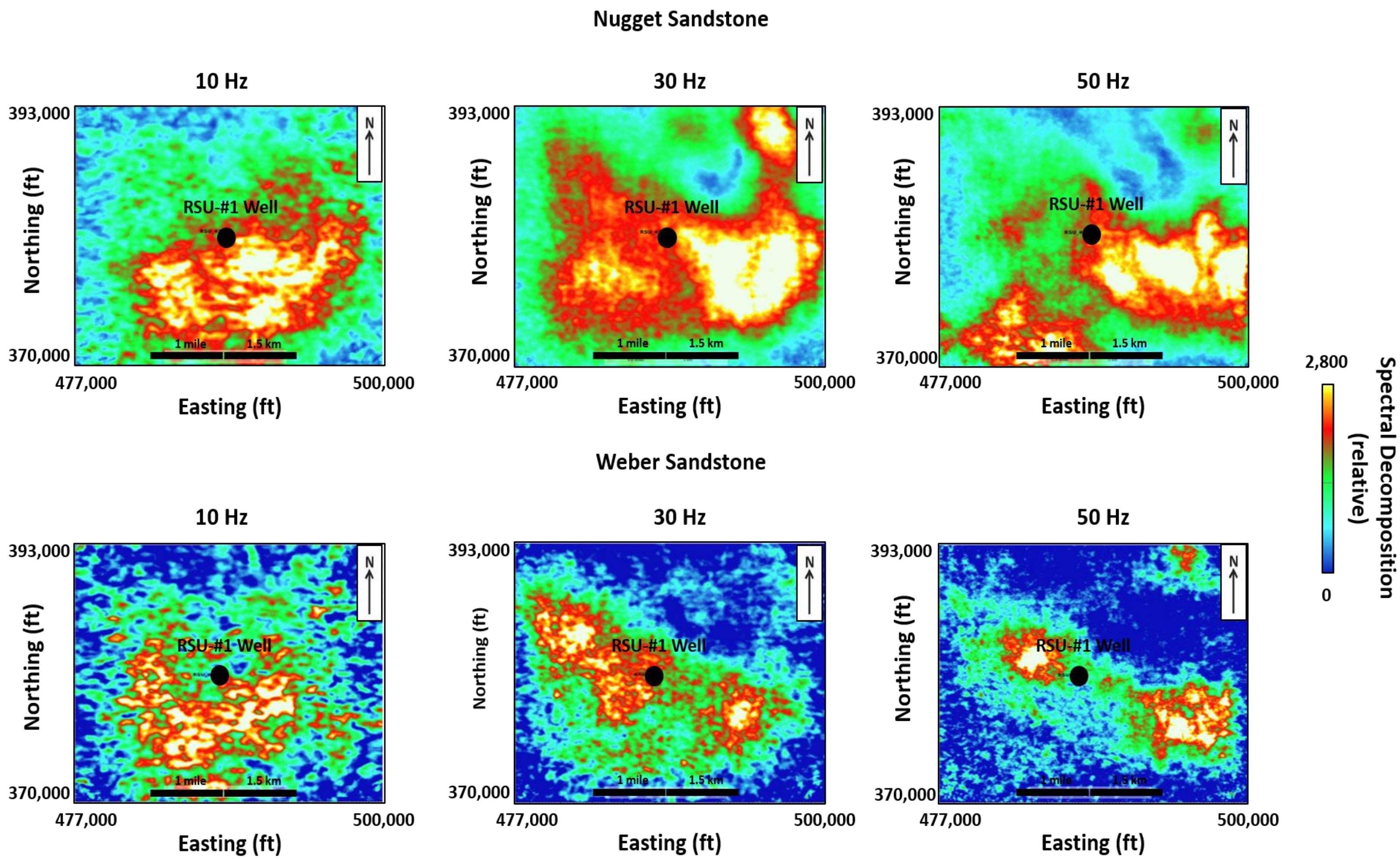

Figure 6.9: Spectral decomposition for 10, 20, 30 Hz for the Nugget and Weber sandstones, respectively.

6.3 Azimuthal anisotropy analysis

6.3.1 Anisotropy magnitude

Azimuthal anisotropy, also known as HTI, produces a pattern of slowness versus azimuth which is an ellipse. For azimuthal corrections, the algorithm decomposes arrival time "errors" caused by anisotropy into parameters estimating the elliptical anisotropy and uses a least-squares fitting to determine the parameters which best define the anisotropic ellipse. Anisotropy magnitude and azimuth generated from the azimuthal anisotropic analysis is a proxy for fracture-prone lithologies and the regional stress field. Figure 6.10 display extracted maps of the magnitude of anisotropy for the Nugget and Weber sandstones. The results display higher anisotropy in the northeastern and southeastern sides of the survey for the Nugget sandstone and higher anisotropy on the eastern side of the survey for the Weber sandstone.

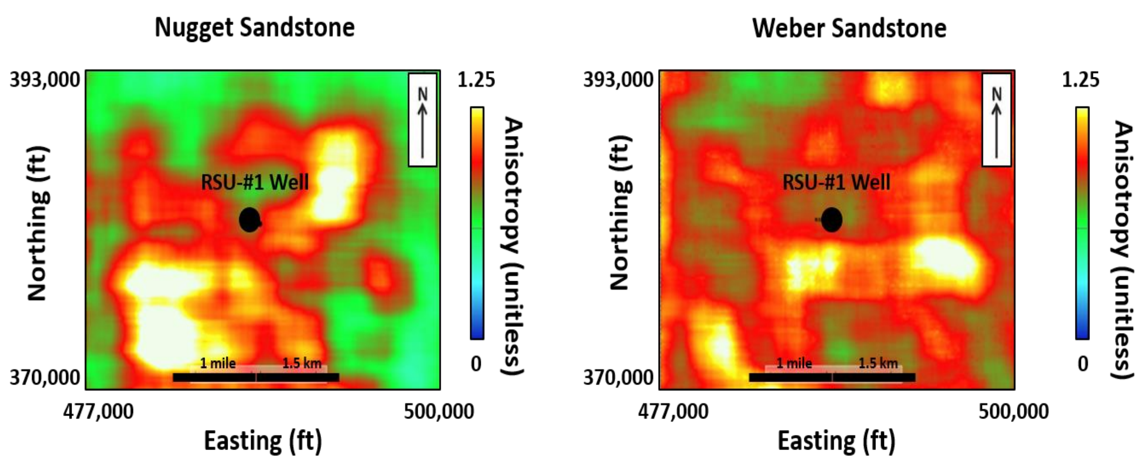

Figure 6.10: Magnitude of anisotropy maps extracted for the Nugget and Weber sandstones.

6.3.2 Anisotropy magnitude and azimuth

Azimuthal information from the azimuthal anisotropic analysis is incorporated by utilizing vector maps overlain on the anisotropy magnitude maps. Such maps display the direction of the anisotropy, hence a proxy for fracture orientation. For CCS, it is beneficial to obtain locations with a higher number of fractures since it may create additional voids for carbon dioxide storage. Figure 6.11 shows the anisotropic magnitude vector maps displaying anisotropy values and fracture orientation. For the Nugget sandstone, the general well-defined trend from the fracture orientations is in the direction of the northeast-southwest direction. On the other hand, the Weber sandstone does not have a clear pattern, and the azimuthal information can be affected by high amounts of noise and poor-signal from the azimuthal analysis.

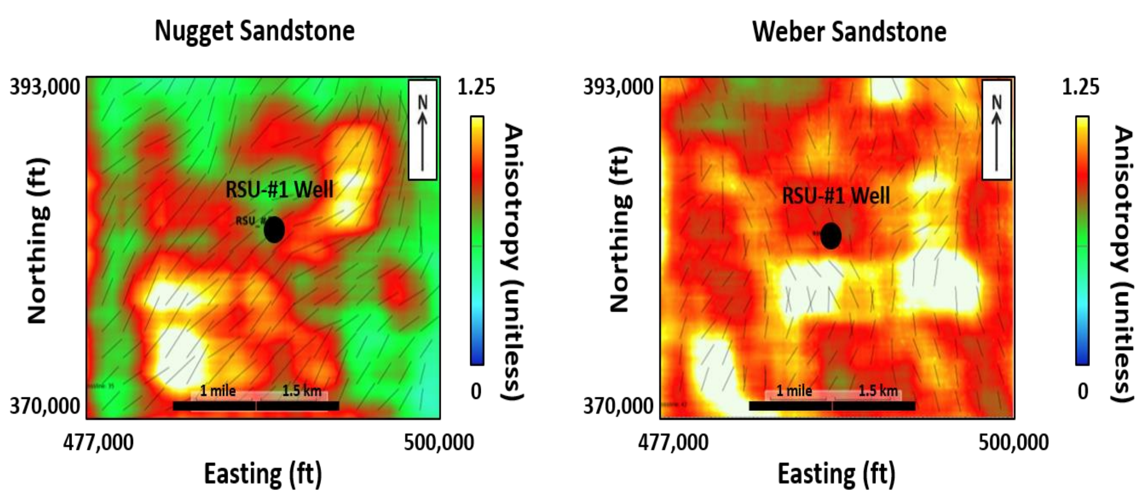

Figure 6.11: Anisotropic vector maps delineating fracture orientation for the Nugget and Weber sandstones.

A regional stress field (WSM, 2016) for the study area is displayed in Figure 6.12. The direction from various types of stress measurement validates the calculated anisotropy azimuthal values with a regional stress field trending in the northeast-southwest direction.

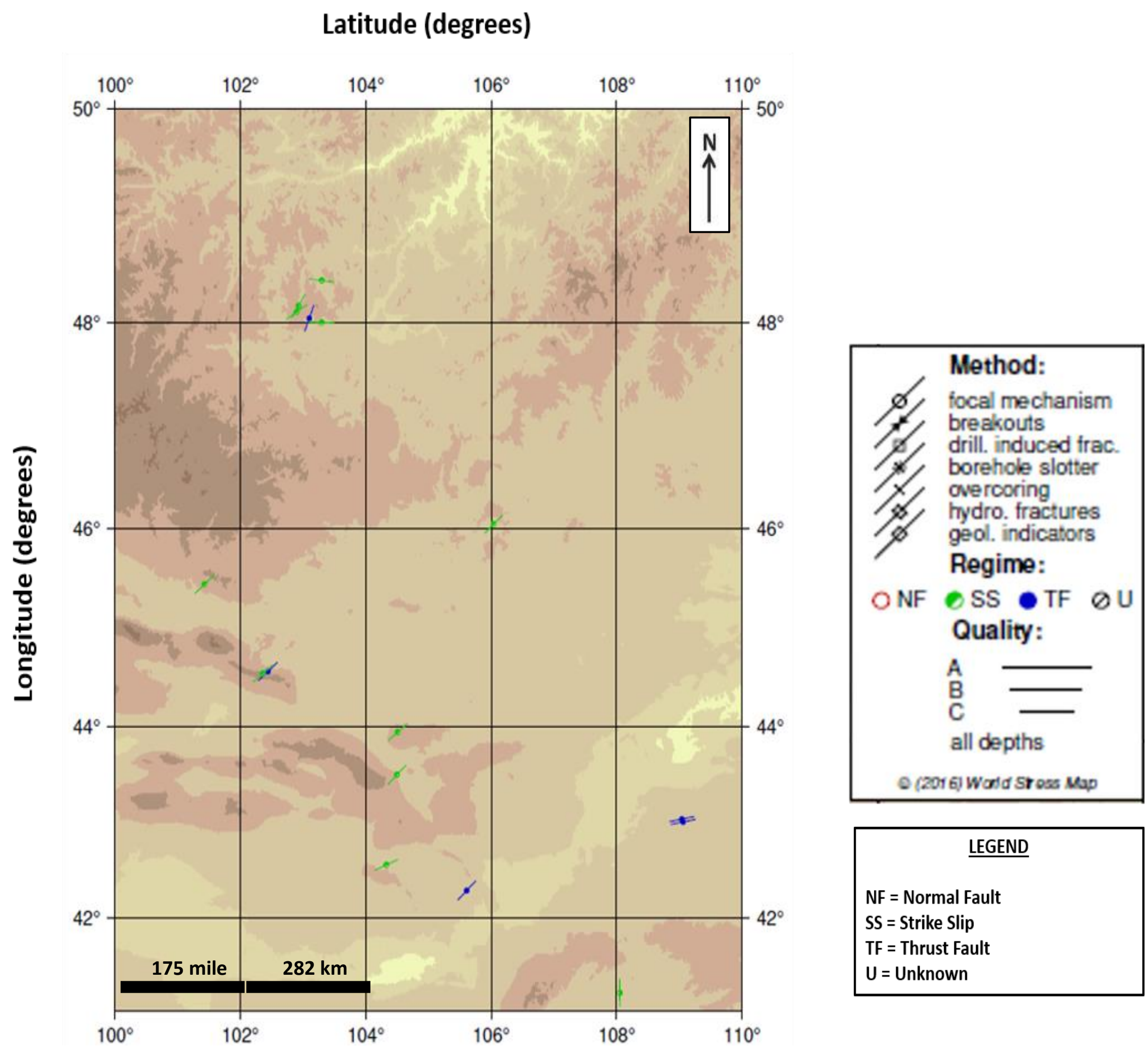

Figure 6.12: Regional stress map for the location for the area of study displaying direction of regional stress field from geologic measurements (modified from WSM, 2016).

6.4 Volumetric analysis for CO_2 sequestration

6.4.1 Time-to-depth conversion

The seismic data and attributes are converted from time-to-depth to reliably obtain thickness for the formations of interest, which are used for the volumetric calculation for CCS. A vertical velocity field is used in the time-to-depth conversion of the seismic data and attributes obtained from the AVO pre-stack inversion. Figure 6.13 shows an example of the time-to-depth conversion of the P impedance volume. The depth attribute volume suggests the Nugget and Weber sandstone formations of interest are at about 9,000 ft (2,743 m) and 10,000 ft (3,048 m) depth, respectively.

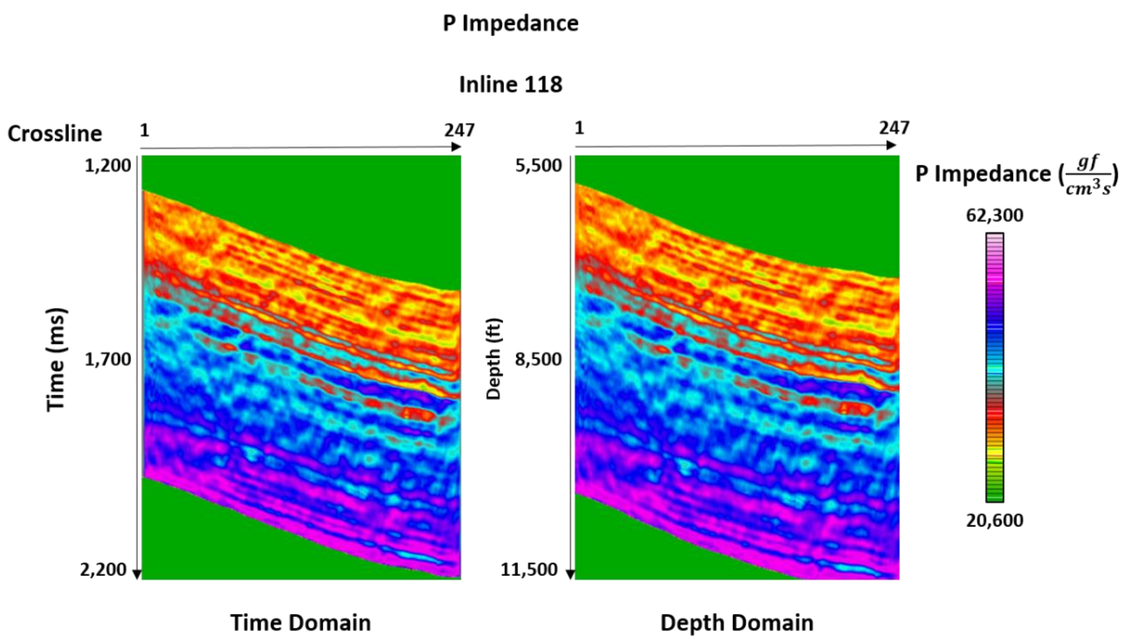

Figure 6.13: Time (left) to depth (right) conversion example from the P impedance volume.

6.4.2 Isopach maps

For the calculation of gross porosity volume for carbon dioxide storage, a thickness map for each formation of interest is generated (Figure 6.14). The isopach maps are created by utilizing the horizons picks of the top and base of the Nugget and Weber sandstones and subtracting them to obtain the thickness. From the stratigraphic column displayed in Figure 1.6, the thickness of the Nugget sandstone is approximately 350 ft (107 m) while the thickness of the Weber sandstone is 700 ft (213 m). These values correlate with the average values obtained from the isopach maps generated from the seismic horizons which are 385 ft (117 m) for the Nugget sandstone and 820 ft (250 m) for the Weber sandstone. Figure 6.15 displays the top and base depth map for the Nugget and Weber sandstones.

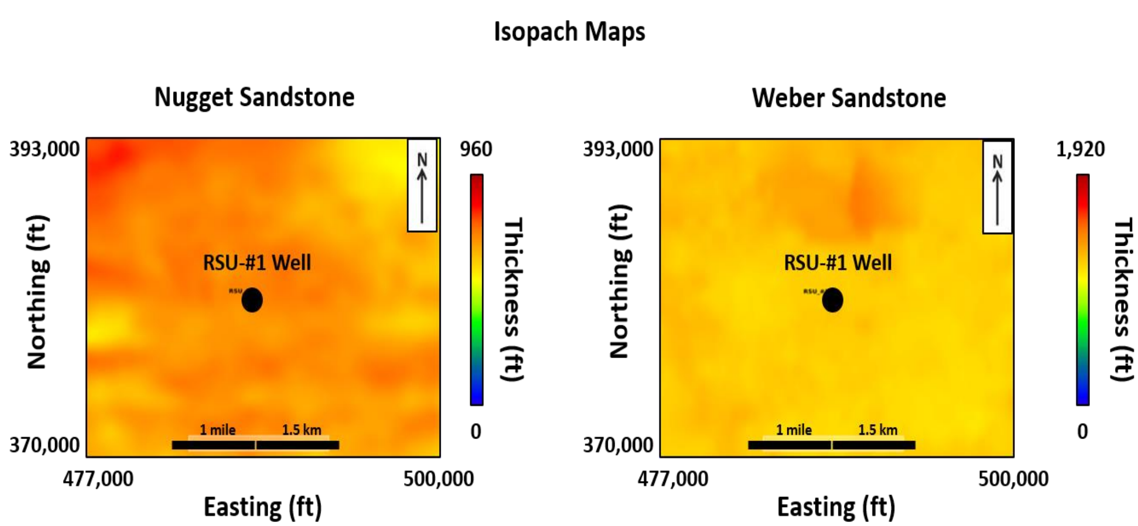

Figure 6.14: Thickness maps for the Nugget and Weber sandstones.

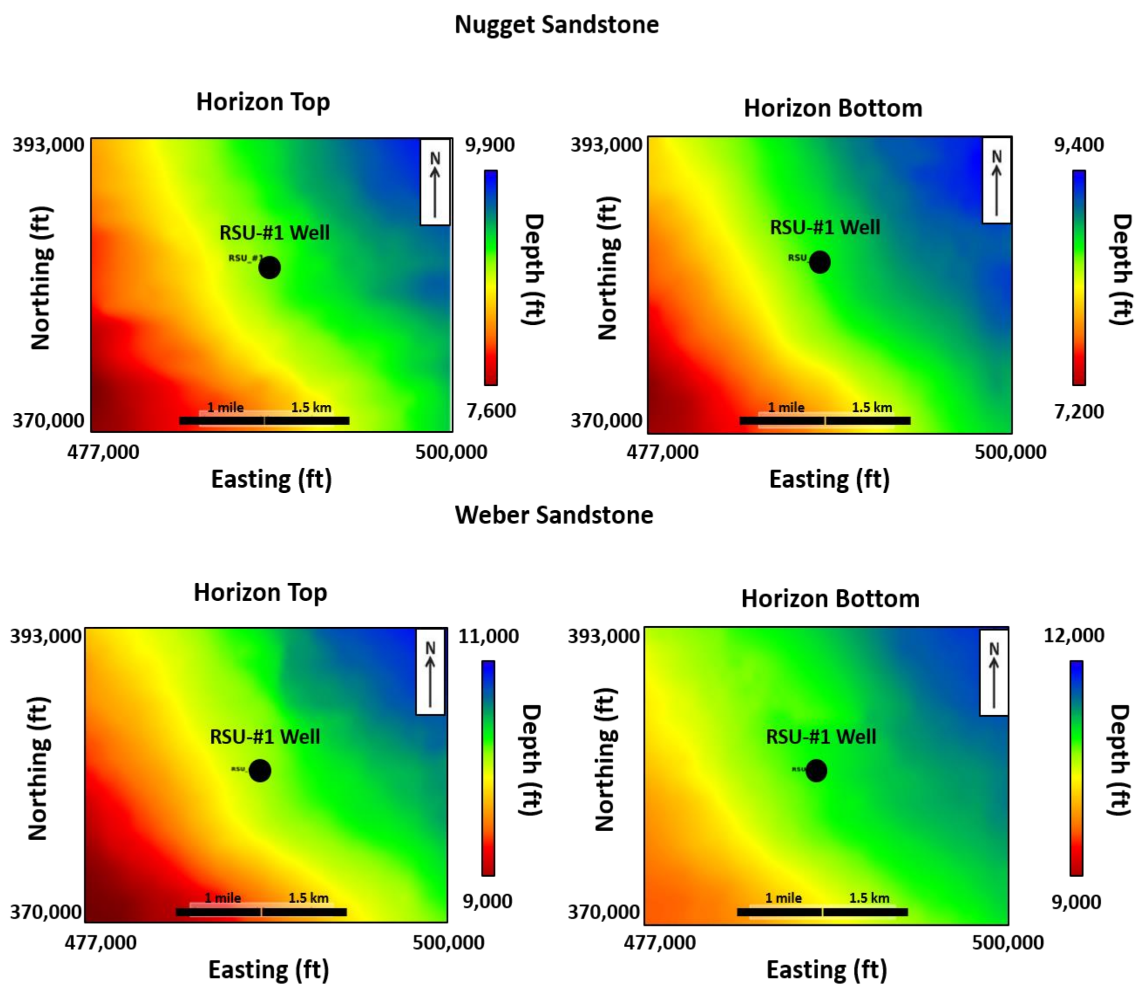

Figure 6.15: Top and base horizon depth maps for the Nugget and Weber sandstones.

6.4.5 Injection model and proposed well

Anomalies indicating higher porosity locations within the survey are analyzed from elastic and seismic attributes to determine the optimal area for carbon dioxide sequestration for both the Nugget and Weber sandstones. From elastic attributes derived from the AVO inversion, pre-stack attributes, and post-stack attributes, an area to the eastern section of the survey displays anomalies indicating higher porosity clean sandstone. In Figure 6.16, extracted RMS porosity maps are displayed for the Nugget and Weber sandstone with the location of a planned well. The proposed well to be drilled for carbon dioxide sequestration targets the center of the high-porosity anomaly to maximize the gross volumes available for storage. The location for the proposed well is at 486,984 Easting and 380,018 Northing. Figure 6.17 demonstrates a chair display from the seismic data at the location of the proposed well for carbon dioxide sequestration along with the Nugget and Weber horizons.

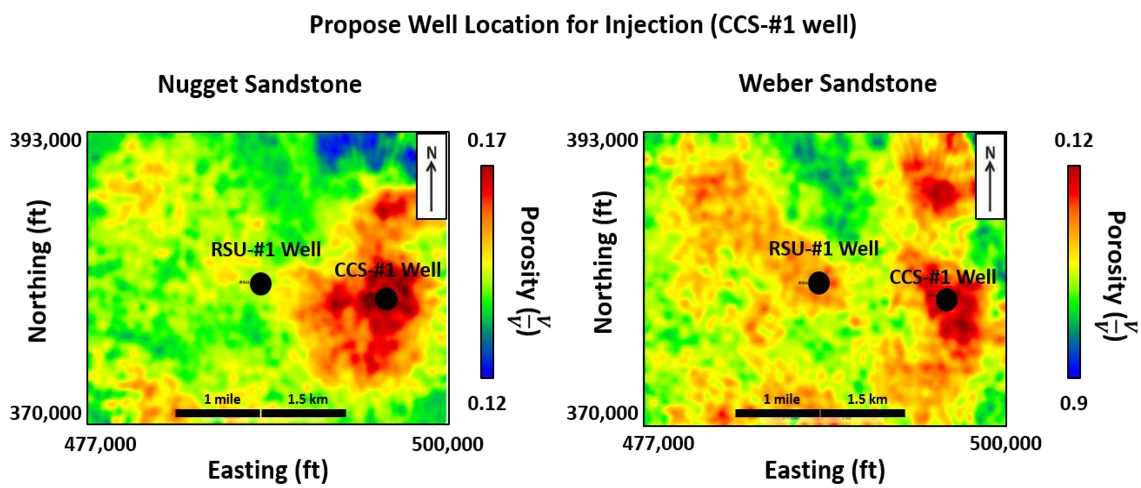

Figure 6.16: Extracted porosity map for the Nugget and Weber sandstones, displaying the location for the planned well (CCS-#1 well) for carbon dioxide sequestration.

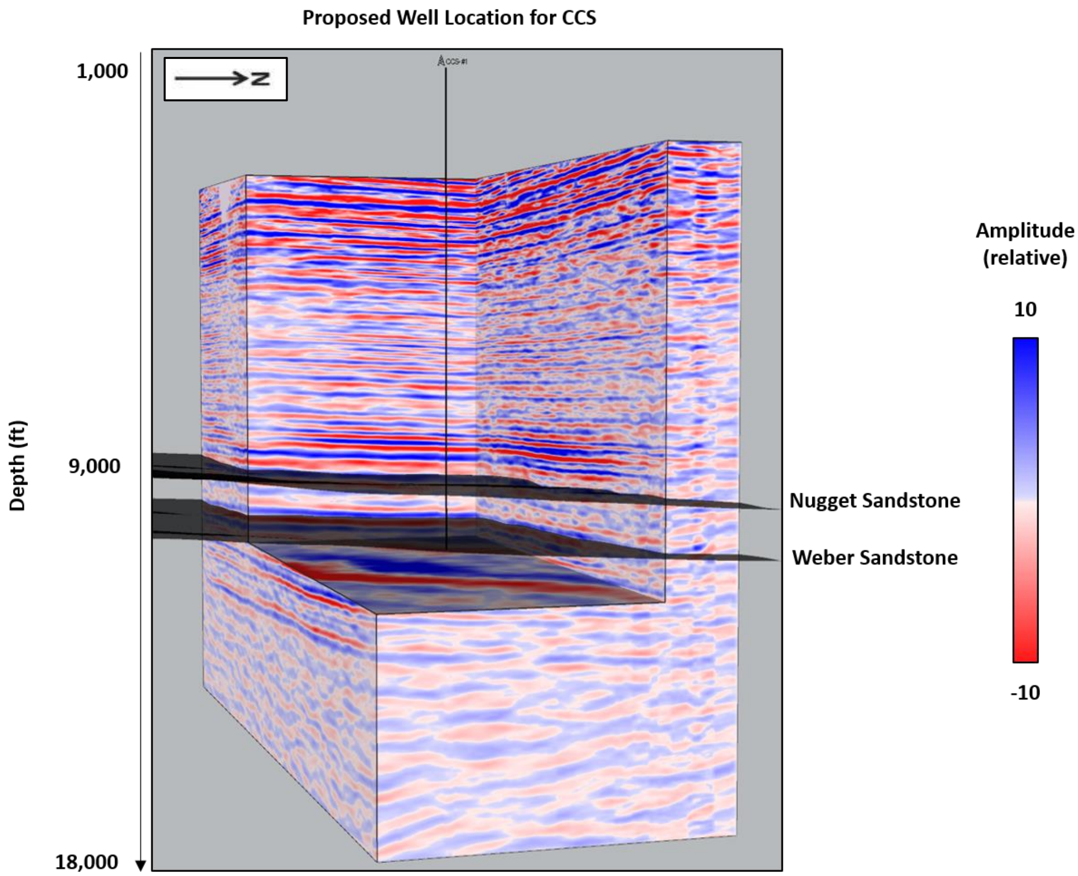

Figure 6.17: Chair display of seismic data at the location of the proposed well. The Nugget and Weber horizons are displayed.

6.4.3 Volumetric assessment

For the high-porosity anomaly determined from the RMS porosity maps extracted, areas can be analyzed for the estimation of low, middle, and high probabilities of targeting high-porosity in the Nugget and Weber sandstone. Such analysis is done by identifying areas surrounding the well location pertaining to a small area with highest-valued porosity anomaly and a large area with lower-valued porosity anomaly. This allows for the derivation of a probability analysis where a range of high to mid to low amount of volume available for carbon storage. The cases where the probability of finding high-porosity and low-porosity values within the sandstone are called P90 for 90% and P30 for 30% likeliness of a high-porosity sandstone. The case of 60% likeliness is in between and is called P60 case. Figure 6.18 displays porosity maps for Nugget and Weber sandstones with areas of 30%, 60%, and 90% likeliness of obtaining high-porosity values. Table 6.1 shows the values calculated estimated CO_2 mass for storage capacity in Mt for the Weber and Nugget sandstones. The P90, P60, and P30 for the Weber sandstone are 330.4 Mt, 176.7 Mt, and 61.9 Mt, respectively. On the other hand, for the estimates of mass for storage of the Nugget sandstone are 231.2 Mt, 94.4Mt, and 57.7 Mt for the P90, 60, and P30 cases.

Table 6.1: Estimated carbon dioxide mass for storage capacity in Mt

	Estimated Carbon Dioxide Mass for Storage Capacity (Mt)		
	High	Mid	Low
Weber Sandstone	330.4	176.7	61.9
Nugget Sandstone	231.2	94.4	57.7
Aggregated	561.6	271.1	119.6

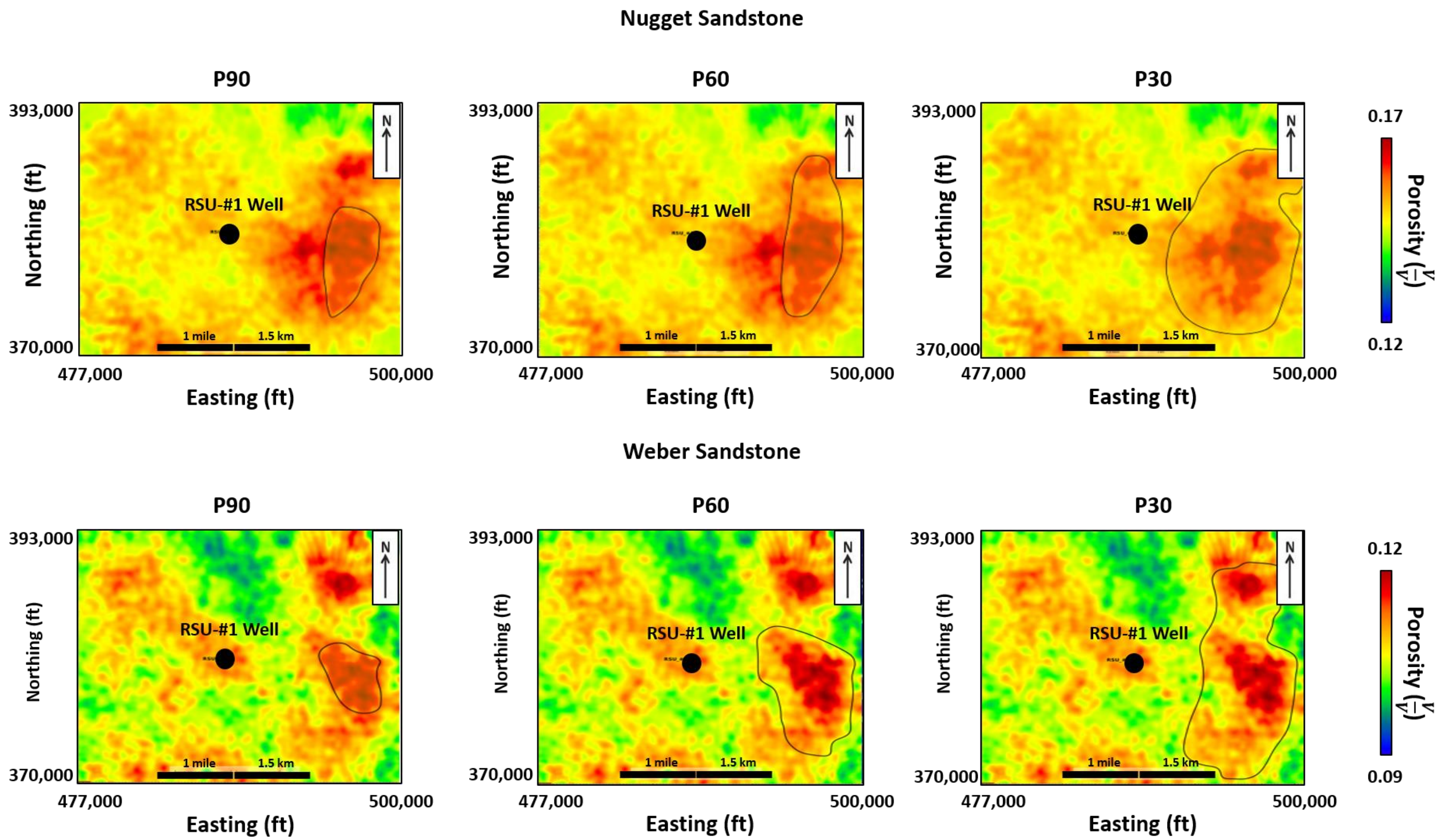

Figure 6.18: High porosity maps for the Nugget and Weber sandstones, demonstrating high, middle, and low probabilities of obtaining a high-porosity anomaly for CCS.

6.4.4 CO_2 chemical properties

Chemical properties of carbon dioxide are analyzed for the calculation of the phase state and molar volume at the high pressure and temperature for carbon dioxide sequestration. The equation of cubic state allows for the calculation of the molar volume of a non-ideal gas as a function of in-situ pressure and temperature (Valderrama, 2003). The equation considers the critical pressure and temperature values from the phase diagram, as well as a constant acentric factor unique to each chemical compound. Equation 13 displays the equations of cubic state used for the calculation of molar volume at a specific pressure and temperature conditions. The in-situ pressure and temperature for carbon dioxide sequestration are calculated by utilizing the geothermal gradient and lithostatic pressure gradient, displayed in Figure 6.19. At the target depth of approximately 10,000 feet, the pressure and temperature conditions are obtained from a rate of change of 25 ^{o}C/km and 23 kPa/m for temperature and pressure. The resulting in-situ pressure and temperature are 701 bars and 366.8 ^{o}K, respectively. The critical pressure and temperature from the carbon dioxide phase diagram (Figure 6.20) are used to calculate the molar volume for a supercritical fluid, which are 304.2 bars and 73.82 ^{o}K. Finally, the acentric factor in the equation of cubic state for carbon dioxide is a constant of 0.228.

$$P = \frac{RT}{V_m - b} - \frac{a\alpha}{{V_m}^2 + 2bV_m - b^2} \tag{13}$$

Where P is pressure, V_m is molar volume, T is absolute temperature, α is the acentric factor, R is the universal gas constant, and a and b are variables dependent of the critical pressure and temperature of the non-ideal gas. The molar volume obtained at the pressure and temperature conditions corresponding to 10,000 feet depth is 0.00004545 $\frac{mol}{m^3}$. Considering the molar mass for carbon dioxide of 44.01 $\frac{gm}{mol}$, the density obtained at the target depth is 0.968 $\frac{gm}{cm^3}$.

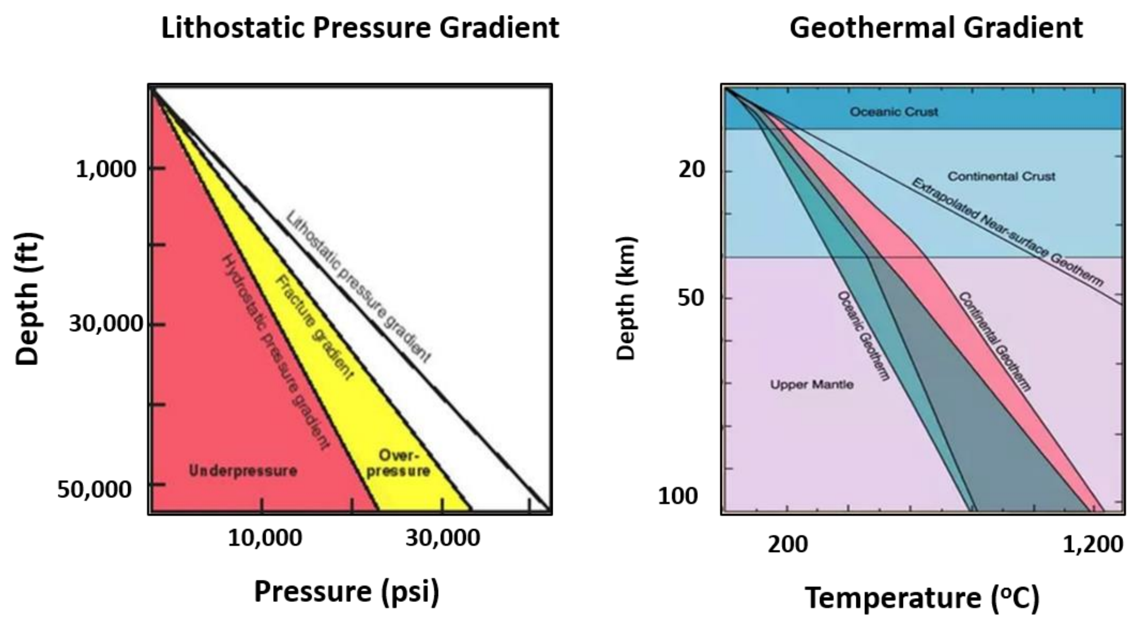

Figure 6.19: Geothermal (right) and lithostatic pressure (left) gradients for the subsurface (modified from Sclater and Christie, 1980; Schlumberger Oilfield Glossary, 2019).

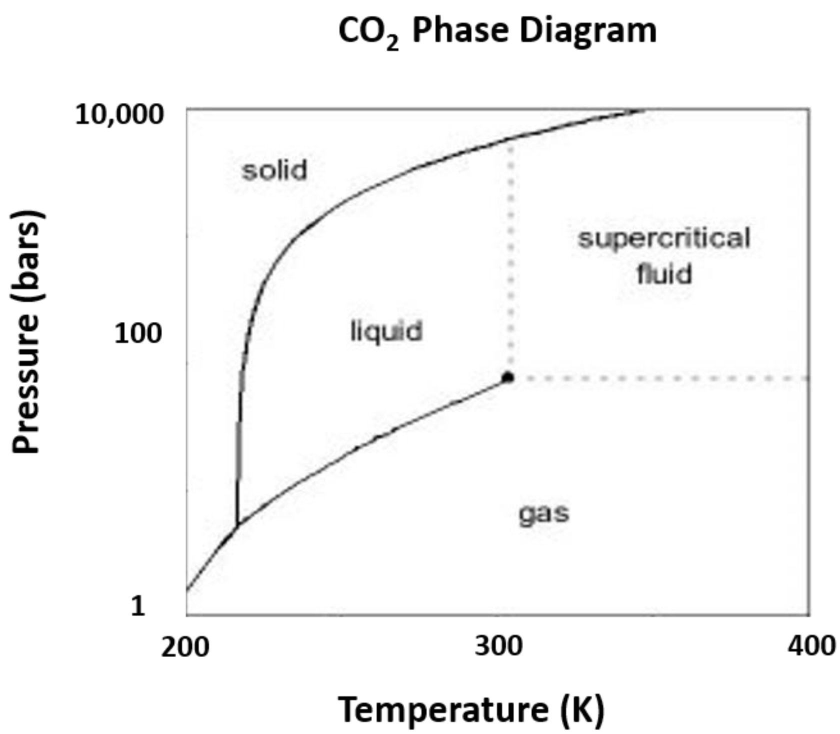

Figure 6.20: Phase diagram for carbon dioxide (modified from Global CCS Institute, 2019).

6.4.5 Injection analysis

What determines the ultimate storage potential of the space considered is the total affected space in combination with a maximum allowable average pressure increase in the affected space (Meer, 2008). The theoretical maximum storage capacity is now the cumulative effect of the combined effect of all compressibility effects of the rock and all fluids present in the affected space at the assumed maximum allowed average pressure to increase (Meer, 2008). For the definition and the subsequent explanation of the affected storage space and storage efficiency factor refer to Figure 6.21. The available space is the geologic formation pore space, which is entirely covered by a sealing caprock and limited by a spill point. The storage efficiency factor is calculated by dividing the used space by the available space and then multiplied by 100%. From past studies, the storage efficiency parameter is likely to have a value of 20% - 100% (Meer, 2008). For this study, a calculation of storage volume is done for scenarios with varying the storage efficiency parameter. The Jim Bridger power plant emits roughly an amount of 16.1 Mt yearly 0.45 Mt of carbon dioxide every day (Surdam and Jiao, 2007). The final storage volumetric calculation is done considering the aggregated gross porosity void volume available for the Nugget and

Weber sandstones, the amount of carbon dioxide volume capable for storage, the average emitted CO_2 at Jim Bridger power plant daily, and various efficiency storage values.

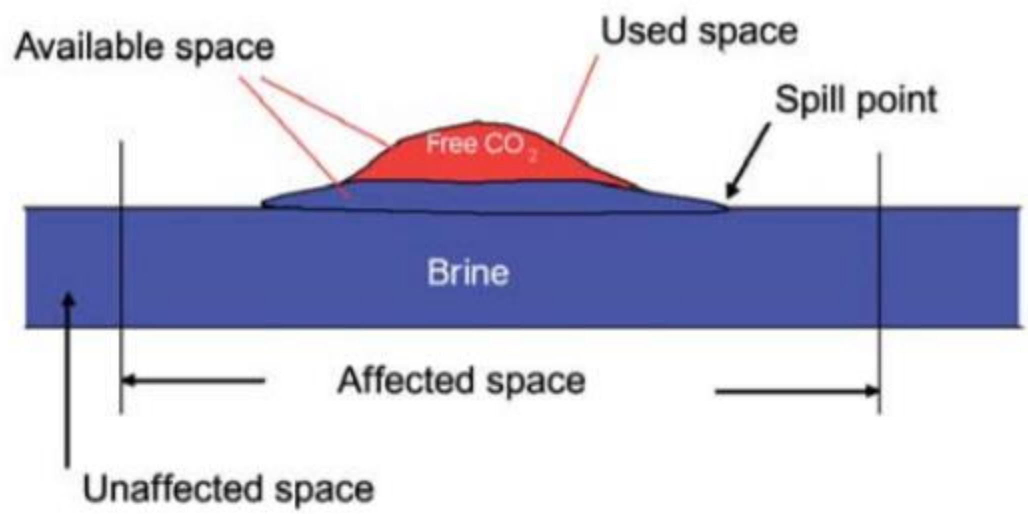

Figure 6.21: A schematic diagram of a CO_2 storage site demonstrating the principles of available space, used space, spill point, affected space, and unaffected space (from Meer, 2008).

USDOE (2007) proposed a method for calculating the total volume for carbon dioxide storage involving a storage efficiency factor displayed in Equation 14.

$$M_{CO2} = A\, h\, \emptyset\ \rho(P,T)\, E \quad (14)$$

Where M_{CO2} is the estimated carbon dioxide mass for storage capacity at the specified pressure and temperature conditions, A is the area, h is the thickness, $\emptyset$ is the effective porosity, ρ is the density, P is pressure, T is temperature, and E is the storage efficiency factor which is a function of a capacity coefficient, permeability, and irreducible water saturation (Juanes and Szulczewski, 2010). Measured permeability in the Weber sandstone ranges from 0.001 mD to 13.8 mD, with an average of 1.4 mD and the highest permeability in the upper eolian unit (Grana et al., 2017). Using the permeability and irreducible water saturation values for Weber sandstone and Madison limestone, Surdam (2007) suggests the storage efficiency factor ranges from 0.1 to 0.8.

Table 6.1 shows the high and low estimates of mass for storage in Mt for Nugget and Weber sandstones. The aggregated mass for storage of CO_2 range from 119.6 Mt to 561.6 Mt. In this study, values of 0.2, 0.4, 0.6, 0.8, and 1.0 are used for the storage efficiency factor. Table 6.2 displays mass for storage values for various storage efficiency factors. The range of CO_2 mass for storage capacity varies from 23.9 Mt to 561.6 Mt. Considering the amount of carbon dioxide emitted yearly by the Jim Bridger power plant of 16.3 Mt, the final calculations for the duration of sequestration are shown in Table 6.3. The estimates suggest sequestration is plausible for a period of 2 years to 35 years for low-and-high-storage capacities, respectively. The average duration for sequestration is 13 years.

Table 6.2: Estimated carbon dioxide mass for storage capacity in Mt considering the storage capacity factor

Estimated Carbon Dioxide Mass for Storage Capacity Considering Efficiency Factor (Mt)					
	Storage Efficiency Factor				
	0.2	0.4	0.6	0.8	1
High Storage Mass	112.3	224.6	337.0	449.3	561.6
Low Storage Mass	23.9	47.9	71.8	95.7	119.6
Avg. Storage Mass	68.1	136.2	204.4	272.5	340.6

Table 6.3: Estimated duration for carbon dioxide sequestration in years from the Jim Bridger power plant

Total duration for CCS (years)		
High estimate	Average estimate	Low estimate
35	13	2

Chapter 7

Conclusions and future work

The goal of this thesis is to understand the relationship between rock properties and their elastic response, petrophysical and rock physics analysis, seismic modeling, 3D-3C processing, seismic inversion, and multi-attribute analysis are integrated to delimit prospective areas with high-porosity content for carbon dioxide sequestration assessment. What I have found is summarized below.

7.1 Conclusions

- Vertical geophone component is processed and split into 60 different OVTs for application of Kirchhoff migration with 30,000 ft (9,144 m) aperture. By processing the data in the OVT domain, the offsets and azimuths are preserved for further analysis of anisotropy.
- Azimuthal anisotropy analysis is done by picking reflection events that show velocity variations with azimuth when sorted as common offset – common azimuth. Such events utilize the sinusoidal variation to solve the equation of an ellipse and values of anisotropy can be estimated. The azimuthal anisotropic

analysis displays anisotropic magnitude between 0.6 – 1.2 and anisotropic azimuth predominantly trends in the direction northeast-southwest (45 and 275 degrees) for the Weber and Nugget sandstones. Results show areas of higher anisotropy which could be a proxy for fractures within the sandstones that may be of interest for carbon dioxide sequestration. The anisotropic azimuth is indicative of the regional stress field and is validated by stress field data observed from geology in the area. The localized stress field can be a proxy for fracture orientation.

- Structure-Oriented Filtering (SOF) is applied to OVT volumes to remove random noise and improve reflection continuity and signal-to-noise values. SOF computes structural coherence from the seismic trace within +6 ms to -6 ms and using a 5 by 5 grid of traces to apply a median filter which removes the incoherent noise present. The algorithm is applied to offset vector tiles to avoid the mixing and smoothing the azimuthal response used for the azimuthal analysis.
- VTI velocity analysis utilizing the method developed by Swan (2001) is done on the CDP gathers post-migration to obtain velocity updates that flatten the gathers from NI and G values. Three passes of 10% velocity variations are applied, and the velocities within the Nugget and Weber sandstone formations are changed between 50 – 200 m/s for improved flattened reflection events. The resulting interval velocity field follows the geologic structure with higher continuity.
- Radon de-multiple is applied on the CDP gathers post-migration for the removal of long-period multiples. A time-variant polygon cut is applied on the tau-p

domain calculated from the pre-stack data with an 80 ms taper. The resulting gathers and stack show improved primary reflection event continuity, more reliable AVO response, and decreased noise content for a better geologic and amplitude anomaly interpretation.

- CDP domain noise attenuation is done by applying a mute on the frequency-wavenumber domain to remove linear noise from the data. The algorithm applies a mute in the *f-k* domain corresponding to velocity lower to 7,000 ft/s (2,134 m/s) within the frequencies of 5 Hz – 35 Hz. An additional noise attenuation method in CDP domain applied consists of transforming the data to the tau-p domain by a Radon transform and applying a time-variant mute to keep only the primary reflections. The data is transformed back to the space-time domain, and the resulting traces are scaled down to 66.333% while the input is scaled down to 33.333% and both are added together. The resulting CDP gathers have coherent and incoherent noise energy removed and improved signal-to-noise values.
- Angle ranges are analyzed on CDP gathers to determine the near, middle, and far angle ranges with similar reflection coherency and signal-to-noise values for the generation of angle stacks. The angle range analysis determined that angle stacks 00 – 13 degrees, 8 – 22 degrees, 18 – 32 degrees, and 28 – 42 degrees are optimal to input into the AVO inversion algorithm. The signal-to-noise ratio and coherency for the Nugget and Weber sandstone formations are similar throughout the angle

stacks with enough information in the far angles for the determination of the density term.

- Seismic-to-well correlation utilizing the conditioned stack for the vertical component data demonstrate the frequency and phase spectrum to be 5 Hz – 40 Hz and -50 degrees, respectively. Minor stretches and squeezes are made to match the synthetics from the well to the seismic traces at the well location. The cross-correlation is found to be at 80% within the target window from 1,400 ms to 2,000 ms. The Nugget and Weber sandstone's seismic response is characterized and matched by the synthetics from the well-logs.
- The seismic data is rotated to standard American SEGY polarity by applying a phase rotation of 50 degrees to the CDP gathers prior to the calculation of the angle stack. With zero phased angle stacks, wavelets are extracted for each one of the angle stacks with its respective scalars for the AVO inversion. The wavelets demonstrate to be consistently zero phased with +10 to -10 degree of error. The scalars for the wavelets to match the seismic amplitude are 5.1e-05, 4.3e-05, 2.9e-05, and 2.2e-05 for the near, middle, and far angle stacks, respectively.
- Low-frequency background models are generated by extrapolating well-log values for P impedance, S impedance, and density throughout the whole survey area guided by the Frontier shale, Weber sandstone, Nugget sandstone, and Madison limestone seismic horizons. The extrapolation is done by a cokriging algorithm that utilizes the well-logs values and the interval seismic velocities for

the guidance of the values for the survey area. The calculated models are then smoothed to the missing frequencies from the seismic data by applying a high-cut filter of 0 – 0 – 6 -12 Hz.

- Pre-stack simultaneous AVO inversion is a Bayesian algorithm used to generate volumes of P impedance, S impedance, and density derived from the seismic data. The inversion shows values for the Nugget and Weber sandstones to range for P impedance, S impedance, and density from 38,000 $\frac{gf}{cm^3 s}$ – 43,000 $\frac{gf}{cm^3 s}$, 27,000 $\frac{gf}{cm^3 s}$ – 32,000 $\frac{gf}{cm^3 s}$, and 2.4 $\frac{g}{cm^3}$ – 2.55 $\frac{g}{cm^3}$, respectively. 10 distinct elastic attributes are calculated from the inversion results such as σ, bulk modulus, shear modulus, lame constant, and $\frac{V_p}{V_s}$.
- A rock physics relationship is derived by cross-plotting normalized μρ and porosity using well-logs from the well RSU-#1. This relationship describes the variations in porosity in terms of shear modulus times density and has a 93% correlation which means we can use it reliably to obtain a porosity volume by applying the relationship to the elastic attributes from the inversion. A porosity volume is generated, and values of porosity for the Weber and Nugget sandstones range from 10% to 21%. The locations of high-porosity anomalies are analyzed and considered for the carbon dioxide sequestration.
- Elastic and seismic attribute analysis is used to validate the high-porosity anomalies within the survey area. Attributes such as λρ, μρ, σ, spectral decomposition, and sweetness are utilized to extract RMS amplitude maps to

obtain anomalous areas which may be correspondent to high-porosity values for the Nugget and Weber sandstones. Predominantly, anomalies found in the attribute volumes validate the locations of interest for carbon dioxide sequestration.

- The location of the high-porosity anomaly is within the eastern section of the survey, and a well is planned that goes through both anomalies for the Nugget and Weber sandstones to maximize storage capacity volume by injecting through both geologic formations. The proposed well is located at 486,984 (ft) Easting and 380,018 (ft) Northing. A probability analysis in which the anomaly is characterized by 30%, 60%, and 90% chance of obtaining high-porosity values is done, and volumetric are calculated for each.
- The inversion volumes are converted from time-to-depth using a vertical velocity function calculated from the VTI/HTI updated velocities. This is done to generate isopach maps to better understand the thickness variation for each of the Nugget and Weber sandstones for the carbon dioxide volumetric analysis. The isopach maps indicate the thickness of the Nugget and Weber sandstones to be approximately 330 - 360 ft (101 – 110 m) and 712 - 764 ft (217 – 233 m) of thickness, respectively.
- Carbon dioxide volumetric analysis is done by using the porosity values from the RMS extracted map, the areal extent of the anomaly for the 30%, 60%, and 90% case, and the thickness maps for the Nugget and Weber sandstones to generate a

total mass for storage capacity for carbon dioxide sequestration. For the high and low cases, the estimated mass for storage capacity is between 561.6 Mt and 119.6 Mt, respectively.

- A storage efficiency factor is analyzed to account for used storage, pressure increase after injection within the reservoir, carbon dioxide dissolution, permeability, saturating fluid displacement, and other factors that may decrease the storage capacity. Storage efficiency factor typically ranges from 20% to 100% (van der Meer, 2008), and these values are used to calculate maximum storage mass capacity. These values, in metric megatons, range from 23.9 Mt to 561.6 Mt.
- To calculate the volume of carbon dioxide that may be injected in the calculated maximum volume of storage, the equation of cubic state is used to determine chemical properties of carbon dioxide at reservoir depth pressure and temperatures. The calculated pressure and temperature at 10,000 ft (3,048 m) depth are of 701 bars and 365.59 kelvins. The equation indicates that the molar volume and density of carbon dioxide at the specified pressure and temperatures are 0.00004545 $\frac{m^3}{mol}$ and 0.968 $\frac{gm}{cm^3}$, respectively.
- Assuming the daily emissions of the Jim Bridger power plant of carbon dioxide is consistently 16.8 Mt, the total duration calculated for carbon dioxide sequestration is years ranges between 34 years and 2 years.
- For multicomponent processing, shear-wave velocities are estimated by generating a rock physics relationship at the RSU-#1 well for S-wave velocity in

terms of P-wave velocity that is then applied to the VTI/HTI updated RMS velocities from PP processing. These initial shear-wave velocities are used in a migration-velocity analysis where migration is done for various percentages of the initial shear-wave velocity volume. The percentages range from 50% to 300% then each migration output is utilized to generate velocity coherencies and mini-stacks which are used for the picking of more accurate shear-wave velocities. The final shear-wave velocities indicate a $\frac{V_p}{V_s}$ of approximately 2.8 – 3.4 in the near-surface and 1.8 to 1.6 within the Nugget and Weber sandstone formations.

- Shear-wave statics are obtained by picking the shear-wave refraction to determine near-surface velocities and delay time corrections needed to align the reflection events. The statics solution from the shear-refraction picking demonstrates values for the in the range of -80 ms to 80 ms for the receiver term, which are the only ones applied to the converted-wave seismic data. The shot refraction statics from the PP processing are also applied.
- ACP binning, component rotation to radial and transverse direction, shear-wave splitting analysis and rotation, and noise attenuation are applied in the processing flow of the converted-wave seismic data. A Kirchhoff migration of 30,000 ft (9,144 m) aperture utilizing PS ray-tracing is used for the migration algorithm to image converted-waves in the subsurface. Finally, event registration in the PP and PS stack is done to match the reflection events in PS time to PP time. The final stack

of the converted-wave displays coherent and continuous events of PS reflections in PP time.

- Utilizing the final converted-wave stack in PP time, a post-stack inversion is done using a seismic-to-well correlation from the well, an extracted wavelet, wavelet scalar for the PS stack, and S impedance background model. The resulting S impedance volume is of higher frequency than the PP inversion results and more reliable shear impedance values that are used for further assessment of carbon dioxide sequestration.

7.2 Future work

- Further processing of the converted-waves in terms of velocities, statics, and migration to improve the converted imaging.
- Generate a joint pre-stack PP – PS inversion utilizing the seismic data from the PP and PS events to obtain more accurate results of P impedance, S impedance, density, and elastic attributes that are used for the assessment of carbon dioxide.
- Propose a rock physics model to understand the individual effects of variations in mineralogy and porosity in the rock's elastic response that considers anisotropy.
- Study attenuation effects values from the sonic logs.
- Extend the bandwidth of the PP seismic data to match the frequency content of the PS seismic data to aid in the interpretation and inversion workflows. Increasing the PP data for 1 to 2 octaves is optimal for higher resolution of geologic events.
- Build a carbon dioxide injection model that is more robust. These models should consider complex parameters such as chemical phase change, temperature changes, pressure changes, irreducible water saturation, permeability, fluid displacement, storage capacity, and efficiency factor.

References

Aki, K., and Richards, P., 1980, Quantitative Seismology. Theory and Methods: Freeman, San Francisco.

Aki, K., and Richards, P., 2002, Quantitative seismology: University Science Books, Sausalito, California, USA, 2nd edition.

Allis, R.G., 2003, CO2 sequestration potential beneath large power plants in the Colorado Plateau-Southern Rocky Mountain region, USA: Proceedings, 2nd Annual Conference on Carbon Sequestration, Alexandria, VA, 1-13.

Benson, S.M., and Cole, D.R., 2008, CO2 Sequestration in Deep Sedimentary Formations: Elements, 4, 325-331.

Burns, 2017, Carbon Capture Projects Map: webpage accessed: March 2019. <https://www.thirdway.org/graphic/carbon-capture-projects-map>.

Castagna, J. P., and Backus, M.M., 1993, Offset-dependent reflectivity–Theory and practice of AVO analysis: SEG.

Chambers, R.L., Yarus, J.M., and Hird, K.B., 2000, Petroleum Geostatistics for the Nongeostatistician—Part 1: The Leading Edge, 19, 474-479.

Crain, E.R., 2003, Seismic Petrophysics Basics: webpage accesses: February 2019. < https://spec2000.net/26-seispetr0.htm>.

Erslev, E.A., and Koenig, N.V., 2009, 3D kinematics of Laramide, basement-involved Rocky Mountain deformations, USA: Insights from minor faults and GIS-enhanced structure maps: Geological Society of America, 204, 125-150.

Feng, H., and Bancroft, J.C., 2006, AVO principles, processing and inversion: webpage accessed: March 2019. <www.crewes.org/ForOurSponsors/ResearchReports/2006/2006-34.pdf>.

Feng, H., and Bancroft, J.C., 2006, AVO principles, processing and inversion: CREWES, Research Report, 18, 1–19.

Gaiser, J., 1999, Applications for Vector Coordinate Systems of Converted Waves Obtained by Multicomponent 3-D Data: The Leading Edge, 18, 1290-1300.

Global CCS Institute, 2019, Water and CO2: webpage accessed: April 2019. < https://hub.globalccsinstitute.com/publications/corrosion-and-materials-selection-ccs-systems/63-water-and-co2>.

Gomez, C.T., Tatham, R.H., 2005, Sensitivity analysis of seismic reflectivity to partial gas saturation: SEG Technical Program Expanded Abstracts 2005, 218-221.

Goodway, W., Chen, T., and Downton, J., 1997, Improved AVO fluid detection and lithology discrimination using Lamé petrophysical parameters; "Lambda-Rho", "MuRho", & "Lambda/Mu fluid stack", from P and S inversions: 67th Annual International Meeting, SEG, Expanded Abstracts, 183-186.

Grana, D., Verma, S., Pafeng, J., Lang, X., Sharma, H., Wu, W., Mclaughlin, F., Campbell, E., Ng, K., Alvarado, Vladimir., Mallick, S., and Kaszuba, J., 2017, A rock physics and seismic reservoir characterization study of the Rock Springs Uplift, a carbon dioxide sequestration site in Southwestern Wyoming: International Journal of Greenhouse Gas Control, 63, 296-309.

Gray, D., 2003, P-S converted-wave AVO: 73rd Annual International Meeting, SEG, Expanded Abstracts, 165-168.

Grossman, J. P., Popov, G., and Steinhoff, C., 2013, Integration of multicomponent processing and interpretation of the Pouce Coupe time-lapse survey: Focus on shear-wave splitting analysis: SEG Technical Program Expanded Abstracts 2013, 5136-5139.

Hart, B. S., 2008, Channel detection in 3-D seismic data using sweetness: AAPG Bulletin, 92, 733-742.

International Energy Agency (IEA), 2013, Technology Roadmap: Carbon Capture and Storage: webpage accessed: March 2019.

<http://www.iea.org/publications/freepublications/publication/TechnologyRoadmapCarbonCaptureandStorage.pdf>.

Jensen, E.H., Johansen, T.A., Avseth, P., and Bredesen, K., 2016, Quantitative interpretation using inverse rock physics modeling on AVO data: The Leading Edge, 35, 677-683.

Journel, A.G., 1989, Fundamentals of Geostatistics in Five Lessons. Short Course in Geology: AGU, Washington, DC, 8, 40.

Juanes, R., MacMinn, C.W., and Szulczewski, M.L., 2010, The footprint of the CO2 plume during carbon dioxide storage in saline aquifers: storage efficiency for capillary trapping at the basin scale: Transport in Porous Media, 82, 19–30.

Mallick, S., and Adhikari, S., 2015, Amplitude-variation-with-offset and prestack-waveform inversion: A direct comparison using a real data example from the Rock Springs Uplift, Wyoming, USA: Geophysics, 80, P.B45-B59.

McLaughlin, J. F., and Garcia-Gonzales, M., 2013, Detailed geologic characterization of core and well data from the Weber and Madison Formations and associated seals at a potential CO2 sequestration site in southwest Wyoming: Defining lithologic, geochemical, diagenetic, and burial histories relative to successful CO2 storage: Springer, Environmental Science and Engineering, 55-96.

Meer, B.V., and Egberts, P., 2008, Calculating subsurface CO2 storage capacities: The Leading Edge, 27(4), 502-505.

Meer, L.G.H., 1993, The conditions limiting CO2 storage in aquifers: Energy Conversion Management 34, 959–966.

Omnes, G., 1978, Exploring with SH-waves: CSEG, 14, 40-49.

Padhi, A., and Mallick, S., 2013, Multicomponent Pre-Stack Seismic Waveform Inversion in Transversely Isotropic Media Using a Non-Dominated Sorting Genetic Algorithm: Geophysical Journal International, 193, 1600–1618.

Pafeng, J., Mallick, S., and Sharma, H., 2017, Prestack waveform inversion of three-dimensional seismic data — An example from the Rock Springs Uplift, Wyoming, USA: Geophysics, 82, P.B1-B12.

Parson, R., 1986, Estimating reservoir mechanical properties using constant offset images of reflection coefficients and incident angles: 56th Annual International Meeting, SEG, Expanded Abstracts, 617-620.

Rawlinson, N., Hauser, J., and Sambridge, M., 2007, Seismic ray tracing and wavefront tracking in laterally heterogeneous media: Advances in Geophysics, 49, 203-267.

Russell, B., 2012, Making sense of all that AVO stuff!: 22nd Geophysical Conference, ASEG, Extended Abstracts, 1-4.

Russell, B., Hampson, D., Chun, J., 1990, Noise elimination and the Radon transform, Part 1: The Leading Edge, 9, 18-23.

Saputra, 2008, Shale Volume Calculation: webpage accessed: March 2019. <https://www.cgg.com/data/1/rec_docs/883_Shale_Volume_Calculation.pdf>.

Schlumberger Oilfield Glossary, 2019, Gamma-ray log: webpage accessed: March 2019. <https://www.glossary.oilfield.slb.com/en/TeRMS/g/gamma_ray_log.aspx>.

Sclater, J.G., and Christie, P.A.F., 1980, Continental Stretching: An Explanation of the Post-Mid-Cretaceous Subsidence of the Central North Sea Basin: Journal of Geophysical Research, 85, 3711-3739.

Sheriff, R.E., 2002, Encyclopedic Dictionary of Exploration Geophysics (4th ed.): Society of Exploration Geophysicists, SEG Geophysical Reference Series No. 13.

Shifan, Z., Maoshan, C., Lei, L., Chunfeng, T., Zhonghong, W., and Xiaohui, Z., 2018, Offset vector tile domain wide-azimuth prestack seismic interpretation methods and applications: Interpretation, 6, T337-T347.

Shuey, R.T., 1985, A simplification of the Zoeppritz equations: Geophysics, 50, 609-614.

Simmons, J., and Backus, M., 2001, Shear waves from 3-D-9-C seismic reflection data: The Leading Edge, 20, 604-612.

Smith, G.C., and Gidlow, P. M., 1987, Weighted stacking from rock property estimation and detection of gas: Geophys. Prosp., 35, 993-1014.

Stewart, R.R., Gaiser, J.E., Brown, R.J., and Lawton, D.C., 2002, Converted-wave seismic exploration: Methods. Geophysics, 67, 1348-1363.

Surdam, R.C., and Jiao, Z., 2007, The Rock Springs uplift: an outstanding geological CO2 sequestration site in southwest Wyoming. Wyoming State Geological Survey: Challenges in Geologic Resource Development No. 2.

Swan, H.W., 2001, Velocities from amplitude variations with offset: Geophysics, 66, 1735-1743.

Tessmer, G., and Behle, A., 1988, Common reflection point data stacking technique for converted waves: Geophys. Prosp., 36, 671–688.

United States Environmental Protection Agency (EPA), 2017, Carbon Dioxide Capture and Sequestration: Overview: webpage accessed: February 2019. < https://archive.epa.gov/epa/climatechange/carbon-dioxide-capture-and-sequestration-overview.html>.

USDOE (U.S. Department of Energy), 2007, Methodology for development of carbon sequestration capacity estimates: Appendix a. Carbon Sequestration Atlas of United States and Canada. National Energy Technology Laboratory, Pittsburgh, PA, USA.

Valderrama, J.O., 2003, The State of the Cubic Equations of State: Industrial and Engineering Chemistry Research, 42, 1603-1618.

Veeken, P.C.H., and Da Silva, M., 2004, Seismic inversion methods and some of their constraints: First Break, 22, 15-38.

Verm, R.W., and Hilterman, F.J., 1994, Lithologic color-coded sections by AVO cross plots: 64^{th} Annual International Meeting, SEG, Expanded Abstracts, 1092-1095.

Vermeer, G.J., 1998, 3-D symmetric sampling: Geophysics, 63, 1629-1647.

White, R., and Simm, R., 2003, Tutorial: Good practice in well ties: First Break, 21, 75-83.

Wiggins, R., Kenny, G.S., and McClure, C.D., 1985, A method for determining and displaying the shear-velocity reflectivities of a geologic formation: The Journal of the Acoustical Society of America, 79, 589-590.

World Stress Map (WSM), 2016, WSM Database 2016: webpage accessed: January 2019. < http://www.world-stress-map.org/casmo/>.

Wyllie, M.R.J., Gregory, A.R., and Gardner, L.W., 1956, Elastic wave velocities in heterogeneous and porous media: Geophysics, 21, 41-70.

Xu Y., and Bancroft J.C., 1997, Joint AVO analysis of PP and PS seismic data: CREWES, Research Report, 9, 1-44.

Yilmaz, 2001, Seismic Data Analysis: Processing, Inversion, and Interpretation of Seismic Data: Society of Exploration Geophysicists.